

UNIVERSITY OF CALIFORNIA

Los Angeles

**Molecular Dynamics Simulations of the
Deformation of Nano-Structured Materials**

A dissertation submitted in partial satisfaction

of the requirements for the degree

Doctor of Philosophy in Materials Science and Engineering

by

Lan Li

2007

© Copyright by
Lan Li
2007

The dissertation of Lan Li is approved.

Jiun-Shyan Chen

Ya-hong Xie

Nasr M. Ghoniem, Committee Chair

University of California, Los Angeles

2007

This dissertation is dedicated to my parents, for their love and continuous support.

TABLE OF CONTENTS

1	Introduction and Thesis Objectives	1
1.1	Brief Overview of Nano Materials	1
1.1.1	What are Nanomaterials?	1
1.1.2	Applications of Nanomaterials	2
1.2	Nano-Laminates and Nano Twins	3
1.2.1	Nano-Laminates	3
1.2.2	Nano-Twinned Cu	6
1.2.3	Applications– the Strongest Metals Ever Known	11
1.2.4	Why are Nano-Layered Structures so Strong?	12
1.3	Computer Simulations on Materials	13
1.4	Thesis Objectives	15
2	Review of Theoretical Research on the Strength of Nano-structured Materials	16
2.1	Computational Methods for Studies of the Mechanical Behavior of Nano-structured Materials	16
2.1.1	Ab-initio Simulations	16
2.1.2	Atomistic Simulations	17
2.1.3	Computational Mesomechanics	18
2.2	Multi-scale Simulation and Atomistic/Continuum Coupling Method	19
2.3	Theoretical Mechanisms for the Strength of nano-structured Materials	21

2.3.1	Hall-Petch Approach	21
2.3.2	The Koehler Barrier	22
2.3.3	The Peierls-Nabarro Model	23
2.4	MD Simulations in Nano-mechanics	27
2.4.1	Molecular Dynamics Simulations of Nano-layered Structures	32
3	Molecular Dynamics Computational Methods	35
3.1	The Principles of the Molecular Dynamics Method	36
3.1.1	Advantages and Limitations	38
3.1.2	Algorithm of Molecular Dynamics	39
3.2	Interatomic Potentials	46
3.2.1	Connections Between Quantum and Approximate Potentials	49
3.2.2	Pair Potentials	50
3.2.3	Effective Medium Potentials	52
3.2.4	Quantum-based Potentials - The Tight-Binding Method .	59
3.3	Boundary Conditions	63
3.3.1	The Rigid Boundary Condition	64
3.3.2	Periodic Boundary Conditions	64
3.3.3	Flexible Boundary Conditions – Greens Function	64
3.4	Stress and Temperature Control	67
4	Results for Dislocation Transmission in Cu/Ni Nano-Layers .	69
4.1	Numerical Models	69
4.2	Dislocation Core Dissociation	71

4.3	Motion of Dislocations in Nano-layers	73
4.4	Discussions	75
5	Deformation of Nano-twinned Copper	78
5.1	Atom Identification Methodology	78
5.2	Deformation of Nano-twinned Copper Crystals	80
5.2.1	Numerical Model	80
5.2.2	Results	82
5.3	Twin Boundary Migration (TBM) Mechanism	91
5.3.1	Computational Model	91
5.3.2	Simulation Results for Twin Boundary Migration	91
5.3.3	Mechanism of Twin Boundary Migration (TBM)	99
5.4	Size Effects on the Deformation of Nano-Twinned Copper	102
5.4.1	Computational Model for nano-twinned Copper crystals	102
5.4.2	Mechanical Twinning	103
5.4.3	Results for Constant Shear Strain Rate Deformation	104
5.4.4	Results for Constant Stress	114
5.4.5	Summary of Nano-twin Lamella Size Effects	128
5.5	Nano-grain Cu with Nano-Twin Structure	129
6	Conclusions	132
6.1	Summary of Discussions	132
A	Molecular Dynamics Code Summary	136

A.1	XMD	136
A.2	LAMMPS	137
A.3	Other MD codes	137
A.4	MakeFiles	138
A.5	SIDE CODE	138
A.5.1	Code to build the input model	138
A.5.2	Code to analyze the output model	140
A.5.3	Software to Visualize Atoms	141
A.5.4	Adding Dislocations by the Anisotropic Displacement Field (Courtesy of Dr. Satish Rao, AFRL)	141
	References	143

LIST OF FIGURES

1.1	A multi-period ZrC/Si Nano-Laminate[85].	4
1.2	A nano-laminate of copper and niobium	5
1.3	Strength (estimated as hardness divided by 3) vs. the layer thickness of several Cu-based multi-layers, and compare to pure metals (estimated at 10 μm grain size). [Data is from Los Alamos National Laboratory].	6
1.4	Atomic packing of the (111) plane in an FCC crystal	7
1.5	A twin boundary in FCC crystal	7
1.6	TEM observations of the typical microstructure in an as-deposited Cu sample [48]. A bright-field TEM image (A) and the electron diffraction pattern (inset) show roughly equiaxed submicrometer-sized grains with random orientations separated by high-angle GBs. The statistical distributions for grain size (B) and for thickness of the twin/matrix lamellae (C) were obtained from the many TEM images of the same sample. Electron diffraction patterns [inset in (D)] indicate that the twins in each grain are parallel to each other in 111 planes (D), and high-resolution TEM images (E) show that the twins follow a sequence of ATATA..., with twinning elements, for example, A:($\bar{1}1\bar{1}$)/[$\bar{1}12$] and T:($\bar{1}11$)/[$1\bar{1}2$]	9

1.7	(A) A typical tensile stress-strain curve for the as-deposited Cu sample with nano-twins in comparison with that for a coarse-grained polycrystalline Cu sample (with an average grain size larger than $100 \mu m$) and a nanocrystalline (nc) Cu sample (mean grain size 30 nm) (11). The inset shows the geometry of the tensile sample for the as-deposited nano-twin sample (R, radius of curvature). (B) The measured temperature dependence of electrical resistivity (ρ) for the as-deposited nano-twin Cu sample and the coarse-grained sample in a temperature range from 2 to 296 K. For comparison, electrical resistivity measurement results in a nanocrystalline Cu sample with a mean grain size of 15 nm are also included. Data taken from reference [48]	10
2.1	Hall-Petch approach	22
2.2	Schematic illustration of the Koehler effect.	24
2.3	Two semi-infinite simple cubic crystals with disregistry in the x direction form an edge dislocation.[32]	25
2.4	Infinitesimal dislocations replace the original single dislocation in the Peierls-Nabarro model. [32]	26
2.5	Analytical solution for Peierls-Nabarro model	28
2.6	Three snapshots of a pair of edge dislocations in a dipole configuration, showing the stabilization of a dipole despite the dynamic overshoot [?]	30
2.7	MD simulations of nano-scale grain boundary evolution under externally applied stress . Time is labelled in each frame. "H" indicates high-angle, and "L" low-angle grain boundary [76].	31
3.1	Molecular statics method: quench	38

3.2	A flow chart of a typical MD algorithm.	39
3.3	creating atomic configuration	40
3.4	Initial velocities	41
3.5	Periodic Boundary Conditions	42
3.6	Cutoff distance in force calculation	43
3.7	Illustration of the leapfrog algorithm	44
3.8	Green function boundary condition	67
4.1	Schematic of the simulation model for Cu/Ni nano-layer structure. . .	70
4.2	Dissociation of a perfect dislocation into two Shockley partials	71
4.3	Dissociation of the dislocation core into two partials in Copper	72
4.4	The core width of dissociated dislocations in different layer structures as a function of the wavelength for Ni. (a) Solid line: in 5 layers of Ni/Cu/Ni/Cu/Ni, (b) dot line: in 3 layers of Cu/Ni/Cu, (c) dash line: in single Ni crystal.	73
4.5	The core width of dissociated dislocations in different layer structures as a function of the wavelength for Cu. (a) Solid line: in 5 layers of Cu/Ni/Cu/Ni/Cu, (b) dot line: in 3 layers of Ni/Cu/Ni, (c) dash line: in single Cu crystal.	74
4.6	Core motion under shear stress in 5 layers Ni-Cu-Ni-Cu-Ni structure with wavelength of 10 nm. The upper curves are for the position of the leading dislocation, and the bottom curves are for the trailing partials. (a) Solid line: under 200 MPa, (b) dash line: under 400 MPa, (c) dot line: under 800 Mpa, (d) dash dot dot line: under 1200 MPa.	75

4.7	Core motion under shear stress in 3 layers Ni-Cu-Ni structure with wavelength of 10 nm. (a) under shear stress of 800 MPa. (b) under shear stress of 1200 MPa.	76
5.1	Illustration of the Centro-symmetry method	79
5.2	Atoms identified at a twin interface in an Fcc crystal.	80
5.3	Schematic illustration for the computational box used in MD simulations of the Cu twin structure.	81
5.4	A schematic of the computation method for calculations of atomic level stress and strain.	82
5.5	Time-sequence of atoms in defect positions in a copper single crystal subjected to a high tensile strain rate of $5 \times 10^8/s$	83
5.6	Time-sequence of atoms in defect positions in a 3-layer twinned copper crystal subjected to a high tensile strain rate of $5 \times 10^8/s$	84
5.7	Time-sequence of atoms in defect positions in a single crystal subjected to a high shear strain rate of $5 \times 10^8/s$	85
5.8	Time-sequence of atoms in defect positions in a 3-layer twinned copper crystal subjected to a high shear strain rate of $5 \times 10^8/s$	86
5.9	The density of twinned planes as a function of time under strain rate of $5 \times 10^8/s$. (a) Dotted line: a copper single crystal subjected to a high tensile strain, (b) dashed dot dot line: a 3-layer twinned copper crystal subjected to a high tensile strain, (c) solid line: a single crystal subjected to a high shear strain, (d) dash dot line: a 3-layer twinned copper crystal subjected to a high shear strain.	87

5.10	Stress-strain curves for deformed copper crystals. (a) Solid line: tension of a single crystal, (b) dash line: tension of a twinned crystal, (c) dot line: shear of a single crystal, and (d) dash dot dot line: shear of a twinned crystal.	88
5.11	Detailed time-sequence of atoms in defect positions in a 3-layer twinned copper crystal subjected to a high shear strain rate of $5 \times 10^8/s$	90
5.12	Schematic of the computational model for twin boundary migration simulations	92
5.13	3D view of the simulation box for twin boundary migration	92
5.14	The 3D visualization of dislocation nucleation and motion on the twin boundary: The white atoms represent defect atoms which align together to form dislocations. The red atomic plane is the original twin interface. The green atomic plane is the new twin interface which is one-atomic layer higher than the red plane.	94
5.15	Burgers Circuit identifying a Schockley partial dislocation.	96
5.16	Plane view of the relative displacement of two parts of the crystal near the partial dislocation.	96
5.17	The relative position between 2 layers of atoms at the dislocation line.	97
5.18	A sketch of the relative positions between 2 layers of atoms at the dislocation line.	97
5.19	Plane view of the relative displacement of the two parts of the crystal near the curved partial dislocations.	98
5.20	Burgers Circuit for the curved partial dislocations	98
5.21	A complete Burgers circuit around atoms in high deformation regions illustrate the lack of a dislocation there.	99

5.22	A plane view around atoms in high deformation regions illustrate the lack of a dislocation there, because there is no relative displacement for the atoms on different sides of the yellow line.	100
5.23	Sketch of the twin boundary migration mechanism leading by a Shockley partial dislocation in an FCC crystal.	101
5.24	Time-sequence showing the progression of deformation in a nano-twinned copper crystal under an applied tensile strain, with fast quench relaxation. The sequence is as follows: (a) At 3 ps, strain = 3%. (b) At 3.5 ps, strain = 3.5%. (c) At 4 ps, strain = 4.0%.(d) At 4.5 ps, strain = 4.5%.(e) At 5 ps, strain = 5.0%.(f) At 5.5 ps, strain = 5.5%.(g) At 6 ps, strain = 6.0%.(h) At 6.5 ps, strain = 6.5%.(i) At 7 ps, strain = 7.0%.(j) At 7.5 ps, strain = 7.5%.(k) At 8 ps, strain = 8.0%.(l) At 8.5 ps, strain = 8.5%.(m) At 9 ps, strain = 9.0%.(n) At 9.5 ps, strain = 9.5%.(o) At 10 ps, strain = 10.0%. Green atoms are for the stacking fault layers, red represent other defects such as atoms, vacancies, noises, dislocations etc.	105
5.25	A detailed view of mechanical twinning under an applied tensile strain, at 10 ps and with 10% strain. Blue atoms represent original matrix atoms and green ones show the stacking fault layers.	106
5.26	Growth of the relative stacking fault areal density for rapid quench of $10^{10}s^{-1}$, solid line, and for slower quench rate of 10^9s^{-1} , dotted line. .	106

- 5.27 A time-sequence of the deformation of a nano-twinned copper structure with a wavelength of 3 nm with applied shear strain at a constant quench rate of $10^9 s^{-1}$. The sequence is as follows: (a) At 54 ps, strain = 5.4%. (b) At 57 ps, strain = 5.7%. (c) At 60 ps, strain = 6.0%. (d) At 63 ps, strain = 6.3%. (e) At 66 ps, strain = 6.6%. (f) At 69 ps, strain = 6.9%. (g) At 72 ps, strain = 7.2%. (h) At 75 ps, strain = 7.5%. (i) At 78 ps, strain = 7.8%. (j) At 81 ps, strain = 8.1%. (k) At 84 ps, strain = 8.4%. (l) At 87 ps, strain = 8.7%. (m) At 90 ps, strain = 9.0%. (n) At 93 ps, strain = 9.3%. (o) At 96 ps, strain = 9.6%. 108
- 5.28 A time-sequence of the deformation of a single copper crystal with applied shear strain at a constant quench rate of $10^9 s^{-1}$. The sequence is as follows: (a) At 58 ps, strain = 5.8%. (b) At 61 ps, strain = 6.1%. (c) At 64 ps, strain = 6.4%. (d) At 67 ps, strain = 6.7%. (e) At 70 ps, strain = 7.0%. (f) At 73 ps, strain = 7.3%. (g) At 76 ps, strain = 7.6%. (h) At 79 ps, strain = 7.9%. (i) At 82 ps, strain = 8.2%. (j) At 85 ps, strain = 8.5%. (k) At 88 ps, strain = 8.8%. (l) At 91 ps, strain = 9.1%. (m) At 94 ps, strain = 9.4%. (n) At 97 ps, strain = 9.7%. (o) At 100 ps, strain = 10%. 109
- 5.29 Dominant deformation modes of nano-twinned copper crystals. The figure shows the operation of the Twin Boundary Migration (TBM) mechanism (see fourth boundary from the bottom), and Mechanical Twinning (MT) as is clear in the double layers bound by Shockley partial dislocations. 110

5.30	A comparison between the deformed structures of the nano-twinned copper (left) and single copper crystal (right) at a strain of 10%. Note the abundance of dissociated dislocations in the nano-twinned case and the abundance of stacking faults in the single crystal.	111
5.31	Time evolution of the relative Stacking Fault Areal Density (SFAD) for various twin layer size, and for single crystal Cu. Simulations are performed at a constant strain rate of $10^9 s^{-1}$ up to a final strain of 10%. (a) Solid line: nano-twinned crystals with lamella thicknesses of 3 nm, (b) dash line: nano-twinned crystals with lamella thicknesses of 4 nm, (c) dash dot line: nano-twinned crystals with lamella thicknesses of 5 nm, (d) dot line: single crystal.	112
5.32	A schematic diagram showing the simulation box and direction of tensile stress for nano-twinned crystals.	115
5.33	Time sequence for the deformation behavior of nano-twinned copper under a tensile stress of 2.5 GPa at 300 K, and with lamella thickness of 3 nm (10 layers are shown here). Simulations are conducted at 300 K, with a time step of 5 fs. The time sequence is as follows: (a) 32 ps, (b) 34 ps, (c) 36 ps, (d) 38 ps, (e) 40 ps, (f)42 ps, (g) 44 ps, (h) 46 ps, (i) 48 ps, (j) 50 ps, (k) 52 ps, (l) 54 ps, (m) 56 ps, (n) 58 ps, (o) 60 ps.	117
5.34	Time sequence for the deformation behavior of nano-twinned copper under a tensile stress of 2.5 GPa at 300 K, and with lamella thickness of 4 nm (7 layers are shown here). Simulations are conducted at 300 K, with a time step of 5 fs. The time sequence is as follows: (a) 32 ps, (b) 34 ps, (c) 36 ps, (d) 38 ps, (e) 40 ps, (f)42 ps, (g) 44 ps, (h) 46 ps, (i) 48 ps, (j) 50 ps, (k) 52 ps, (l) 54 ps, (m) 56 ps, (n) 58 ps, (o) 60 ps.	118

- 5.35 Time sequence for the deformation behavior of nano-twinned copper under a tensile stress of 2.5 GPa at 300 K, and with lamella thickness of 5 nm (5 layers are shown here). Simulations are conducted at 300 K, with a time step of 5 fs. The time sequence is as follows: ((a) 32 ps, (b) 34 ps, (c) 36 ps, (d) 38 ps, (e) 40 ps, (f)42 ps, (g) 44 ps, (h) 46 ps, (i) 48 ps, (j) 50 ps, (k) 52 ps, (l) 54 ps, (m) 56 ps, (n) 58 ps, (o) 60 ps. 119
- 5.36 Time sequence for the deformation behavior of single crystal copper under a tensile stress of 2.5 GPa at 300 K, and with lamella thickness of 3 nm (10 layers are shown here). Simulations are conducted at 300 K, with a time step of 5 fs. The time sequence is as follows: (a) 32 ps, (b) 34 ps, (c) 36 ps, (d) 38 ps, (e) 40 ps, (f)42 ps, (g) 44 ps, (h) 46 ps, (i) 48 ps, (j) 50 ps, (k) 52 ps, (l) 54 ps, (m) 56 ps, (n) 58 ps, (o) 60 ps. 120
- 5.37 Time sequence illustrating the cross-glide mechanism of dislocation loops in nano-twinned copper under a tensile stress of 2.5 GPa at 300 K, and with lamella thickness of 3 nm. The time sequence is as follows: (a) 43 ps, (b) 44 ps, (c) 45 ps, (d) 46 ps. Figure shows that the leading partial crosses twin boundary interfaces. 121
- 5.38 Time sequence illustrating the Twin Boundary Migration (TBM)mechanism in nano-twinned copper under a tensile stress of 2.5 GPa at 300 K, and with lamella thickness of 3 nm. The time sequence is as follows: (a) 17 ps, (b) 19 ps, (c) 21 ps, (d) 23 ps, (e) 25 ps, (f) 27 ps. Figure shows that the leading partial glides on the twin interface leading to its migration. 122

- 5.39 Time sequence illustrating the "trapping-recoil" mechanism of dislocations in nano-twinned copper under a tensile stress of 2.5 GPa at 300 K, and with lamella thickness of 4 nm. The time sequence is as follows: (a) 39 ps, (b) 40 ps, (c) 41 ps, (d) 42 ps, (e) 43 ps, (f) 44 ps, (g) 45 ps, (h) 46 ps. Figure shows that the leading partial generates from one boundary, crosses to the opposite boundary, recoils, and finally shrinks back to a small loop close to the nucleation site. 123
- 5.40 Time evolution of the total shear strain for various size nano-twin lamella thickness at an applied shear stress of 2 GPa. (a) Solid line: nano-twinned crystals with lamella thicknesses of 3 nm at 300 K, (b) dash line: nano-twinned crystals with lamella thicknesses of 4 nm at 300 K, (c) dash dot line: nano-twinned crystals with lamella thicknesses of 5 nm at 300 K, (d) dot line: single Cu crystal at 300 K, (e) dash dot dot line: nano-twinned crystals with lamella thicknesses of 3 nm at 0 K. 125
- 5.41 Time evolution of the total shear strain for various size nano-twin lamella thickness at an applied shear stress of 2.5 GPa at 300 K. (a) Solid line: nano-twinned crystals with lamella thicknesses of 3 nm, (b) dash line: nano-twinned crystals with lamella thicknesses of 4 nm, (c) dash dot line: nano-twinned crystals with lamella thicknesses of 5 nm, (d) dot line: single Cu crystal. 125
- 5.42 Time evolution of the total shear strain for various size nano-twin lamella thickness at an applied shear stress of 3 GPa at 300 K. (a) Solid line: nano-twinned crystals with lamella thicknesses of 3 nm, (b) dash line: nano-twinned crystals with lamella thicknesses of 4 nm, (c) dash dot line: nano-twinned crystals with lamella thicknesses of 5 nm, (d) dot line: single Cu crystal. 126

5.43	Time evolution of the relative stacking fault area for various size nano-twin lamella thickness at an applied shear stress of 2 GPa at 300 K. (a) Solid line: nano-twinned crystals with lamella thicknesses of 3 nm, (b) dash line: nano-twinned crystals with lamella thicknesses of 4 nm, (c) dash dot line: nano-twinned crystals with lamella thicknesses of 5 nm, (d) dot line: single Cu crystal.	126
5.44	Time evolution of the relative stacking fault area for various size nano-twin lamella thickness at an applied shear stress of 2.5 GPa at 300 K. (a) Solid line: nano-twinned crystals with lamella thicknesses of 3 nm, (b) dash line: nano-twinned crystals with lamella thicknesses of 4 nm, (c) dash dot line: nano-twinned crystals with lamella thicknesses of 5 nm, (d) dot line: single Cu crystal.	127
5.45	Time evolution of the relative stacking fault area for various size nano-twin lamella thickness at an applied shear stress of 3 GPa at 300 K. (a) Solid line: nano-twinned crystals with lamella thicknesses of 3 nm, (b) dash line: nano-twinned crystals with lamella thicknesses of 4 nm, (c) dash dot line: nano-twinned crystals with lamella thicknesses of 5 nm, (d) dot line: single Cu crystal.	127
5.46	Deformation of nano grain Cu crystals containing an initial nano-twin structure: Twin Boundary Migration and Mechanical Twinning. A shear strain of 7% is applied at 0 K. System is relaxed for 3000 steps with step size of $1 \times 10^{-15}s$. (a) An intersection view perpendicular to the grown-in twin interfaces, (b) an intersection view parallel to the grown-in twin interfaces.	130

5.47 Deformation of nano grain Cu crystals containing an initial nano-twin structure: full dislocations in two adjacent layers. A shear strain of 7% is applied at 0 K. System is relaxed for 3000 steps with step size of 1×10^{-15} s. 131

LIST OF TABLES

ACKNOWLEDGMENTS

First I would like to thank my advisor Professor Nasr M. Ghoniem, who has given me immense support and help during these past four years. He has very broad knowledge so that he can always give me guidance from a high level. Beyond that, he has been dedicated to the details of my research, and has devoted considerable time to discuss my ideas and research problems. His advice has always helped me find the right direction and go through research difficulties, and without his help, I would not have achieved what I have today. I would also like to thank Dr. Yury N.Osetskiy, because through my discussions with him, I have learnt valuable experience with Molecular Dynamics. Thanks are due to Dr. Akiyuki Takahashi, who has worked closely with me in the last year, and has given me very important help. Finally, our group members have built a pleasant and friendly environment and have been a helpful resource for me: Sam, QiYang, Jaafar, Mike, Ming, Silvester and ZhiQiang.

This work was supported by the Air Force Office of Scientific Research (AFOSR) grant number F49620-03-1-0031. Financial support through the National Science Foundation Project #CMS-0506841, entitled NIRT: Nanostructured Materials for Interconnect and Packaging Technology, is greatly acknowledged.

VITA

July 1978 Born, Guilin, China

2001 B.S., Material Science and Engineering
Tsinghua University, China

2002 M.S., Material Science and Engineering
University of California
Los Angeles, CA

2001-2006 Research Assistant
Department of Material Science and Engineering
University of California
Los Angeles, CA

ABSTRACT OF THE DISSERTATION

**Molecular Dynamics Simulations of the
Deformation of Nano-Structured Materials**

by

Lan Li

Doctor of Philosophy in Materials Science and Engineering

University of California, Los Angeles, 2007

Professor Nasr M. Ghoniem, Chair

The strength of nano-layered materials is dictated by dislocation confinement at interfaces, when an external stress is applied. In materials composed of nano-layered duplex structures, several factors influence the maximum value of the externally-applied stress before dislocations can move across the interface, and thus slip confinement is lost. The strengthening effect is a result of elastic modulus mismatch across the interface (the Koehler barrier), lattice resistance mismatch influencing the core structure (the gamma surface effect), and any coherency strains.

Recently, it has been experimentally shown that nano-twinned copper can be produced by pulsed electro-plating, and that the strength is several GPa without significant loss of electrical conductivity.

The objective of our research is to use large-scale Molecular Dynamics modelling methods to study the mechanisms of dislocation motion in multi-layer nano-structure and the interactions of dislocation with interfaces and twin boundaries. Those methods used the Embedded Atom Method for the calculation of potentials of Cu, Ni.

We present here studies of dislocation motion in Cu/Ni nano-layers utilizing Molecular Dynamics (MD) simulations, where we observed that the interfaces act as barriers for dislocation transmission, which accelerate or decelerate the motion of its partials.

We present another study of the mechanism of twin boundary migration (TBM) in copper crystals with a nano-twinned structure. We show that the mechanism of twin boundary migration is a consequence of the nucleation and motion of Schockley partial dislocations across the twin boundary.

We also studied the size effects on the deformation of nano-twinned copper. The deformation behaviors of nano-twinned Cu with different twin thickness are compared under several loading methods. The stacking fault density and the number of nucleated dislocations are compared for different size lamellae of twin structures. The present simulations reveal the origins of strengthening caused by nano-twins as the restriction of dissociated dislocation loop motion in narrow channels. A Critical twin thickness for the maximum strength in twinned copper is found to be around 4 nm.

After the introduction of the background, we presents a literature review on the theory of Molecular Dynamics Modelling and the applications of MD on the Nano-materials. The research progress and results will be discussed next and followed by a Conclusion and Summary.

CHAPTER 1

Introduction and Thesis Objectives

1.1 Brief Overview of Nano Materials

1.1.1 What are Nanomaterials?

Nanomaterials (nanocrystalline materials) are materials possessing grain sizes on the order of a billionth of a meter. They manifest extremely fascinating and useful properties, which can be exploited for a variety of structural and non-structural applications. All materials are composed of grains, which in turn comprise many atoms. An average human hair is about $100\ \mu m$ in diameter. A nanocrystalline material has grains with size on the order of 1 to 100 nm. The average size of an atom is on the order of 1 to 2 angstroms (\AA) in radius, and thus 1 nanometer comprises 3 to 5 atoms, depending on the atomic radius.

Nanocrystalline materials are exceptionally strong, hard, ductile at high temperatures, wear-resistant, erosion-resistant, corrosion-resistant, and are chemically very active. Nanocrystalline materials, or nanomaterials, are also much more formable than their conventional, commercially available counterparts. Nanomaterials research literally exploded in mid-1980s in the U. S.

There are five widely known methods to produce nanomaterials, and they are as follows:

Sol-gel synthesis, Inert gas condensation, Mechanical alloying or high-energy ball milling, Plasma synthesis, and Electrodeposition. All these processes synthesize nanomaterials to varying degrees of commercially-viable quantities.

1.1.2 Applications of Nanomaterials

Since nanomaterials possess unique, beneficial chemical, physical, and mechanical properties, they can be used for a wide variety of applications. An important problem which concerns the microelectronics industry is the reliable operation of integrated circuits (IC's), where the lifetime is limited by the failure of interconnect wires in between sub-micron semiconducting chips. In some cases, the nucleation and growth of even a single nanovoid can cause interconnect failure. Statistical mechanics cannot adequately address this situation. Future electronic and optoelectronic devices are expected to be even smaller, with nanowires connecting nano-size memory and information storage and retrieval nanostructures.

The applications of Nanomaterials include, but are not limited to, the following:

- Next-generation computer chips
- Kinetic Energy (KE) penetrators with enhanced lethality
- Better insulation materials
- Phosphors for high-definition TV
- Low-cost flat-panel displays
- Tougher and harder cutting tools
- Elimination of pollutants
- High energy density batteries
- High-power magnets
- High-sensitivity sensors

- Automobiles with greater fuel efficiency
- Aerospace components with enhanced performance characteristics
- Better and future weapons platforms
- Longer-lasting satellites
- Longer-lasting medical implants
- Ductile, machinable ceramics
- Large electrochromic display devices

1.2 Nano-Laminates and Nano Twins

Materials with a nano-laminate structure have been manufactured to enable a new class of optical structures that are ultra-lightweight, dimensionally stable, resistant to environmental effects, have low cost and are fast to manufacture. Also, more recently, using pulsed electrodeposition, copper samples have been fabricated to have a unique nano-twinned structure. We will discuss here the merits if these two material systems.

1.2.1 Nano-Laminates

Atom-by-atom deposition of different metals into many very thin layers opens the door to the creation of a new realm of composite materials with incomparable levels of strength and toughness. Nano-Laminates are man made layered structures synthesized atom by atom using sputter deposition technology. Another fabrication method is severe deformation.

Figure 1.1 shows a Cross-section Transmission Electron Microscopy image of a multi-period ZrC/Si Nano-Laminate fabricated by sputter deposition for X-ray

Optic Applications[85]. The thickest dark ZrC layers are 5.77 nm thick. The thick Si layers are 6.73 nm thick. The thinnest layers (ZrC - 0.36 nm and Si - 0.42 nm) are not observable in this lower magnification image but are seen at higher magnifications



Figure 1.1: A multi-period ZrC/Si Nano-Laminate[85].

Another test sample shown here consists of thousands of alternating layers of copper and niobium. Each layer has a thickness of only a few nanometers. At these nanometer-scale layer thicknesses, the material deforms in ways that are very different from that of conventional materials.

Nano-laminates are synthesized using atom by atom physical vapor deposition

sequential magnetron sputtering. Elemental materials, alloys or compounds are sputtered producing individual layers having a thickness ranging from a single monolayer (0.2 nm) to hundreds of monolayers (> 500 nm). Macroscopic sample thickness up to $400 \mu\text{m}$ has been demonstrated. Nanolaminates allow direct and perfect replication off of a master tool.

Nano-laminates are a new class of materials that are capable of approaching theoretical limits of strength. This property is important because high specific strength produces a more durable material at smaller cross sectional areas and supports surface quality. Additionally, as metals typically have stiffness larger than that characteristic of glasses, metallic nano-laminate materials will perform better as thin foil structures.

At these nanometer-scale layer thicknesses, the material deforms in ways that

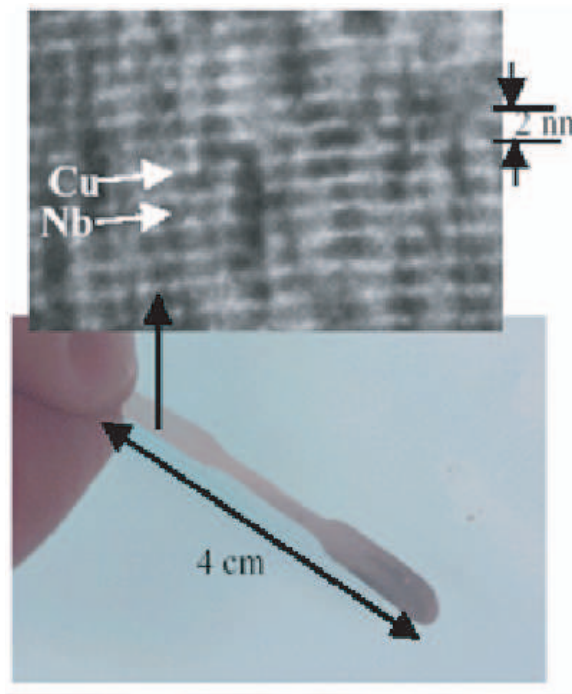


Figure 1.2: A nano-laminate of copper and niobium

are very different from that of conventional materials. They show incomparable strength, toughness, and unique deformation mechanisms. The present research is aimed at the exploration of new concepts in the physics of strengthening of ultra-fine scale materials. Figure 1.3 shows that composites of nano-layered metals can

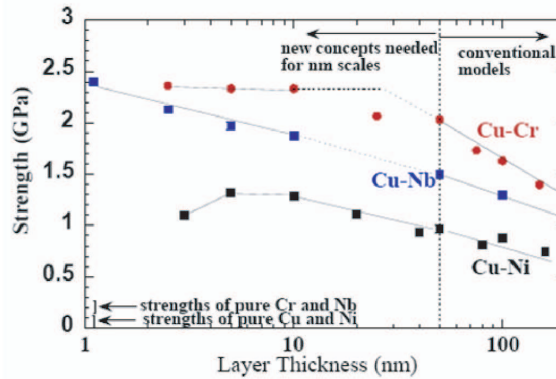


Figure 1.3: Strength (estimated as hardness divided by 3) vs. the layer thickness of several Cu-based multi-layers, and compare to pure metals (estimated at $10 \mu\text{m}$ grain size). [Data is from Los Alamos National Laboratory].

achieve strength levels that are 100 to 1000 times greater than the conventional strength of individual components. This graph shows how strength depends on layer thickness in several different combinations of layered composites. We see that in some cases, but not all, the strength tends to reach a maximum.

1.2.2 Nano-Twinned Cu

Figure 1.4 shows the (111) plane in an face cubic crystal (FCC) structure. (111) is the plane with the highest atomic packing factor, which means that the density of atoms on this plane is the highest compared to any other plane in the FCC crystal structure.

When adjacent parts of a crystal are regularly arranged such that one part is a mirror image of the other, the two parts are said to be twin related.

Figure 1.5 shows a twin boundary structure within an FCC crystal.

Recently, high-purity Cu samples with nanoscale growth twins were synthesized using a pulsed electrodeposition technique from an electrolyte of $CuSO_4$

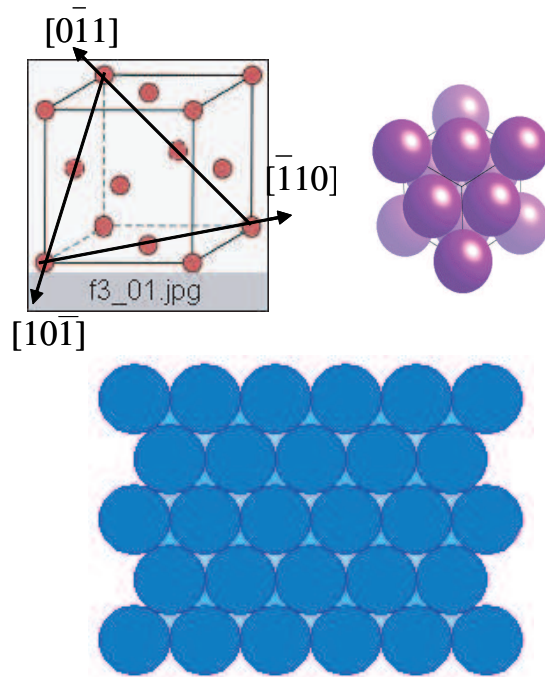


Figure 1.4: Atomic packing of the (111) plane in an FCC crystal

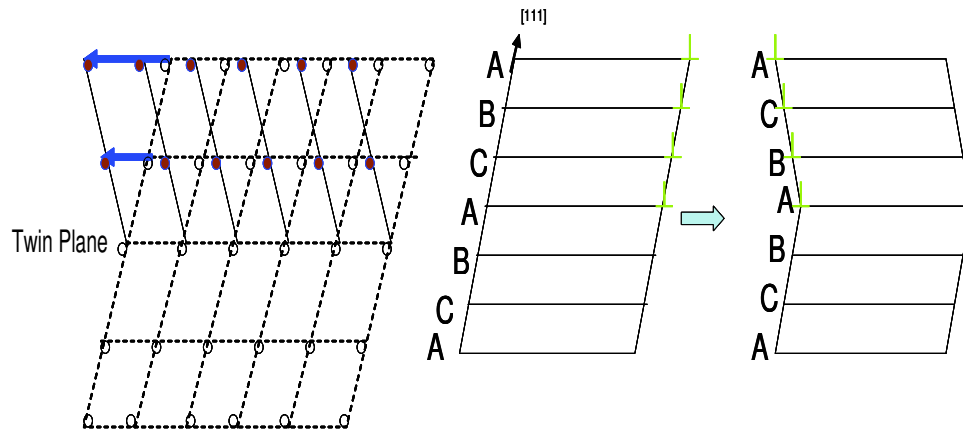


Figure 1.5: A twin boundary in FCC crystal

[48]. Transmission electron microscopy (TEM) observations (Fig. 1.6) indicated that the as-deposited Cu consisted of irregular-shaped grains with random orientations. The grain sizes were between 100 nm and 1 μm , with an average value of about 400 nm (Fig. 1.6B). Each grain contained a high density of growth twins of the 111/[112] type. Measurements of the lamella thickness along the [110] orientation showed a wide distribution ranging from several nanometers to about 150 nm (Fig. 1.6C), due to the fact that in this orientation, only ($\bar{1}11$) and ($11\bar{1}$) twins are edge-on, whereas (111) and ($11\bar{1}$) twins are inclined to the surface. The lamella thickness distribution showed a peak at about 15 nm, corresponding approximately to the average lamella thickness for the edge-on twins. The length of twin lamellar geometry varied from about 100 nm to 1 μm (the grain diameter). The high-density growth twins separated submicron-sized grains into nanometer-thick twin/matrix lamellar structures. Close TEM observations and high-resolution TEM images showed that most TBs were perfectly coherent and atomically sharp (Fig. 1.6 , D and E).

For conducting materials in many applications, high electrical conductivity and high mechanical strength are often required simultaneously. However, pure metals with high conductivities such as Ag, Cu, and Al are very soft. Strengthening the metals via various approaches, including solid solution alloying, cold working, and grain refinement, leads to a pronounced decrease in conductivity. For example, alloying pure Cu may increase the strength by two or three times, but the electrical conductivity of Cu alloys is only 10 to 40% that of pure Cu.

Tensile tests of as-deposited Cu foils performed at ambient temperature showed an extremely high strength (Fig. 1.7A) [48]. The tensile yield strength σ_y (at 0.2% offset) reached as high as 900 MPa, and the ultimate tensile strength (UTS) was 1068 MPa. These values are at least one order of magnitude larger than those

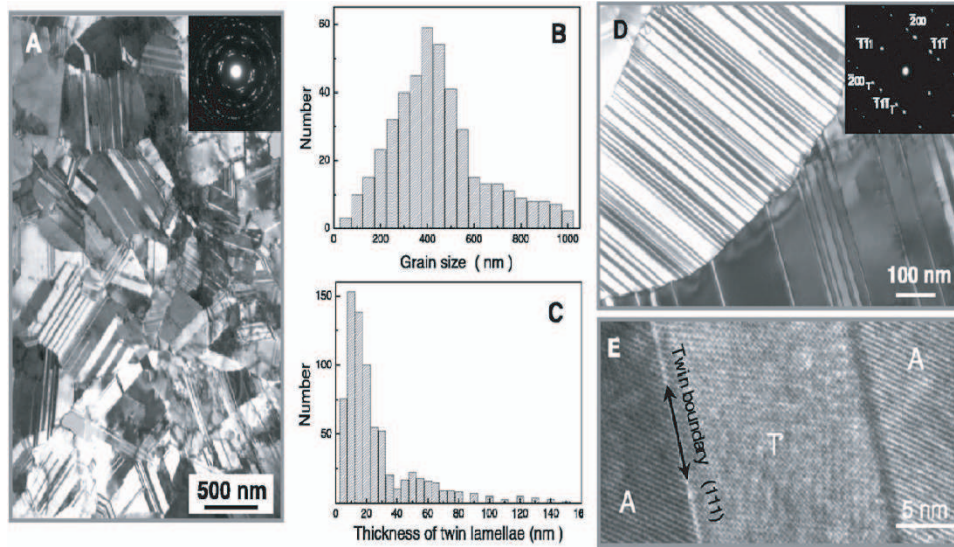


Figure 1.6: TEM observations of the typical microstructure in an as-deposited Cu sample [48]. A bright-field TEM image (A) and the electron diffraction pattern (inset) show roughly equiaxed submicrometer-sized grains with random orientations separated by high-angle GBs. The statistical distributions for grain size (B) and for thickness of the twin/matrix lamellae (C) were obtained from the many TEM images of the same sample. Electron diffraction patterns [inset in (D)] indicate that the twins in each grain are parallel to each other in 111 planes (D), and high-resolution TEM images (E) show that the twins follow a sequence of ATATA..., with twinning elements, for example, A: $(\bar{1}\bar{1}\bar{1})/[\bar{1}\bar{1}2]$ and T: $(\bar{1}\bar{1}\bar{1})/[\bar{1}\bar{1}2]$

of the coarse-grained (grain size $> 100\mu m$) Cu samples. The strength values are higher than those reported for polycrystalline pure Cu with three-dimensional grain sizes down into the nanometer scale (Fig. 1.7A).

Figure 1.7B displays the measured temperature dependence of the electrical resistivity (ρ) for the as-deposited Cu sample with nanoscale twins in comparison with the coarse-grained one. The electrical resistivity of the nanotwin Cu sample is very close to that of the coarse-grained Cu specimen over the whole measured temperature range. For comparison, the electrical resistivity of a nanocrystalline Cu foil (with conventional Grain Boundaries and an average grain size of 15 nm) made by means of magneto-sputtering was also measured in the same temperature range (Fig. 1.7B). The resistivity values in the whole temperature range were at least one order of magnitude higher than that for the nano-twin Cu sample.

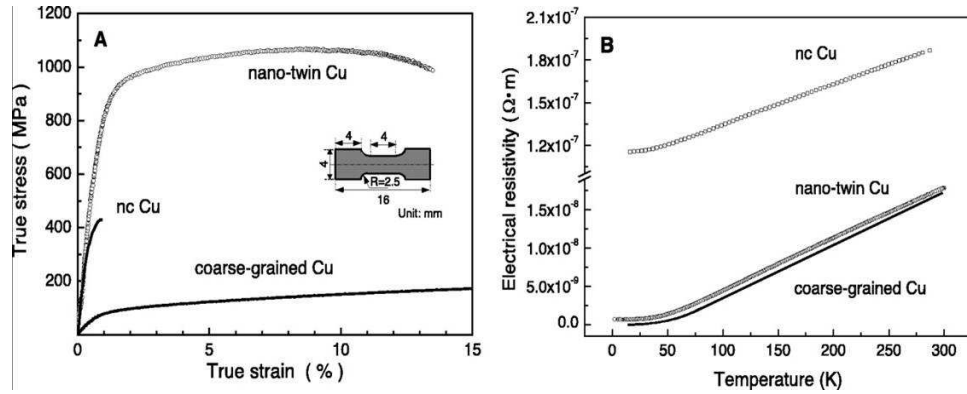


Figure 1.7: (A) A typical tensile stress-strain curve for the as-deposited Cu sample with nano-twins in comparison with that for a coarse-grained polycrystalline Cu sample (with an average grain size larger than $100\mu m$) and a nanocrystalline (nc) Cu sample (mean grain size 30 nm) (11). The inset shows the geometry of the tensile sample for the as-deposited nano-twin sample (R, radius of curvature). (B) The measured temperature dependence of electrical resistivity (ρ) for the as-deposited nano-twin Cu sample and the coarse-grained sample in a temperature range from 2 to 296 K. For comparison, electrical resistivity measurement results in a nanocrystalline Cu sample with a mean grain size of 15 nm are also included. Data taken from reference [48]

1.2.3 Applications– the Strongest Metals Ever Known

Nano-scale design shows promise of synthesizing the strongest metals ever known to mankind. Recent interest in nanotechnology is challenging the scientific community to analyse, develop and design nanometer to micrometer-sized devices for applications in new generations of computers, electronics, photonics and drug delivery systems. Some examples of the application areas are:

- Micro-electronics interconnects
- Opto-electronics Laser mirrors
- Aircrafts structures
- Rocket engine chamber walls Ultra-hard
- Nano-scale sensors and actuators
- Ultra-High Strength Materials
- Magnetic Transducers - GMR
- High Performance Tribological Coatings
- EUV, Soft X-ray and X-ray Optics
- Coatings for Gas Turbine Engines
- Microcircuit Lithography Development
- High Performance Visible Optics
- High Performance Capacitors
- Integrated Circuit Interconnects

- New Materials and New Devices Based on the Chemical and Structural Control Available with Engineered Nano-Laminate Materials
- Basis for New Manufacturing Strategy

1.2.4 Why are Nano-Layered Structures so Strong?

The flow stress in nano-layered structures can approach to within 1/3 of the theoretical shear strength of order $\mu/30$, where μ is the shear modulus.

The strength mechanism is understood to be the result of restricting the motion of dislocations from one layer to another. Understanding the mechanics of such nano-engineered devices will enable high levels of reliability and useful lifetimes to be achieved. Restricted motion of dislocations in nano-layered materials is a result of several factors, as listed below:

- Modulus Mismatch (Koehler Effect)
- The Lattice Parameter Mismatch
- The Chemical Mismatch (Stacking Fault Energy)
- Slip plan geometry mismatch
- Dislocation Core Spreading into the Interface
- Misfit Dislocations at a Semi-coherent or Incoherent Interface

Undoubtedly, defects are expected to play a major role in these nanosystems and microsystems owing to the crucial impact on the physical and mechanical performance. Those defects effect could be:

- Unstable stacking fault energy of the incoming and outgoing slip planes

- Creation of a residual dislocation at a semi-coherent or incoherent interface during transmission
- Dissociation of the dislocation into partials that can be separated or contracted by non-glide components of stress (the Escaig effect)
- Ordering mismatch across interfaces

The present research is aimed at developing an understanding of the origins of this behavior so that materials can be tailored to reach even higher strength levels.

1.3 Computer Simulations on Materials

The development of ultra-strong, yet ductile materials by combining nano-layers with different microstructure also requires detailed understanding of their mechanical properties. Such materials, if properly designed, may be candidates for many demanding applications (e.g. micro-electronics, opto-electronics, laser mirrors, aircraft structures, rocket engines, fuel cells, etc.).

The new exciting application areas require novel and sophisticated, physically based approaches for design and performance prediction. Thus theory and modelling are playing an ever-increasing role in this area to reduce development costs and manufacturing times.

Experimental studies on Nano-materials have many limitations:

- The experiments always produce complex microstructures such as nano-crystalline columnar grains, etc. All the microstructures exert an influence on the results.
- Observation is due to many factors

- The influence of the substrate

Understanding the deformation mechanisms can help us to design nanostructured materials for both high strength and high ductility. However, due to the physical size restriction, the current experimental tools have been mainly limited to only a few methods such as pointed indenters, scratch-type tests and bulge tests.

Computer simulation of material behavior has become an indispensable tool, and is now playing an increasingly significant role to complement traditional theoretical and experimental research. Large-scale computer simulations may provide an additional investigative tool to augment, interpret and plan experimental techniques for mechanical properties at nano- to micro- length scale.

Continuum methods for prediction of the mechanical properties of nano- structures fail to describe their plastic deformation and subsequent failure. Therefore, fundamental models of plasticity, based on dislocation dynamics and atomistic computer simulation methods are necessary to accurately predict the strength and plastic deformation at the nano- length scales. Molecular dynamics (MD) is a useful atomistic simulation method that can give out the full information about each atoms.

In the following chapters, a literature survey for the related topics including experimental and theoretical research is reviewed in Chapter 2. The computational method of molecular dynamics utilized through this thesis is presented in Chapter 3, and our results on nano-laminated Cu/Ni composites are given in Chapter 4. Results of MD simulations of the strength of nano-twinned copper are then given in Chapter 5. Finally, conclusion and future directions are discussed in chapter 6.

1.4 Thesis Objectives

The overall objectives of this dissertation can be stated as follows:

- Gain understanding of the mechanics of ultra-strength of Nano-layered structure materials.
- Develop a model for studying nano laminated Cu/Ni structure and nano twinned Cu in single and polycrystalline configurations.
- Develop a method to distinguish twins from other defects
- Analyze the dislocation motion in nano-layered structures, the interaction of dislocations with interfaces, and the conditions for confinement and transmission.
- Ultimately determine the dependence of strength on nano-twin size, and explain how material properties affect the strength, and gain a sense as to what direction the manufacturing of the nano-structure materials must proceed.

CHAPTER 2

Review of Theoretical Research on the Strength of Nano-structured Materials

In this chapter, we first briefly introduce the different length scales in the simulation of nano-structured materials, followed by detailed review of the Molecular Dynamics (MD) simulation method. We present the essential details of empirical interatomic potentials, and introduce the idea of Multi-scale simulation. Then we will review the current application of MD simulation in studies of the deformation of nano-materials. Finally, we discuss the various theoretical mechanisms that attempt to explain the extraordinary strength of nano-structured materials.

2.1 Computational Methods for Studies of the Mechanical Behavior of Nano-structured Materials

2.1.1 Ab-initio Simulations

Most of the low-energy physics, chemistry, materials science, and biology can be explained by the quantum mechanics of electrons and ions. The quantum mechanical description of events on the atomic scale in most cases give the properties and behavior of materials.

Without quantum-mechanical modelling, we can still solve many problems in materials science. However, when one goes into the atomic world, the traditional method is often limited. For instance, classical elasticity theory gives the understanding of the properties of dislocations, however, until recently, the nature of the core of a dislocation or the effect of chemistry on the core was still known very little, because this part of the dislocation requires detailed quantum-mechanical

modelling.

Quantum mechanics has the ability to predict the total energy and the atomic structure of a system of electrons and nuclei, which makes a quantum mechanical calculation directly useful.

The Schrödinger equation can be used to calculate a wide range of physical properties of materials. There are many methods to solve this equation requiring only a specification of the ions present (by their atomic number). These methods are usually referred to as *ab initio* methods.

2.1.2 Atomistic Simulations

The *ab initio* methods presented in Section (2.1.1) are rigorous but limited by present day computers to systems containing a few hundred atoms at most. Such methods serve two important purposes. First, they provide direct information on the response of materials to external environments (e.g. force and temperature). Second, they also generate a database of properties that can be used to construct effective (empirical) interatomic potentials. To determine the properties of an ensemble of atoms larger than what can be handled by computational quantum mechanics, the description of the atomic interactions must be approximated. The Molecular Dynamics (MD) method is developed to enable studies of the properties of material volumes containing millions to billions of atoms with effective interatomic potentials. The basic idea is to eliminate all electronic degrees of freedom, and assume that the electrons are glued to the nuclei. Thus, the interaction between two atoms is represented by a potential function that depends on the atomic configuration (i.e. relative displacement) and the local environment (i.e. electrons). Based on the electronic structure database, or alternatively using experimental measurements of specific properties, approximate effective potentials

can be constructed. According to classical Newtonian mechanics, the dynamic evolution of all atoms can be fully determined by numerical integration. In principle, once the positions and velocities of atoms in the finite ensemble within the simulation cell are known, all thermodynamic properties can be readily extracted. There are two methods used to simulate dynamical ensembles of atomic systems at larger length scales, and these are the Molecular Dynamics (MD) and Monte Carlo (MC) methods.

2.1.3 Computational Mesomechanics

Studies of the mechanical behavior of materials at a length scale larger than what can be handled by direct atomistic simulations, and smaller than what allows macroscopic continuum averaging represent particular difficulties. When the mechanical behavior is dominated by microstructure heterogeneity, the mechanics problem can be greatly simplified if all atomic degrees of freedom were adiabatically eliminated, and only those associated with defects are retained. Because the motion of all atoms in the material is not relevant, and only atoms around defects determine the mechanical properties, one can just follow material regions around defects. Since the density of defects is many orders of magnitude smaller than the atomic density, two useful results emerge. First, defect interactions can be accurately described by long-range elastic forces transmitted through the atomic lattice. Second, the number of degrees of freedom required to describe their topological evolution is many orders of magnitude smaller than those associated with atoms. Thanks to many computational advances during the past two decades, the field has steadily moved from conceptual theory to practical applications. While early research in defect mechanics focused on the nature of the elastic field arising from defects in materials, recent computational modelling has shifted the emphasis on defect ensemble evolution.

Two of the most fascinating features of micro-scale plasticity are the spontaneous formation of dislocation patterns, and the highly intermittent and spatially localized nature of plastic flow. Dislocation patterns consist of alternating dislocation rich and dislocation poor regions usually in the μm range (e.g. dislocation cells, sub-grains, bundles, veins, walls, and channels). On the other hand, the local values of strain rates associated with intermittent dislocation avalanches are estimated to be on the order of 1 to 10 million times greater than externally imposed strain rates [63] [98]. Understanding the collective behavior of defects is important because it provides a fundamental understanding of failure phenomena (e.g. fatigue and fracture). It will also shed light on the physics of self-organization and the behavior of critical-state systems (e.g. avalanches, percolation, etc.)

2.2 Multi-scale Simulation and Atomistic/Continuum Coupling Method

Recent research has focused on a multi-scale modelling approach to achieve a comprehensive understanding of the mechanism of dislocation nucleation and movement in stressed multi-layer structures. Here, the essence of the multi-scale modelling approach is the proper choice of coupling between different length scales, this can explain and guide the results of atomistic models and inversely give a reasonable description of the parameters in the macroscopic level.

Appropriate validation experiments are crucial to model verification. Models must predict the correct behavior at each length scale. However current nano and micro-scale mechanical experiments have been mostly limited to indentation [47] [94] and bulge tests [81] [6], and to non-contact tests such as X-ray residual stress measurements [38] [78]. Multi-scale interconnected approaches will need to be developed to interpret new and highly specialized nano / micro-mechanical

tests. One of the advantages of these approaches is that, at each stage, physically meaningful parameters are predicted and used in subsequent models, avoiding the use of empiricism and fitting parameters.

As the material dimensions become smaller, its resistance to deformation is increasingly determined by internal or external discontinuities (e.g. surfaces, grain boundaries, dislocation cell walls, etc.). The Hall-Petch relationship has been widely used to explain grain size effects, although the basis of the relationship is strictly related to dislocation pileups at grain boundaries. Recent experimental observations on nano-crystalline materials with grains of the order of 10 to 20 nm indicate that the material is weaker than what would be expected from the Hall-Petch relationship [20] [12]. Thus, the interplay between interfacial or grain boundary effects and slip mechanisms within a single crystal grain may result in either strength or weakness, depending on their relative sizes. Although experimental observations of plastic deformation heterogeneities are not new, the significance of these observations has not been addressed till very recently. In same metallic alloys, regular patterns of highly localized deformation zones, surrounded by vast material volumes which contain little or no deformation, are frequently seen [57] [58] [2]. The length scale associated with these patterns (e.g. typically the size of dislocation cells, the ladder spacing in persistent slip bands (PSB's), or the spacing between coarse shear bands) controls the material strength and ductility. As it may not be possible to homogenize such types of microstructure in an average sense using either atomistic simulations or continuum theories, new intermediate approaches will be needed.

2.3 Theoretical Mechanisms for the Strength of nano-structured Materials

2.3.1 Hall-Petch Approach

The Hall-Petch relationship has been widely used to explain grain size effects. When a queue of dislocations is forced against some obstacle by the applied stress, the queue is called a dislocation pileup. Figure 2.1 shows an example of the pileup of edge dislocations pushed against an interface, which blocks the motion of the leading dislocation. The leading dislocation is acted upon not only by the applied stress, but also by the interaction force with the other dislocations in the pileup. The pileup concentrates on the leading dislocation a large force proportional to the applied stress and to the number of dislocations in the pileup. An inverse square root dependence of the flow stress (or by analogy, the hardness and ultimate tensile strength) on the layer thickness in the nanolaminate is predicted with the Hall-Petch mechanism. Recent experimental observations on nano-crystalline materials with grains of the order of 10 to 20 nm indicate that the material is weaker than what would be expected from the Hall-Petch relationship. The theory must be modified to account for two facts, first that, when d is small, the number of dislocations in a pile up is small and discrete. And second, the interface barrier itself depends strongly on d . The first modification progressively reduces the Hall-petch slope as d decreases, eventually to zero at the saturation point, when dislocations cross interfaces unaided by pileups. The second modification, that is not a constant but falls as d falls, creates a peak in the plot of stress against thickness, this peak defines the strongest size for the multilayer.

The shear stress at the tip of the pileup is approximately given by

$$\tau_p \propto N\tau_a \quad (2.1)$$

where τ_p is the shear stress at the tip of the pileup, N is the number of dislocations in the pileup, and τ_a the applied shear stress. It can be shown that the shear strength of the pileup, τ_{HP} , which is resisted by the interface barrier strength τ^* , is given by

$$\tau_{HP} = \tau_0 + \frac{k_{HP}}{\sqrt{d}} \quad (2.2)$$

$$k_{HP} = \sqrt{\frac{\mu b \tau^*}{\pi}} \quad (2.3)$$

where τ_0 is the lattice resistance stress.

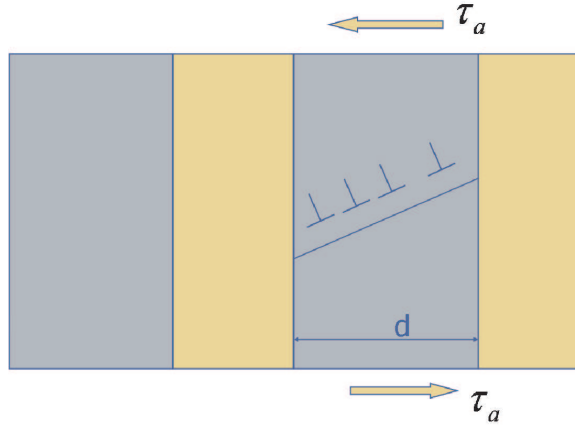


Figure 2.1: Hall-Petch approach

2.3.2 The Koehler Barrier

The Barrier Strength of the Interfaces τ^* is a result of several factors, as listed below:

- The Modulus Mismatch (Koehler Effect)

- The Lattice Parameter Mismatch
- The Chemical Mismatch
- Geometrical Mismatch

In the Hall-Petch model, the most important parameter is the barrier strength, τ^* , which may be thought to have four separate components resulting from four mismatches between adjacent layers. The energy of a dislocation must rise as it passes from a layer with low μ to one with high μ . Consequently, a force opposes this passage. Van der Merwe dislocations at the interface block a glissile dislocation crossing the interface and cause it to bow between the mismatch dislocations. The line energy of a dislocation depends on its core structure and the width of its stacking fault. An increase in this core energy from one layer to another generates a barrier at the interface. If the slip planes or Burgers vectors do not match on the two sides of an interface, the glissile dislocation may leave a difference dislocation in the interface, or acquire jogs, or, in the case of a screw crossing a twin interface, may cross-slip. The dislocations are attracted to the lower modulus material, and accumulate within that layer if transmission is possible and will pileup along the interface if transmission is not possible. Elastic analysis of dislocation transmission across two semi-infinite layers of different shear moduli (μ_1 and μ_2) predicts an inverse first power relationship between the maximum shear strength, τ^* , and the layer thickness, h :

$$\tau_K^* = \frac{\mu_1(\mu_2 - \mu_1)b}{4\pi(\mu_2 + \mu_1)h} \quad (2.4)$$

2.3.3 The Peierls-Nabarro Model

While the continuum elasticity theory predicts well the long range elastic field of a dislocation, it suddenly breaks down within a few atomic spacings surrounding

the dislocation core. The Peierls-Nabarro model is useful in determining the width of a dislocation and in estimating its core energy.

As shown in Figure 2.3 [32], let us consider two semi-infinite simple cubic crystals, with their cube axes parallel, but with an initial disregistry in the x direction. Initially the disregistry of the bottom half-plane with respect to the top one is Φ^0 (see Figure 2.3(a)).

$$\phi_x^0 = \begin{cases} \frac{b}{2}, x > 0 \\ -\frac{b}{2}, x < 0 \end{cases} \quad (2.5)$$

The displacement $u(x)$, are now imposed on the two half-crystals (figure 2.3(b)), which are then joined to form the edge dislocation. The disregistry in the latter case is:

$$\phi_x(x) = \begin{cases} 2\mu_x(x) + \frac{b}{2}, x > 0 \\ 2\mu_x(x) - \frac{b}{2}, x < 0 \end{cases} \quad (2.6)$$

We can also see from the Figure 2.3(b) that at the boundary, the displacement $u(x)$ will have the value as:

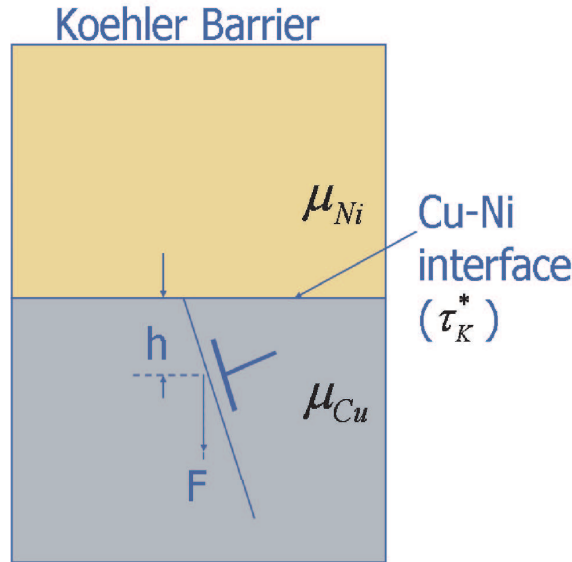


Figure 2.2: Schematic illustration of the Koehler effect.

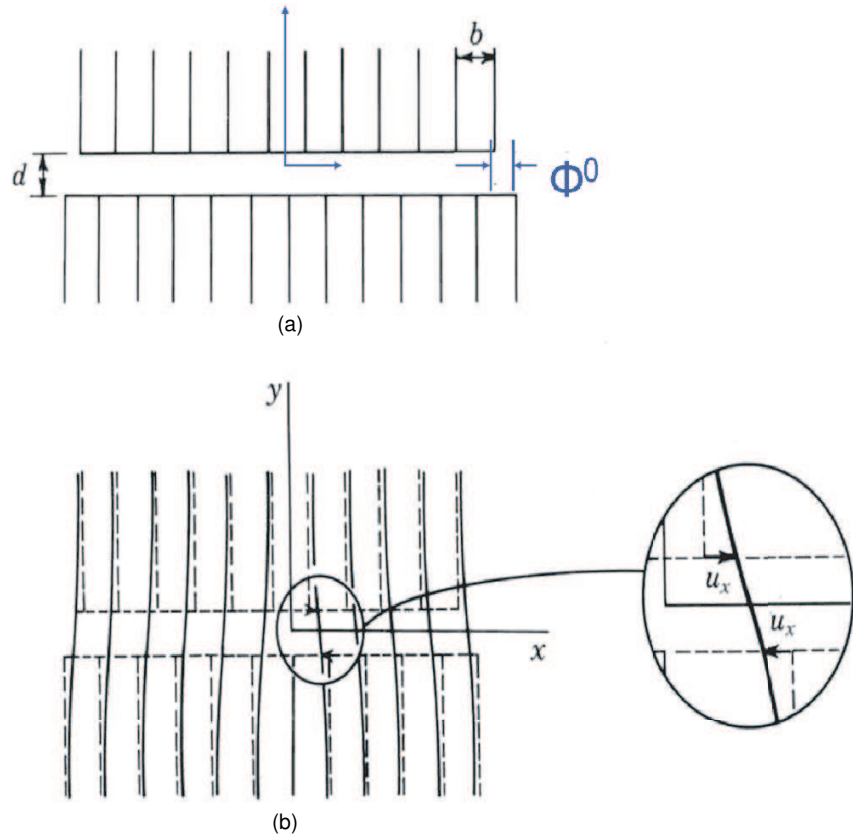


Figure 2.3: Two semi-infinite simple cubic crystals with disregistry in the x direction form an edge dislocation.[32]

$$\mu(-\infty) = \frac{b}{4} \quad (2.7)$$

$$\mu(+\infty) = -\frac{b}{4} \quad (2.8)$$

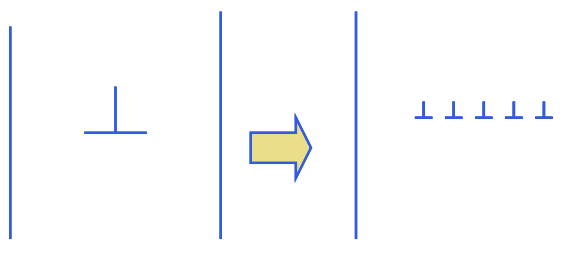


Figure 2.4: Infinitesimal dislocations replace the original single dislocation in the Peierls-Nabarro model. [32]

The Peierls-Nabarro model uses a continuous distribution of infinitesimal dislocations to replace the original single dislocation (see Figure 2.4). Let $b(x)dx$ be the Burgers vector of the infinitesimal dislocation lying between x and $x + dx$. The differential equation of $b(x')dx'$ will be:

$$b(x')dx' = \frac{du(x')}{dx'}dx' \quad (2.9)$$

The integral equation of $b(x')$ is:

$$b = \int_{-\infty}^{+\infty} b(x')dx' \quad (2.10)$$

Stress field will generated at x due to the infinitesimal dislocations between lying x' and $x' + dx'$ with Burgers vector $b(x')dx'$, can be calculated by:

$$\frac{K}{2\pi} \frac{1}{x - x'} \frac{du(x')}{dx'} \quad (2.11)$$

where K depends on the type of dislocation and the crystalline direction.

If we do the integral over the stress field over the x space, we will get so-called

restoring stress σ_p at x :

$$\sigma_p[u(x)] = \frac{K}{2\pi} \int_{-\infty}^{+\infty} \frac{1}{x-x'} \frac{du(x')}{dx'} dx' \implies u(-\infty) = \frac{b}{4}; u(+\infty) = -\frac{b}{4} \quad (2.12)$$

On the other hand, the restoring stress is caused by distorted bonds in lattice, and is given by the the gradient of the so-called generalized stacking fault energy (or γ surface).

$$\sigma_p[u(x)] = -\frac{\partial\gamma}{\partial u} \quad (2.13)$$

In the original Peierls-Nabarro model, a sinusoidal form of the restoring force is assumed:

$$\sigma_p[u(x)] = \tau_{max} \sin\left(\frac{2\pi u(x)}{b}\right) \quad (2.14)$$

Analytical solutions of the Peierls-Nabarro model are available when the restoring force is sinusoidal. Let

$$\tau_{max} \cong \frac{\mu b}{d}; K = \frac{\mu}{(1-\nu)} \quad (2.15)$$

Then, the displacement is given by [32]:

$$u_x(x) = \frac{b}{\pi} \tan^{-1} \frac{x}{\zeta} \quad (2.16)$$

where $\zeta = \frac{d}{2}(1-\nu)$, is half dislocation width. The solution is also shown in Figure 2.5.

2.4 MD Simulations in Nano-mechanics

This section focuses on a review of the applications of MD simulations to mechanics problems at the nano-scale. Furthermore, we focus on nano-mechanics of point defects, dislocations, and interfaces (free surfaces and grain boundaries)

under applied stress. Mechanics of nanotubes have also received much attention [19], but will not be treated here.

We start with point defects. Under stress, the normal diffusion process governed by point defect motion is polarized by the action of the stress field. The diffusion process of a point defect has been investigated by a combination of molecular statics (MS) and MD simulations. Diffusion anisotropy, which is intrinsic in low symmetry crystals, can be enhanced by the action of stress [92]. The stress effect on a point defect, particularly its formation and migration energies, is crucial to the analysis of kinetic processes, but this is usually not a first order effect in nano-mechanics.

The second type of defect, dislocation, has received much attention in nano-mechanics. In the following, we analyze the nano-mechanics of dislocations in terms of statics and dynamics. In dislocation statics, one is primarily concerned with the final core structure of one or a few dislocations. The discovery of three-fold symmetry of a screw dislocation in BCC metals is a beautiful example of applications of dislocation statics [88, 18, 71, 95, 90]. During dislocation motion, many processes are involved; dislocation damping, dislocation intersection, and dislocation clustering, just to name a few. MD simulations have provided much insight to details of kink-kink [10], dislocation-dislocation [96, 100, 75, 74], dislocation-point-defect [39], and dislocation-grain boundary [65]. In the tran-

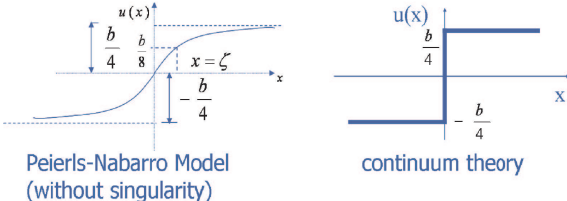


Figure 2.5: Analytical solution for Peierls-Nabarro model

sonic velocity range, MD simulations have revealed new mechanisms and possibilities. Gumbsch and Gao [28] demonstrated that transonic dislocations are possible. Later, it was shown that a transonic dislocation can cross the sound barrier back and forth [79, 46]. The availability of fast dislocations also enabled the study of dislocation dipole stability at the atomic level [91], to serve as direct confirmation of the elasticity analysis [35]. As shown in Fig. 2.6, the simulations further reveal that a dislocation dipole can be stabilized even with an overshoot; a direct result of the finite speed of wave propagation.

In addition to the static and dynamic behavior, the nucleation of dislocations is another important area of nano-mechanics. MD simulations have been applied in studies of dislocation emission from crack tips [89], nucleation of dislocations from surfaces [44, 45], and dislocation nucleation in nanocrystals [86, 15]. One of the challenging problems that remain is treating the interaction of boundaries with elastic waves emitted by a moving dislocation. It is usually necessary to separate this interaction from the true dynamics of a moving dislocation. Several recent studies have attempted to damp out boundary effects [42, 11, 91], but the problem is still not satisfactorily solved.

Similar to point defects and dislocations, interfaces (e.g. surfaces and grain boundaries) respond to mechanical loading. In connection with dislocations, surfaces are nucleation sites. Although grain boundaries also have this function, they are more crucial in facilitating or blocking other deformation mechanisms. Using a multiscale approach, [65] have studied the interaction of a dislocation with a grain boundary. It is well established that grain boundaries serve as barriers to dislocation motion and give rise to the Hall-Petch effect, which shows that the strength of materials is inversely proportional to the square root of its grain size. However, for materials with grain sizes below a few nanometers, materials

strength begins to decline when the grain size decreases [87]. At the nanoscale, grain boundaries facilitate mechanical deformation through grain boundary sliding. At the same time, the grain structure evolves as well, and this evolution in turn affects the mechanical deformation. Taking thin slices of polycrystalline nano-grains, Wolf and co-workers [77, 76] have investigated mechanisms of grain boundaries interactions. As shown in Fig. 2.7, high-angle grain boundaries shrink and that quadruple junctions are not stable and are reduced to triple junctions.

The presentation in this section has so far focused on physical aspect of nano-mechanics. This physical understanding relies on identification and analysis of point defects, dislocations, and interfaces. Among the three types of defects, dislocation is probably the most difficult to characterize or identify. The identification is straightforward if the dislocation configuration is simple. One may rely on constructing the Burgers circuit, using disregistry functions (such as the Centrosymmetry parameter), or tracking the atomic level stress or energy [13, 30, 31]. When complex dislocation configurations are involved, unambiguous identification of dislocation cores may require a combination of several of the methods

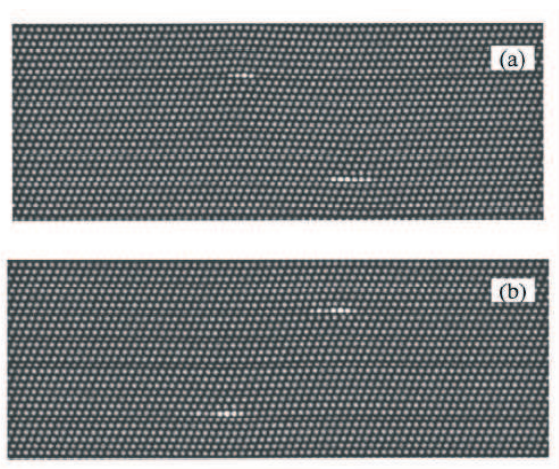


Figure 2.6: Three snapshots of a pair of edge dislocations in a dipole configuration, showing the stabilization of a dipole despite the dynamic overshoot [?]

discussed above. There is still not a universal characterization method that fits all purposes.

Before closing this section, let's examine the type of information that can be passed on to larger length scales. Here, we consider three types of defects: point defect, dislocation, and interface (particularly grain boundary). Information on defect energetics and diffusion tensors obtained by MD or MS simulations provide parameters to rate equations and Monte Carlo methods describing microstructure evolutions. Dislocation energetics (e.g. kink-pair formation energy and dislocation core energy), Peierls stress and dislocation mobility are used as input parameters in dislocation dynamics simulations at the mesoscopic level [89]. Finally, dislocation nucleation conditions and interaction mechanisms with other defects (dislocations or grain boundaries or other interfaces) from MD simulations are critical to dislocation dynamics simulations.

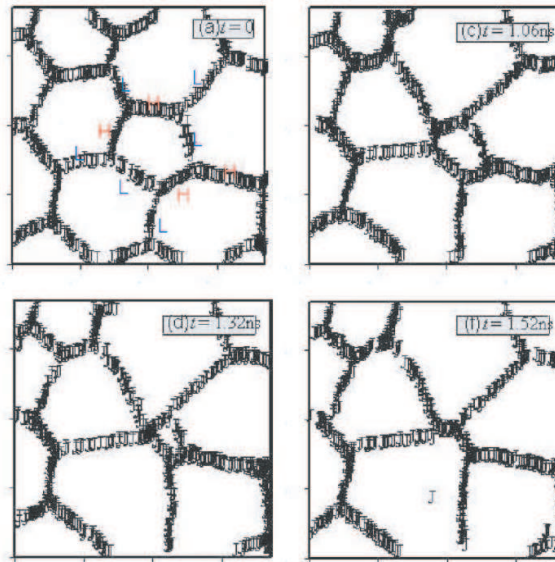


Figure 2.7: MD simulations of nano-scale grain boundary evolution under externally applied stress . Time is labelled in each frame. "H" indicates high-angle, and "L" low-angle grain boundary [76].

2.4.1 Molecular Dynamics Simulations of Nano-layered Structures

Nano-crystalline Cu materials have revealed very high twin densities prior to deformation [61]. When high shear stresses are applied, mechanical twinning is observed as a deformation mechanism [97]. During high-pressure torsion of Cu, mechanical twinning is observed [23]. Extended partials are not the exclusive nc deformation mechanism: in situ analysis technique recently developed at the Swiss synchrotron light source showed no change in the stacking fault density [9]. In ultra-fine grained Cu with an average grain size of 400 nm the strain rate sensitivity and the ductility both increase when the TB density is increased - and this while maintaining a high strength that is even higher than what is usually measured for nc Cu with a mean grain size of 30 nm [48] [49].

Generalized planar fault energy (GPF) curve is studied to explain the dominance deformation behavior in nano-crystals [4] [5] [37] [4] [3]. Instead of absolute value of the stacking fault energy, generalized planar fault energy involves both stable and unstable stacking fault energies for an intrinsic stacking fault, and also the twin migration energy. Generalized planar fault curve represents the energy cost of rigidly shifting two semi-infinite blocks of crystal on a (111) plane along a [112] direction, which is the energy gain as a function of shift-vector by rigidly shearing a perfect FCC lattice across a (111) plan. Such a curve is calculated by performing the rigid shift incrementally and, at each stage, relaxing the atomic configuration via molecular statics only in the direction normal to the (111) plane. Researchers found that in Al twinned nano crystals, the twin migration energy barriers are much lower than the partial dislocation energy barriers, therefore the grown-in twin enhances plastic deformation by means of twin boundary migration. In Cu, Ni twinned nano crystals, the twin migration energy barriers are not different from the partial dislocation energy barriers, as a result, the grown-in

twin migration is not the favored deformation, while partially dislocations travel transmit the crystals are more dominant. In Al defect-free nano crystals, full dislocation activities are also observed.

Schmid factor effect is observed in the activation of slip systems as well [5]. In Cu, Ni nano crystals where twin boundaries are introduced parallel to the (111) planes with the most optimal set of Schmid factors, extended dislocations are the dominant deformation behavior with few twin boundary migration. Instead in those where twin boundaries are introduced parallel to the (111) planes with the least optimal set of Schmid factors, partial dislocations are found to emit nonparallel to the twin boundaries, while twin boundaries create a barrier for the dislocations motion. In Al nano crystals where twin boundaries are introduced parallel to the (111) planes with the most optimal set of Schmid factors, twin boundary migration is the dominant deformation mechanism, while no partial or full dislocation are travelling through the crystals.

The twin boundary migration starts with atomic shuffling showed by the atomic displacement vectors and assisted by stress-assisted free volume migration, which are shown by the local hydrostatic pressure [86]. With the migration of free volume towards the original high compressive region, there is a corresponding redistribution of such compressive stress regions and the nucleation of a slip event resulting in the twin boundary migration.

Rate limit of MD (high stress in relative short time) is supposed to be part of the reason of the absence of full dislocations in tensile simulation. No trailing partial is able to emit because of the local structural relaxation in the grain boundary during and after the nucleation and absorption of the first partial, which is illustrated by the local hydrostatic pressure and maximum resolved shear stress distributions. If increase stress, the deformation mechanism changes to include

all types of slip: extended partials, full dislocations and twinning.

3-dimensional (3D) and 2-dimensional (2D) systems are compared [4]: in 3D Al defect free nano crystal, full dislocation activity is the dominate deformation mechanism, while in 2D Al columnar, plastic deformation is predominantly carried by deformation twinning, which is explained by the influence of the plane geometry. In 2D system, in order to create a partial, entire atomic columns have to be moved, because of no 3D atomic shuffling within the atomic columns, and therefore also no movement of free volume of the size typical of that of a grain boundary vacancy. The grain boundary columnar motion is clearly constrained by the imposed quasi-2D geometry, and the dislocation nucleates and propagates as a true 2D object. While 2D system allow only for slip planes whose normals are perpendicular to the columnar axis, on the other hand, the grain boundary stress inhomogeneities are localized in 3D system and then the emitted dislocations are strongly curved with a correspondingly different and reduced stress signature.

CHAPTER 3

Molecular Dynamics Computational Methods

The Molecular Dynamics (MD) method is developed to enable studies of the properties of material volumes containing millions to billions of atoms with effective interatomic potentials. The basic idea is to eliminate all electronic degrees of freedom, and assume that the electrons are glued to the nuclei. Thus, the interaction between two atoms is represented by a potential function that depends on the atomic configuration (i.e. relative displacement) and the local environment (i.e. electrons).

Based on the electronic structure database, or alternatively using experimental measurements of specific properties, approximate effective potentials can be constructed. According to classical Newtonian mechanics, the dynamic evolution of all atoms can be fully determined by numerical integration. In principle, once the positions and velocities of atoms in the finite ensemble within the simulation cell are known, all thermodynamic properties can be readily extracted.

The implementation and practice of MD simulations are more involved than the conceptual description alluded to here. A successful simulation depends on three major factors:

1. the computational implementation of the MD method;
2. the construction of accurate interatomic potentials; and
3. the analysis of massive data resulting from computer simulations.

In the following, we present the key concepts in the numerical implementation of MD methods.

3.1 The Principles of the Molecular Dynamics Method

The MD method is about the simultaneous motion and interaction of atoms or molecules. The following presentation outlines the basic equations and principles of the MD method. The dynamic evolution of the system is governed by classical Newtonian mechanics, where for each atom (i), the equation of motion is given by:

$$M_i \frac{d^2 R_i}{dt^2} = F_i = -\nabla_{R_i} \Phi \quad (3.1)$$

which is derived from the classical Hamiltonian of the system:

$$H = \sum \frac{M_i V_i^2}{2} + \Phi \quad (3.2)$$

An atom of mass M_i moves as a rigid particle at the velocity V_i in the effective potential of other particles, $\Phi(R_i)$. The atomic force F_i is obtained as the negative gradient of the effective potential, $F_i = -\nabla_{R_i} \Phi$. Solving these 2^{nd} order ordinary differential equations for all the atoms in a simulation cell may appear simplistic.

We can also regard those atoms as particles obeying Newton's 2nd law

$$-\frac{dV}{dx} = F = ma = m \frac{d^2 x}{dt^2} \quad (3.3)$$

where V is the potential energy; x is the position.

The question is how we can find out the motion of the atoms in a molecule, the $x(t)$?

We know that the force(x) can be calculated by

$$F(x) = m \frac{d^2 x}{dt^2} \quad (3.4)$$

Now we want to find the trajectory, $x(t)$ of that atom.

Assume that at time t , the atom is at position x_1 , with velocity $v_1 = \frac{dx_1}{dt}$; and acceleration $a_1 = \frac{d^2x_1}{dt^2} = m^{-1}F(x_1)$.

Approximately,

$$x_2 = x_1 + v_1\delta t \quad (3.5)$$

$$v_2 = v_1 + a_1\delta t = v_1 + m^{-1}F(x_1)\delta t = v_1 - m^{-1}\frac{dV}{dx}\Big|_{x_1}\delta t \quad (3.6)$$

In general, if we are given the initial position x_1 , and velocity v_1 of the atom, and the potential energy $V(x)$ which it feels, we can thus, step by step, compute its positions $x_1(t_1), x_2(t_2), x_3(t_3), \dots$ by

$$x_i = x_{i-1} + v_{i-1}\delta t \quad (3.7)$$

$$v_i = v_{i-1} + a_{i-1}\delta t = v_{i-1} + m^{-1}F(x_{i-1})\delta t = v_{i-1} - m^{-1}\frac{dV}{dx}\Big|_{x_{i-1}}\delta t \quad (3.8)$$

and thus approximately compute its trajectory $x(t)$. We call this process integrating the equations of motion to find the trajectory.

Molecular Statics is another widely used method to find the minimum energy configuration by moving atoms down along the potential surface. The idea is similar to quench the system quickly to reach the state of 0K temperature so that the system will reach a local energy minimization configuration. The algorithm of quench is:

$$\text{If } v \cdot f > 0; \quad \text{let } v = v$$

$$\text{If } v \cdot f < 0; \quad \text{let } v = 0$$

3.1.1 Advantages and Limitations

MD was first introduced by Alder and Wainwright in the late 1950s to study the interactions of hard spheres. In 1964, Rahman, first using a realistic potential for liquid Ar. In 1974, Rahman and Stillinger, first applied MD on a realistic system for liquid water. Today, MD simulations permit the study of complex, dynamics processes in systems such as proteins, DNA and crystallography. MD allows generation of information at the microscopic level such as atomic positions and velocities with capability of simulating up to 10^9 atoms.

The advantages of MD simulations include:

- Physically as meaningful as the potential U that is used.
- No approximation in treating the N-body problem.
- Unified study of all physical properties. (thermodynamic, structural, mechanical, dynamic and transport properties of a system.
- Several thousand particles are sufficient to simulate bulk matter.
- Direct link between potential model and physical properties.
- Complete control over input, initial and boundary conditions.
- Detailed atomic trajectories.

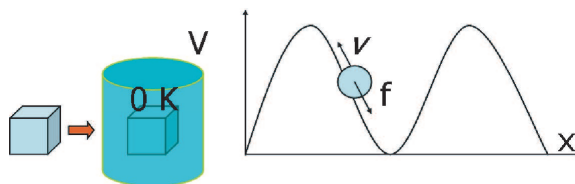


Figure 3.1: Molecular statics method: quench

MD also has its own limitations: (a) Need for sufficiently realistic interatomic potential functions U (b) Computational capabilities constraints.

Due to MD's limitations, researchers are developing multi-scale simulations (see chapter 2.2) that combine the MD and other methods to obtain large-scale computational capabilities for engineering nano-layered structures by computational design.

3.1.2 Algorithm of Molecular Dynamics

3.1.2.1 Flow Chart

The MD algorithm is realized by repeating the loop of Newton's motion equations, as shown in Figure 3.2.

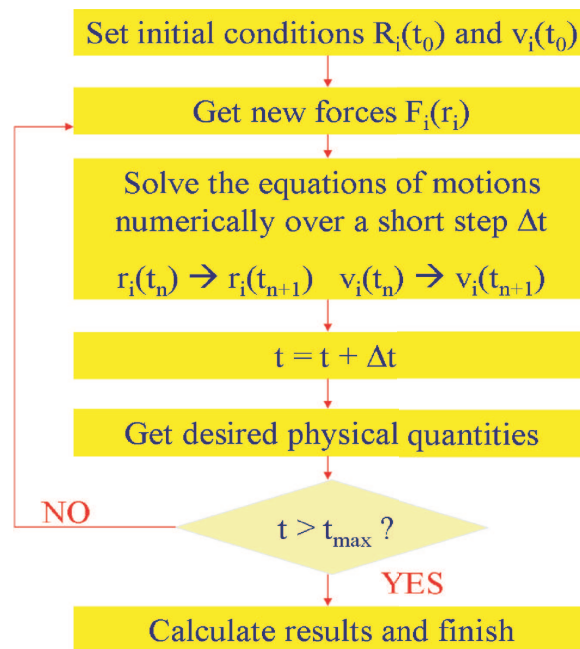
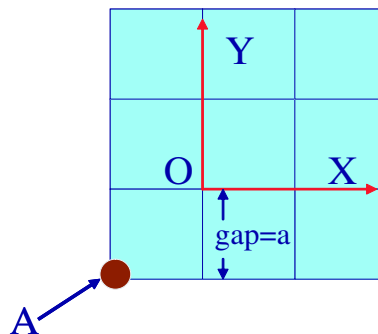


Figure 3.2: A flow chart of a typical MD algorithm.

3.1.2.2 Initial conditions: creating atomic configuration

To start, we need the initial atomic configuration as a basic input. The initial configuration could be a perfect lattice or a crystal with defects. Here is a simple algorithm to generate an FCC lattice by periodically repeating 2 base atoms in the space.

```
gap(k) = region(k) / initUcell(k)
DO nY= 1, initUcell(2)
c(2) = (nY-0.5)*gap(2) - regionH(2)
DO nX=1, initUcell(1)
c(1)= (nX-0.5)*gap(1) - regionH(1)
n = n +1
r(1, n) = c(1)
r(2, n) = c(2)
END DO
END DO
```



```
nY = 1, nX = 1
r(1,1) = c(1) = 0.5a - 1.5a = -1a
r(2,1) = c(2) = 0.5a - 1.5a = -1a
```

Figure 3.3: creating atomic configuration

3.1.2.3 Initial atom velocities

We also need to initialize the velocities for all the atoms. Here is one algorithm to assign velocities with fixed magnitudes and random directions.

```
(vMag fixed by temperature)
! Random directions
Ang = 2 * pi * RandR(randSeed)
rv(1,n) = vMag * cos (Ang)
rv(2,n) = vMag * sin (Ang)
! Centerof Mass is stationary
vSum(1) = vSum (1) + rv (1,n)
vSum(2) = vSum (2) + rv(2,n)
vSum(k) = vSum(k) / nAtom
rv(k,n) = rv(k,n) - vSum(k)
```

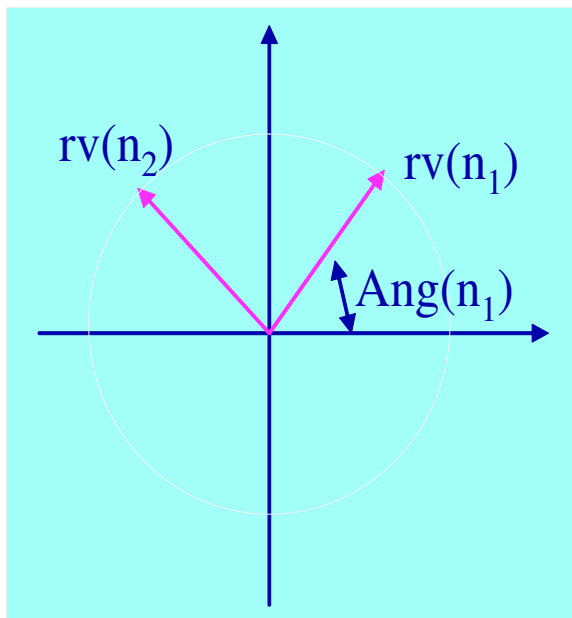


Figure 3.4: Initial velocities

3.1.2.4 Periodic Boundary Conditions

To get meaningful simulation results, we need to be very careful about the Boundary Conditions. Periodic Boundary Conditions (PBC) is one of the most widely used methods to allow us to simulate some bulk materials properties using only a few thousands of atoms. PBC means an atom which passes over the cell boundary comes back on the other side:

$$IF(r(k, n) \geq regionH(k)) \quad r(k, n) = r(k, n) - region(k)$$

$$IF(r(k, n) < regionH(k)) \quad r(k, n) = r(k, n) + region(k)$$

$$IF(dr(k) > regionH(k)) \quad dr(k) = dr(k) - region(k)$$

$$IF(dr(k) \leq regionH(k)) \quad dr(k, n) = dr(k) + region(k)$$

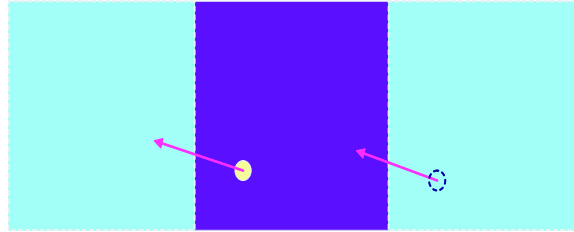


Figure 3.5: Periodic Boundary Conditions

3.1.2.5 Force Cutoff Distance

In the MD simulation, beyond r_{cutoff} distance, particles simply do not see each other. Force cutoff distance is an important parameter for the force calculation.

3.1.2.6 Neighbor List

As the number of the atoms increases every 10 times, the expense for calculating the neighbors will increase 100 times. Therefore it is necessary to have a neighbor list by keeping track of who are nearest, second nearest neighbors of each particle, so that we only need to update neighbor list after some steps.

3.1.2.7 Force calculation

We use the Lennard-Jones(LJ) (12-6) PAIR potential as an example to show the algorithm of force calculation:

$$U(r_{ij}) = 4\epsilon\left[\left(\frac{\sigma}{r_{ij}}\right)^{12} - \left(\frac{\sigma}{r_{ij}}\right)^6\right] \quad (3.9)$$

$$f_{ij} = -\nabla U(r_{ij}) = \frac{48\epsilon}{\sigma^2}\left[\left(\frac{\sigma}{r_{ij}}\right)^{14} - \frac{1}{2}\left(\frac{\sigma}{r_{ij}}\right)^8\right]r_{ij} \quad (3.10)$$

$$ma_i = F_i = \sum_{j=1, j \neq i}^N f_{ij} \quad (3.11)$$

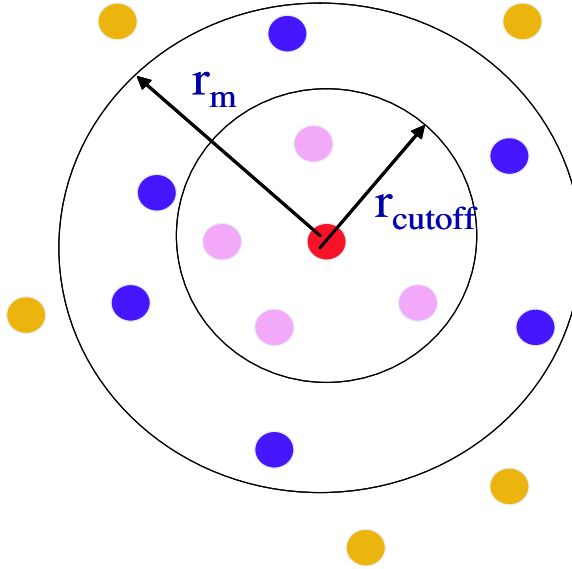


Figure 3.6: Cutoff distance in force calculation

3.1.2.8 Leapfrog step

A proper numerical integration scheme should be both numerically stable and computationally efficient. The numerical integration of the equations of motion is performed either by explicit or implicit methods. The simple Euler scheme is not appropriate for MD simulations because it lacks numerical stability. In the explicit Verlet's leap-frog method, the equation of particle motion is split into two first-order equations:

$$\frac{dR_i}{dt} = V_i, \quad \frac{dV_i}{dt} = F(R_i)/M_i \quad (3.12)$$

Based on the half-step leap-frog method, this set of equations is converted for small time increment δt to:

$$R_i(t + \delta t) = R_i(t) + \delta t V_i(t + \frac{1}{2}\delta t) \quad (3.13)$$

$$V_i(t + \frac{1}{2}\delta t) = V_i(t - \frac{1}{2}\delta t) + \delta t \frac{F_i}{M_i} \quad (3.14)$$

The Verlet algorithm is very popular in MD simulations because it is stable, memory-efficient, and allows for a reasonably large time-step. Another popular implicit integration method for MD simulations is the predictor-corrector scheme, in particular, Gear algorithm [26].

$$rv(k, n) = rv(k, n) + \delta T * ra(k, n) \quad (3.15)$$

$$r(k, n) = r(k, n) + \delta T * rv(k, n) \quad (3.16)$$

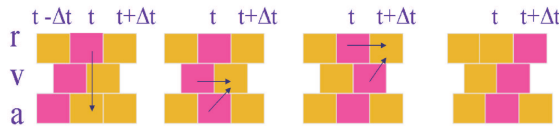


Figure 3.7: Illustration of the leapfrog algorithm

3.1.2.9 Examples of Properties Evaluation and Accumulation

The basic output information from MD simulation is the atom position and velocity, but we can extract a lot of different properties information from them. For example:

$$v = rv0.5r_a\delta T(\text{Leapfrogmethod}) \quad (3.17)$$

$$E_k = \frac{1}{2N_a} \sum_{i=1}^{N_a} v_i^2 \quad (3.18)$$

$$E_u = \frac{4}{N_a} \sum_{1 \leq i < j \leq N} (r_{ij}^{-12} - r_{ij}^{-6}) \quad (3.19)$$

$$T = \frac{1}{dN_a} \sum_i v_i^2 \quad (3.20)$$

$$PV = N_a T + \frac{1}{d} \left\langle \sum_{i=1}^N r_i \cdot F_i \right\rangle \quad (3.21)$$

3.1.2.10 Potential – Force Calculations

In MD simulations, interatomic potentials are the base of the force calculation, the accuracy of the potential determined the physical meaningfulness of the simulation result. A detailed discussion about potential will be in section 3.2.

Depending on the method of treating the electronic degrees of freedom of each atom, there are 3 main categories of potentials:

- Pair Potentials (the electronic degree of freedom is eliminated)
- Effective Medium Potentials (the electronic degrees of freedom are treated as a total energy function)
- Quantum-based Potentials - The Tight-Binding Method (the electronic wave functions can be built up as a linear combination of the atomic wave functions)

3.2 Interatomic Potentials

A proper MD method is a necessary condition for physically meaningful simulations. However, the method says nothing about how simulated atoms interact with each other. The latter aspect is solely determined by prescribed interatomic potentials, and is more crucial in obtaining physically meaningful results. In general, there is a compromise between the potential rigorousness and the computational efficiency. For high computational efficiency, pair potentials, such as [43] and Morse potentials [56] are used. With the increasing demand on accuracy and available computational power, many-body potentials such as the Finnis-Sinclair potential [24] and the Embedded Atom Method (EAM) [17, 59] have been commonly used. In the same category are effective medium and glue models [22]. Angular dependent potentials, which are also many-body, include the well-known Stillinger-Webber potential [83] and the Tersoff potential [84]. Potentials that have quantum mechanics basis, such as the generalized pseudopotential [54, 55], the bond order potential [70], and the inversion method [14, 99] have also been used for greater accuracy.

In general, interatomic potentials are empirical or semi-empirical, and thereby have fitting parameters. Simpler potentials, like the Lennard-Jones potential, have very few fitting parameters, which can be easily determined from crystal properties. On the other hand, these potentials suffer from non-transferability. Since these potentials are fitted to only a few perfect crystal properties, their applicability in studying defects is by default questionable. The more sophisticated potentials, like the EAM - particularly the force matching approach [21], use several or many defect properties to determine the EAM functions, in either analytical or tabular form. Materials properties, of either the perfect crystal or defected structures, are obtained from ab initio calculations and reliable ex-

periments. It is worth pointing out that these interatomic potentials apply for specific classes of materials. Strictly speaking, pair potentials are applicable to simulations of rare gas behavior. However, applications to simple metal systems can also provide qualitative guidance. The EAM type of potential has proven to be a good choice for simple metals. Applications to metals like aluminum, copper, silver, and iron (except its magnetic properties) have been very successful. The radial function form of the EAM is computationally advantageous. However, this advantage is accompanied by the inability to describe covalent systems, in which angular dependence dominates. In studying silicon, diamond carbon and other covalent systems, angular dependent potentials, particularly the Stillinger-Webber [83], the Tersoff [84], and the bond-order potentials [70] are among the leading candidates. A modification of the EAM has been proposed to include the angular dependence by [8], and applied to SiC by [36]; the modification by [67] is similar.

Potential energy is to determine the stable of a system. Quantum mechanics is most adequate when determine the stable of a system, but too complicated to be soluble.

Let us start from Time-dependent Schrödinger equation:

$$\widehat{H}\Psi = i\hbar \frac{\partial \Psi}{\partial t} \quad (3.22)$$

The probability that the particle will be found in the range x to $x + \delta x$, at a time t is $|\Psi(x, t)|^2 \delta x$, which is obtained by solving Equation 3.22.

Time-independent Schrödinger equation is

$$\widehat{H}\Psi = E\Psi \quad (3.23)$$

With the Born-Oppenheimer Approximation, the degrees of freedom can be unlinked.

$$\psi(\{\mathbf{R}_i, \mathbf{r}_n\}) = \psi_{el}(\{\mathbf{r}_n\}; \mathbf{R}_i) \psi_n(\{\mathbf{R}_i\}) \quad (3.24)$$

The idea comes from that nuclei and electrons have greatly disparate masses. Imagine the electrons to respond to an essentially static set of nuclear position. So in the Schrödinger equation for the electrons, the ionic coordinates only appear parametrically

Steps to solve the Schrödinger equation are:

1. To solve the electronic Schrödinger equation for a specific set of nuclear variables. The electronic equation is

$$\widehat{H}_{el}\Psi_{el} = E_{el}(r_1, r_2, \dots, r_N)\Psi_{el} \quad (3.25)$$

The nuclear coordinates are regarded as fixed and the wavefunction that is determined. gives the distribution of the electrons only.

2. To treat the nuclear dynamics by using the energy as an *effective potential* for the interaction of the nuclei.

$$(T_n + V_{nn} + E_{el})\psi(\{\mathbf{R}_i\}) = E_n\psi_n(\{\mathbf{R}_i\}) \quad (3.26)$$

Pair Potentials Pair potentials are constructed such that the electronic degree of freedom are eliminated, and the exact energy of the system, E_{exact} is replaced by an approximate energy function, E_{approx} . $E_{effective}$ Medium Potentials In these types of potentials, we treat the electronic degrees of freedom as a class of total energy functions known as effective medium functions Approximate embedding potentials divide the energy into two contributions, one from core-core repulsion that can be of a Coulomb or screened Coulomb type, while the second part represents the energy cost for embedding an ion in a uniform electron gas, of local density ρ Ab-initio calculations have shown that the electronic component

of the embedding energy shows a minimum that is dependent on the type of embedded ion. We will discuss now one example of analytical determination of embedded atom potentials. This is followed by the procedure for more accurate numerical determination of the Embedded Atom Method, or EAM for short [17] [59], and finally a different approach for the embedding function based on the Finnis-Sinclair procedure [24]. The basic idea of the tight-binding method is that the electronic wave function of the solid can be built up as a linear combination of the atomic wave functions centered on the atoms, following the solution procedure of the Schrodinger equation for the hydrogen molecule. The coefficients of the basis functions, i , are selected such that the total energy is a minimum. The eigenvalues of the resulting Hamiltonian matrix are the electronic contribution to the total energy. The method results in two main aspects: (1) the total energy of the system can be calculated directly without separation into pair potentials and embedding energy; and (2) it gives the form of the pair functionals and angular forces.

3.2.1 Connections Between Quantum and Approximate Potentials

The direct use of DFT methods to perform full quantum molecular-dynamics simulations on real materials is limited to a hundred or so atoms and a few picoseconds of simulation time. Thus, the next step of coarse-graining the problem is to remove the electronic degrees of freedom by imagining the atoms to be held together by some sort of glue or interatomic potential, thereby allowing large scale atomistic simulations for millions of atoms and nanoseconds of simulation time. Such simulations, employing approximate (or empirical) interatomic potentials, have been extremely useful in investigating generic phenomena in simple systems. Empirical potentials involve the fitting of parameters to a predetermined experimental or ab initio database which includes physical quantities such as the lattice

constant, the bulk modulus and elastic constants, the vacancy formation energy, the surface energy, etc. The goodness of the potential is determined by fitting to a small set of properties and then accurately predicting other properties not within the set used for fitting its parameters. However, at the same time, they may not provide the desired physical accuracy for many real complex materials of interest. For example, reliable interatomic potentials are not usually available for multi-element materials and for systems containing substitutional or 27 interstitial alloying impurities. Interatomic potentials used in MD simulations may generally be classified into three broad categories: (1) pair potentials; (2) effective medium potentials; and (3) quantum-based potentials. In pair potentials, the electronic DOF are totally eliminated, and are glued to nuclear DOF, thus atoms are represented by coordinates and momenta only. When electronic DOF are averaged out and included into an electronic density function that depends on the local environment of the atom, we have what is known as effective medium potentials. Implicit recognition of the electronic DOF is given through the embedding function. Further recognition of the electronic DOF is achieved through the introduction of reduced sets of coefficients based on quantum mechanics in quantum-based potentials. We give here examples of interatomic potentials belonging to the three main categories.

3.2.2 Pair Potentials

Pair potentials are constructed such that the electronic DOF are eliminated, and the exact energy of the system, E_{exact} is replaced by an approximate energy function, E_{approx} . Thus, we map the energy function of the system's nuclear, R_i , and electronic, r_i , coordinates, such that:

$$E_{(exact)}(R_i, r_i) \longrightarrow E_{approx}(R_i) \quad (3.27)$$

Two common examples of pair potentials are the Lennard-Jones [43] and the Morse [56] potentials:

3.2.2.1 The Lennard-Jones Potential [43]

The Lennard-Jones potential is sometimes used to model the interatomic interaction in solids, although it is best fit to the behavior of gases or fluids. The potential is given by:

$$V(R) = -\frac{A}{R^{12}} + \frac{B}{R^6} \quad (3.28)$$

where A and B are constants, determined by matching independent physical properties. For example, if the equilibrium lattice constant in Cu is 0.36 nm, and its shear modulus is 50 GPa, let's see how one can determine the two A and B.

$$E(R) = -\frac{A}{R^{12}} + \frac{B}{R^6}, F = -\nabla E = -\frac{12A}{R^{13}} + \frac{6B}{R^7} \quad (3.29)$$

We now take equilibrium distance to be the lattice constant = 3.610×10^{-10} m, where the force should be zero. This gives: $B = 2A/R_0^6$. We can assume that the approximate area per atom $\approx \pi R_0^2$, then:

$$\sigma = \frac{\Delta F}{\pi R_0^2} = E\epsilon = E \frac{\Delta R}{R} \Big|_{R_0} \Rightarrow E = \frac{1}{\pi R_0} \frac{\partial F}{\partial R} \quad (3.30)$$

However, $E = 2(2 + \nu)\mu = 1.34 \times 10^{-11}$ [pa] = $(\pi R_0) / \frac{156A}{R_0^{14}} - \frac{42B}{R_0^8}$

Now, solving for A and B, we obtain: $A = 1.38 \times 10^{-132}$ and $B = 1.17 \times 10^{-69}$.

3.2.2.2 The Morse Potential [56]

This potential, $E(R)$, is characterized by three parameters: ϵ_1, a_1 and R_0 , and is given by:

$$E(R) = \epsilon[e^{-2a(R-R_0)} - 2e^{-a(R-R_0)}] \quad (3.31)$$

Compared with the simpler Lennard-Jones potential, the repulsion term here is more realistic, but the attraction is less so. Furthermore, there is an extra parameter a , which can be used to fit a third property. We can fit, for example, the lattice constant R_0 , the bulk modulus B , and the cohesive energy E_{coh} , using the three conditions:

$$\left[\frac{dE}{dR}\right]_{R_0} = 0 \quad (3.32)$$

$$B = -V dP/dV = V \frac{\partial^2 E}{\partial V^2} \quad (3.33)$$

$$E_{coh} = [E]_{R_0} \quad (3.34)$$

The Morse potential may be written as:

$$E(R) = \zeta(\zeta - 2), \text{ and } \zeta = \exp[\rho(1 - R/R_0)] \quad (3.35)$$

where ϵ , ρ and R_0 are adjustable parameters that determine the shape of the potential. First, ϵ adjusts the depth of the potential (i.e the binding energy), R_0 adjusts the equilibrium interatomic separation, and ρ adjusts the range of the potential. Recently, an intermolecular potential for Bucky balls (C_{60} molecules), has been obtained, with an effective value of $\rho = 13.62$. The alkali metals have longer-ranged interactions, for example $\rho = 3.15$ has been suggested for sodium, while $\rho = 3.96$ for nickel. Take the case of two isolated atoms, separated by 0.4 nm at equilibrium and have a cohesive energy of (-5 eV). Then, $\epsilon = -5$ eV, $R_0=0.4$ nm.

3.2.3 Effective Medium Potentials

This class of potentials include the embedded-atom (EAM) type [17] [59] or the Finnis-Sinclair (FS) type [24] potentials for metals that do not exhibit directional bonding character, and the Stillinger-Weber (SW) type [83] [29] or the Tersoff type [84] potentials in covalent materials, where the potential depends on the

bond angle. In these types of potentials, we treat the electronic degrees of freedom as a class of total energy functionals known as effective medium and angular force schemes to incorporate environmental and angular dependencies. Thus, we map the exact potential to an approximate representation as:

$$E_{exact}(R_i, r_i) \rightarrow E_{approx}(R_i, r_i) \rightarrow E_{approx}[\rho(r_i), R_i] \quad (3.36)$$

Approximate embedding potentials divide the energy into two contributions, one from core-core repulsion that can be of a Coulomb or screened Coulomb type, while the second part represents the energy cost for embedding an ion in a uniform electron gas, of local density ρ . Ab initio calculations have shown that the electronic component of the embedding energy shows a minimum that is dependent on the type of embedded ion. We will discuss now one example of analytical determination of embedded atom potentials. This is followed by the procedure for more accurate numerical determination of the Embedded Atom Method, or EAM for short [17] [59], and finally a different approach for the embedding function based on the Finnis-Sinclair procedure.

In the EAM, all atoms are viewed as embedded in the host consisting of all other atoms, and the total energy is divided into an embedding energy, which is electron-density dependent, and pair contributions. Various functional forms are developed on the basis of known experimental or ab initio data:

$$E_{tot} = \sum_i F(\rho_i) + \frac{1}{2} \sum_{i,j} \phi(R_{ij}) \quad (3.37)$$

$$F(\rho) = E_{embed} \quad (3.38)$$

$$\rho_i = \sum_{j \neq i} f(R_{ij}) \quad (3.39)$$

$$\phi_{ij}(R) = Z_i(R)Z_j(R)/R \quad (3.40)$$

$\phi_{ij}(R)$ is the pair-interaction term, while $F(\rho)$ is the embedding energy term. The following represent popular examples of effective medium potentials.

3.2.3.1 The Johnson potential

Based on extensive experimental data and first principles calculations, the total energy was found to be a function of the interatomic separation in a simple form, known as the Universal Binding Energy Relation (UBER), and given by:

$$E_{tot}(R) = -E_{sub}[1 + \alpha(\frac{R}{R_0} - 1)]exp-\alpha(\frac{R}{R_0} - 1) \quad (3.41)$$

In this expression, E_{sub} is the absolute value of the sublimation energy at zero temperature and pressure, and $\alpha = (E_{sub}/9B\Omega)^{1/2}$. B is the bulk modulus of the material and Ω is the equilibrium volume per atom.

An analytical procedure was developed by , where the interatomic potential is obtained analytically. In this procedure, the embedding function is deduced as the difference between the total energy as given by the UBER and the total contributions of the pair part of the potential. For an fcc metal, the energy of a given atom (without double counting, since the fcc structure has 12 nearest neighbors) is E , given by:

$$E_i = F(\rho_i) + 6\phi(R_{nn}) \quad (3.42)$$

where R_{nn} is the equilibrium distance of the nearest neighbor, ϕ is the pair potential, F the embedding function, and ρ_i the total electron density at atom i . If we rely on our knowledge of the universal binding energy relationship, we can immediately deduce the embedding function as follows:

$$F[\rho(R)] = E_{tot}(R) - 6\phi(R) \quad (3.43)$$

Johnson assumed the following forms for $\rho(R)$ and $\phi(R)$:

$$\rho(r) = fe^{-\beta(\frac{r}{r_0}-1)} \quad (3.44)$$

$$\phi(r) = \phi_0e^{-\gamma(\frac{r}{r_0}-1)} \quad (3.45)$$

$$(3.46)$$

where f, β, ϕ_0 and γ are constants. With these forms, the embedding function can be analytically obtained, and is given by:

$$F(\rho) = -E_c \left(1 - \frac{\alpha}{\beta} \ln \frac{\rho}{\rho_0}\right) \left(\frac{\rho}{\rho_0}\right)^{\frac{\alpha}{\beta}} - 6\phi_0 \left(\frac{\rho}{\rho_0}\right)^{\frac{\gamma}{\beta}} \quad (3.47)$$

Force calculations in MD simulations must take into account the implicit dependence of the embedding function on interatomic distances. The force on the i^{th} atom due to the embedding function is given by

$$f_i = - \sum_{i \neq j} (F'(\rho_j) \rho'_j + F'(\rho_i) \rho'_i) \tilde{R}_{ji} \quad (3.48)$$

where \tilde{R}_{ji} is the unit vector connecting the i^{th} and j^{th} atoms.

3.2.3.2 The Embedded Atom Potential [17] [59]

The atomic densities are computed from the Hartree-Fock wave functions by

$$\rho^a(R) = n_s \rho_s(R) + n_d \rho_d(R) \quad (3.49)$$

where n_s and n_d are the number of outer s and d electrons and ρ_s and ρ_d are the densities associated with the s and d wave functions. The total number of s and d electrons, $n_s + n_d$ is fixed to be 10 for Ni, and 11 for Cu. For the pair-repulsion term, we assume a simple parameterized form for $Z(R)$:

$$Z(R) = Z_0(1 + \beta R^\nu e^{-\alpha R}) \quad (3.50)$$

Now we look at those parameters for Cu and Ni:

	Z_0	r	β	ν	n_s	Atomic configuration
Cu	11.0	1.7227	0.1609	2	1.000	$3d^{10}4s^1$
Ni	10.0	1.8633	0.8957	1	1.5166	$3d^84s^2$

When we do the forces calculation in the MD code, we are in fact using several numerical tables that contain the data for a certain element. The data includes $F(\rho) - \rho$, $\rho(R) - R$ and $Z(R) - R$ calculated from the equations and parameters above. For example, given atomic figuration of Cu lattice, in order to calculate the potential of a certain Cu atom, we have to know all the single contribution of $\rho(R)$ and $Z(R)$ between every other atoms and this certain atom by looking up the tables. Then sum all the $\rho(R)$ to get the total atomic density and look up the table of $F(\rho)$ to get the embedding energy. To get the pair interaction term, we just simply sum up all the $Z(R)$. The total potential of this atom is obtained by combining those two terms.

3.2.3.3 The Finnis-Sinclair Potential [24]

An embedding potential introduced by Finnis and Sinclair (1984) incorporates the band character of metallic cohesion. Finnis and Sinclair replaced the charge Z in tight-binding treatments with the sum of functions representing the valence electrons. The form of the potential is a balance between this attractive contribution and core repulsion. One form of the potential is given by:

$$E = E_n + E_e = \frac{1}{2} \sum_{ij} V_{ij}(R_{ij}) - \sum_i \sqrt{\rho_i} \quad (3.51)$$

The electron density for each atom is given by:

$$\rho_i = \sum_{i \neq j} \phi(R_{ij}) \quad (3.52)$$

where

$$\phi(R_{ij}) = \begin{cases} (R_{ij} - d)^2, & R_{ij} < d \\ 0, & R_{ij} > d \end{cases} \quad (3.53)$$

3.2.3.4 Potentials with Angular Dependence

The embedding-type potentials are applicable to metals that do not exhibit strong directional bonding character. However, in covalently-bonded solids, such as Si and SiC, the crystal structure is not closed packed, but is rather open. Certain angles between bonds designate the equilibrium nature of the open structure. Empirical interatomic potentials have been developed to reflect this fact, and the following two are among the most popular.

1. Stillinger-Weber angular potential [83]

In the Stillinger-Weber potential, the total energy is expanded in terms of two-body V_2 and three-body V_3 contributions.

$$E_{tot}(\{\mathbf{R}_i\}) = \frac{1}{2} \sum_{i,j} V_2(R_{ij}) + \frac{1}{3!} \sum_{i,j,k} V_3(\mathbf{R}_i, \mathbf{R}_j, \mathbf{R}_k) \quad (3.54)$$

The two-body (pair potential) contribution to the total energy is given by a function of scaled interatomic distances

$$V_2(R_{ij}) = \epsilon f_2\left(\frac{R_{ij}}{\sigma}\right) \quad (3.55)$$

while the three-body contribution is expressed as a function of three vectors connecting between triplets of three atoms as

$$V_3(\mathbf{R}_i, \mathbf{R}_j, \mathbf{R}_k) = \epsilon f_3\left(\frac{\mathbf{R}_i}{\sigma}, \frac{\mathbf{R}_j}{\sigma}, \frac{\mathbf{R}_k}{\sigma}\right) \quad (3.56)$$

$$f_2(R) = \begin{cases} A(BR^{-p} - R - q)e^{[(r-a)^{-1}]} & \text{if } r < a \\ 0 & \text{otherwise} \end{cases} \quad (3.57)$$

$$f_3(\mathbf{R}_i, \mathbf{R}_j, \mathbf{R}_k) = h(R_{ij}, R_{ik}, \theta_{jik}) + h(R_{ji}, R_{jk}, \theta_{ijk}) + h(R_{ki}, R_{kj}, \theta_{ikj}) \quad (3.58)$$

$$h(R_{ij}, R_{ik}, \theta_{jik}) = \lambda e^{[\gamma(R_{ij}-a)^{-1} + \gamma(R_{ik}-a)^{-1}]} \left(\cos\theta_{jik} + \frac{1}{3}\right)^2 \quad (3.59)$$

The key ingredient in this formulation is the angular function h , which is selected to be a function of the angle θ_{ijk} between the vectors R_{ji} and R_{jk} . $\lambda, a, \gamma, A, B, \text{ and } q$ are fitting constants. It is noted that the angular term is minimized for $\theta \approx 109.47$ degree, corresponding to the tetrahedral angles that characterize the sp^3 bonds of covalent materials.

2. Tersoff cluster functionals (1988) [84]

The Stelling-Weber potential does not have explicit functional dependence on the embedding environment for participating atoms. Tersoff (1986) was the first to develop Si potentials that account for environmental dependence. The total energy in his potential takes the form:

$$E_{tot} = \frac{1}{2} \sum_{ij} [V^r(R_{ij}) + b_{ij}V^a(R_{ij})] \quad (3.60)$$

where the repulsive potential is given by

$$V^r(R_{ij}) = Ae^{-\lambda_1 R_{ij}} \quad (3.61)$$

And the attractive potential by

$$V^a(R_{ij}) = Be^{-\lambda_2 R_{ij}} \quad (3.62)$$

The environmental and angular dependence enter the potential through the function b_{ij}

$$b_{ij} = (1 + \beta^n \xi_{ij}^n)^{-1/2n} \quad (3.63)$$

where the function ξ_{ij} is given by

$$\xi_{ij} = \sum_{k \neq ij} f_c(R_{ik})g(\theta_{ijk}) \quad (3.64)$$

and $f_c(R)$ is a cutoff function that smoothly decreases from $1 \rightarrow 0$ as $R \rightarrow R_c$

The function $g(\theta_{ijk})$ contains the angular dependence, and takes the form

$$g(\theta) = 1 + \frac{c^2}{d^2} - \frac{c^2}{d^2 + (h - \cos\theta)^2} \quad (3.65)$$

3.2.4 Quantum-based Potentials - The Tight-Binding Method

There is a growing need to develop more accurate interatomic potentials, derived from quantum mechanics, that can be applied to large-scale atomistic simulations. This is especially so for directionally-bonded systems, such as transition metals, and for chemically or structurally complex systems, such as intermetallic compounds and alloys. The Tight-Binding [16] [50] and the self-consistent-charge density functional Tight-Binding Molecular Dynamics (TBMD) approach is becoming widespread in the atomistic simulation community, because it allows one to evaluate both ionic and electronic properties [25]. The success of TBMD stands on a good balance between the accuracy of the physical representation of the atomic interactions and the resulting computational cost. TBMD implements an empirical parameterization of the bonding interactions based on the expansion of the electronic wave functions on a very simple basis set. Recently, novel analytic bond-order potentials have been derived for atomistic simulations by coarse-graining the electronic structure within the orthogonal two-center tight-binding representation [70] [68] [69]. Quantumbased interatomic potentials for transition metals that contain explicit angular-force contributions have been developed from first-principles, DFT-based generalized pseudopotential theory [54] [53] [52].

The basic idea of the tight-binding method is that the electronic wave function of the solid can be built up as a linear combination of the atomic wave functions centered on the atoms, following the solution procedure of the

Schrodinger equation for the hydrogen molecule. The coefficients of the basis functions, $\alpha_{i\beta}$, are selected such that the total energy is a minimum. The eigenvalues of the resulting Hamiltonian matrix are the electronic contribution to the total energy. The method results in two main aspects: (1) the total energy of the system can be calculated directly without separation into pair potentials and embedding energy; and (2) it gives the form of the pair functionals and angular forces.

The electronic degrees of freedom are thus incorporated by the mapping

$$E_{exact}(\{\mathbf{R}_i, \mathbf{r}_n\}) \longrightarrow E_{approx}(\{\mathbf{R}_i, \alpha_i\}) \quad (3.66)$$

where $\{\alpha_i\}$ are expansion coefficients that characterize the electronic wave function. The solid is assumed to be formed by bringing its atoms into close proximity such that the atomic energy levels of outer valence electrons are distributed as a result of the overlap between the wave functions of adjacent atoms. We postulate a wave function for the total solid of the form

$$\psi_r = \sum_{i=1}^N \sum_{\alpha=1}^n a_{i\alpha} \phi_{\alpha}(r - R_i) \quad (3.67)$$

or, written in a more compact form

$$|\psi\rangle = \sum_{i=1}^N \sum_{\alpha=1}^n a_{i\alpha} |i, \alpha\rangle \quad (3.68)$$

The outer sum runs over the number of atoms, N , in the solid, while the inner sum runs over the number of orbitals per site. The representation of the wave function, $|i, \alpha\rangle = \phi_{\alpha}(r - R_i)$ is for the α orbital on site i . For the case of Si, for example, we make our expansion for the $3s$ and $3p$ electrons only, with no contributions from inner shell electrons. The procedure attempts

to find the minimal set of wave functions, with no attempt for completeness. Now we write the energy functional, Π , as a function of the wave function, ψ , or, as a function of the unknown expansion coefficients

$$\Pi(\{a_{i\alpha}\}) = \langle \psi | \hat{H} | \psi \rangle - E \langle \psi | \psi \rangle \quad (3.69)$$

$$(3.70)$$

Substituting now for the total wave function (Equations 3.67 and 3.68). We have

$$\Pi(\{a_{i\alpha}\}) = \sum_{i,j=1}^N \sum_{\alpha,\beta=1}^n (h_{ij}^{\alpha\beta} - ES_{ij}^{\alpha\beta}) a_{i\alpha}^* a_{j\beta} \quad (3.71)$$

Where the matrices, $h_{ij}^{\alpha\beta}$, and $S_{ij}^{\alpha\beta}$ are given by

$$h_{ij}^{\alpha\beta} = \langle i, \alpha | \hat{H} | j, \beta \rangle = \int_{\Omega} \phi_{\alpha}^*(r - R_i) \hat{H} \phi_{\beta}(r - R_j) d^3r \quad (3.72)$$

and

$$S_{ij}^{\alpha\beta} = \langle i, \alpha | j, \beta \rangle = \int_{\Omega} \phi_{\alpha}^*(r - R_i) \phi_{\beta}(r - R_j) d^3r \quad (3.73)$$

The matrix $S_{ij}^{\alpha\beta}$ represents the degree of overlap between wave functions of adjacent sites, and is hence called the overlap matrix. If the wave function basis set is selected to be orthogonal, then $S_{ij}^{\alpha\beta} = \delta_{ij} \delta_{\alpha\beta}$. Once the Hamiltonian matrix is formed (Equation 3.71), the unknown coefficients $a_{i\alpha}$ can be obtained by minimization, thus

$$\partial \Pi / \partial a_{i\alpha}^* = 0 \quad (3.74)$$

$$\sum_{p'} (H_{pp'} - E \delta_{pp'}) a_p = 0 \quad (3.75)$$

where the super index p' runs from 1 to nN . Solution of the set of nN Equations 3.75 results in a set of energy eigen values, $E_k \equiv E_{i\alpha}$, and a set of coefficients $a_p \equiv a_i$ that determine the total wave function itself.

Evaluation of the matrix elements is usually done by the so-called two-center approximation, where contributions to the $h_{ij}^{\alpha\beta}$ arise only from the potential of two neighboring atoms i and j , $V_{atom}(r - R_i)$ and $V_{atom}(r - R_j)$, respectively. Each matrix element depends on the separation distance and orientation vector between two neighboring atoms. Since p-orbitals are spherically symmetric, and p-orbitals have single lobes of the wave functions, oriented along $x(p_x), y(p_y)$ or $z(p_z)$, then various symmetries should arise in coupling factors, V , within the matrix elements. For example, if the azimuthal rotational symmetry direction of individual atoms is aligned with the bond direction, we would have the so-called σ -bond. This may arise because of coupling between two s-orbitals, two p-orbitals, etc., and we would have factors like $V_{ss\sigma}, V_{pp\sigma}$ etc. On the other hand, π -bonds are denoted for couplings of orbitals such that the azimuthal symmetry directions of individual atoms are normal to bond direction. Such is the case when we consider two p_z -orbitals of two neighboring atoms connected along the x-axis.

Solution of the eigenvalue problem stated above results in a spectrum of energies that covers a wide span, and can be best represented as a histogram of delta functions, known as the electronic Density Of States (DOS), which takes the form

$$\rho(E) = \sum_i \delta(E - E_i) \quad (3.76)$$

Thus, the electronic contribution to the total energy is obtained by summing up all eigen values of E , or rather by performing the integral:

$$E_{el} = 2 \int_{-\infty}^{e_F} E \rho(E) dE \quad (3.77)$$

the factor of two accounts for up-down electron spin occupancy of each state. The total energy can then be constructed by adding an effective pair

potential for the interaction between neighboring nuclei.

$$E_{total}(\{\mathbf{R}_i\}) = \frac{1}{2} \sum_{ij} V_{eff}(R_{ij}) + 2 \int_{-\infty}^{\epsilon_F} E \rho(E) dE \quad (3.78)$$

Typical calculations proceed as follows. First, a computational cell is constructed with its set of nuclear coordinates, R_i . Once we have these coordinates, we can determine the elements of the interaction matrix, $h_{ij}^{\alpha\beta}$, which describe the coupling between the α^{th} orbital on site i with the β^{th} orbital on site j . The overlap matrix, $S_{ij}^{\alpha\beta}$, can be similarly determined. The full Hamiltonian is thus known, and we can proceed to find the energy eigen values, and finally determine the degree of state, $\rho(E)$.

3.3 Boundary Conditions

Similar to the numerical integration scheme, proper use of boundary conditions is crucial to obtaining a physically meaningful MD simulation. The boundary of a simulation cell is usually within close proximity to each simulated atom, because of limited computational power. Simulations for one billion atoms represent the upper limit of computation today with simple interatomic potentials (e.g. [43]). Total simulation times are typically less than one nano-second as a result of short integration time steps in the femto-second range. The boundary of a simulation cell may not be a real physical interface, rather it is merely the interface of the simulation cell and its surroundings. Various boundary conditions are used in mechanics simulations. Since dislocations dominate the linking of nano- and micro- mechanics, the following presentation of boundary conditions focuses on those boundary conditions relevant to the long-range strain fields of dislocations. These boundary conditions include: the rigid boundary condition [41], periodic boundary condition [40], direct linking of atomistic and continuum regions [65], and flexible (Green's function) boundary condition [80, 93, 33, 72].

3.3.1 The Rigid Boundary Condition

The rigid boundary condition is probably the simplest. According to this condition, boundary atoms are fixed during molecular dynamics simulations. For simple dislocation configurations, the initial strain field, say of an infinitely long straight dislocation, is imposed on all atoms in the simulation cell. During subsequent simulations, boundary atoms are not allowed to relax. This rigidity of the boundary condition naturally leads to inaccuracy in the simulation results.

3.3.2 Periodic Boundary Conditions

The inaccuracy also exists in the application of the periodic boundary condition. According to this condition, the simulation cell is repeated periodically to fill the entire space. When one dislocation is included in the simulation cell, infinite number of its images are included in the entire space because of the infinite repetition of the simulation cell. Modifications have been made to include dipoles in a simulation cell, and to subtract the image effects. However, it is difficult to extend such modifications to general dislocation configurations, which are more complex.

3.3.3 Flexible Boundary Conditions – Greens Function

In contrast to the two approximate boundary conditions, the direct linking and flexible boundary conditions can be rigorous. The direct linking of atomistic and continuum region [65] aims at a seamless bridging of two different scales. This idea has been extended to include the direct linking of atomistic and electronic structure regions [1]. Once numerically robust and efficient, the direct linking scheme should be the most reliable and desirable boundary condition. At present, the other rigorous scheme - flexible boundary condition - is more com-

monly used in dislocation simulations. This scheme has gone through the implementations in two and three dimensions. In the 1970's, the two-dimensional version of this boundary condition was implemented [93, 80, 33], allowing the simulation of a single straight dislocation. In these simulations, periodic boundary conditions are applied along the dislocation line. On the plane normal to the dislocation line, the simulation cell is divided into three regions. The innermost region is MD region, in which atoms follow Newtonian dynamics according to the MD method outlined earlier. The intermediate region is the flexible region (or Green's function region), in which the force on each atom is calculated, and then used to generate displacements of all atoms in the simulation cell using the Greens' function of displacement. Since periodic boundary condition is applied along the dislocation line, line forces are calculated in the flexible region, making the displacement two-dimensional. The outermost region contains atoms that serve as background for force calculations in the flexible region. As a result of renewed interest in dislocation dynamics, flexible boundary conditions have been extended to three dimensions, and are often referred to as the Green's function boundary conditions [72]. Flexible or Green's function boundary conditions have clear advantages in allowing for full relaxation of one or a few dislocations in a simulation cell, without suffering from the artifacts of image dislocations. However, Green's function calculations are time-consuming, limiting applications of the Green's function boundary condition. Recently, a tabulation and interpolation scheme [27] has been developed, improving the computational efficiency by two orders of magnitude, yet maintaining the accuracy of linear elasticity. With this improvement, the Green's function boundary conditions work well for static simulations of dislocations. However, they are not applicable to truly dynamic simulations. During dislocation motion, elastic waves are emitted, and when they interact with the simulation cell boundaries or borders, they are reflected and can

lead to interference or even resonance in the simulation cell. Approximate approaches [42, 11] have been proposed to damp the waves at the boundary, but a fully satisfactory solution is still not available.

Elastic Green's functions, which describe the displacement response of a linear elastic solid to a point force, are fundamental ingredients in many methods developed for understanding the mechanics of materials. A description of the internal, or self stress field of materials containing defects is critically dependent on accurate knowledge of elastic Green's functions. Interaction forces between defects and the elastic energy stored around them can be obtained once Green's functions are determined. More recently, Molecular Dynamics (MD) computer simulations of defect interactions have utilized Green's functions to connect atomistic simulation regions to the elastic continuum, e.g. [72]. Computer simulations of defect interactions by Kinetic Monte Carlo (KMC), e.g. [62], or by DD, require Green's functions as essential elements. Unfortunately, however, analytical solutions of Green's functions are not available, with the exception of a few cases. Moreover, numerical methods for 3-D Green's functions in finite spaces of general elastic anisotropy are also very limited [7]. Once Green's tensor functions are determined, the elastic field of a dislocation loop can be constructed by numerical integration.

Two-dimensional version of flexible boundary condition is shown in figure 3.8. Periodic boundary conditions are applied along the dislocation line. On the plane normal to the dislocation line, the simulation cell is divided into three regions. The innermost region is MD region; the intermediate region is the flexible region (or Greens function region), in which the force on each atom is calculated, and then used to generate displacements of all atoms in the simulation cell using the

Greens function of displacement. The outermost region contains atoms that serve as background for force calculations in the flexible region. Three dimensions.

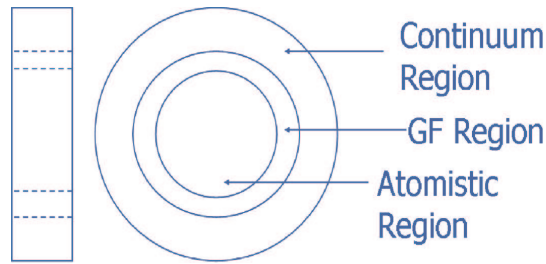


Figure 3.8: Green function boundary condition

3.4 Stress and Temperature Control

In addition to the numerical integration and boundary condition issues, successful MD simulations rely on the proper control of thermodynamic variables: stress and temperature. When the internal stress, as derived from interatomic interactions, is not balanced by the external stress, the simulation cell deforms accordingly. At small stress levels, this response is consistent with linear elasticity. Under general stress conditions, the formulation of [66] provides a mechanism to track the deformation. In this formulation, the three vectors describing the shape of simulation cell are equated to position vectors of three imaginary atoms. The driving force of the imaginary atoms is the imbalance of internal and external stresses, and the motions of those atoms are governed by Newton's equations of motion. This formulation works well when an equilibrated stress state is sought. However, large fluctuations in the deformation are unavoidable according to the Parrinello-Rahman method; the lattice constant may fluctuate by about 0.5% around its equilibrium value. This large fluctuation may introduce artifacts in the simulation of kinetic process, and caution should be exercised. The other thermodynamic variable, temperature, is controlled through the kinetic energy

or velocities of all atoms. Using frictional forces to add or subtract heat, the Nose-Hoover method [64, 34] provides a mechanism of controlling the temperature of a simulation cell. When the temperature is uniform in space and constant in time, little difficulty exists. When the temperature changes, however, the strength of the frictional force dictates the transition time. A fast transition is usually necessary because of the short time reachable in MD simulations. However, such a transition is generally too fast compared to realistic processes. This transition problem exists in other temperature control mechanisms, such as velocity scaling or introduction of random forces.

CHAPTER 4

Results for Dislocation Transmission in Cu/Ni Nano-Layers

4.1 Numerical Models

We use here the embedded atom method (EAM) [59] to represent the empirical potentials of Cu, Ni, and Cu-Ni, because it contains the two-species cross interaction format by fitting to the properties of a disordered Ni-Cu system. An atom is viewed as embedded in a host consisting of all other atoms, and the total energy is divided into an embedding energy, which is electron-density dependent, and pair contributions. In this work, parallel large-scale MD simulations are carried out on the Beowulf cluster ISIS, with up to 20 nodes. Three kinds of cells with an $\frac{a}{2} \langle 110 \rangle$ edge dislocation in each were simulated: pure Cu, pure Ni and Cu-Ni multi-layer cells. The x , y and z axes of the simulation cells were $[110]$, $[\bar{1}\bar{1}\bar{1}]$, and $[1\bar{1}2]$. The cells had 3 units along the z axis, 7 nm wide along the y axis, with thickness (wavelength λ) of the multi-layer structures along x axis, which was designed to have different values between 5 nm and 80 nm, covering the range of nano-layer structures with the highest strength. Periodic boundary conditions were applied in the z direction and free surface boundary conditions were applied in the other two directions. An infinite edge dislocation with a Burgers vector of $\frac{a}{2} \langle 110 \rangle$ was introduced by inserting two $\langle 220 \rangle$ half atom layers in the middle of the cells and displacing all the atoms from their perfect lattice positions according to their anisotropic elastic displacement field. Atoms in the cells were then allowed to relax using EAM potential interactions. The relaxed

structure of the dislocation core was studied and visualized by two methods: the Centro-symmetry parameter and the coordination number. For simulations of the dislocation core, a constant shear stress was applied on the relaxed cells in the range of 400 to 1200 MPa on the $(1\bar{1}\bar{1})$ plane along the $[110]$ direction. The motion of the dislocation core was studied during MD simulations by recording the position of the core at different time intervals.

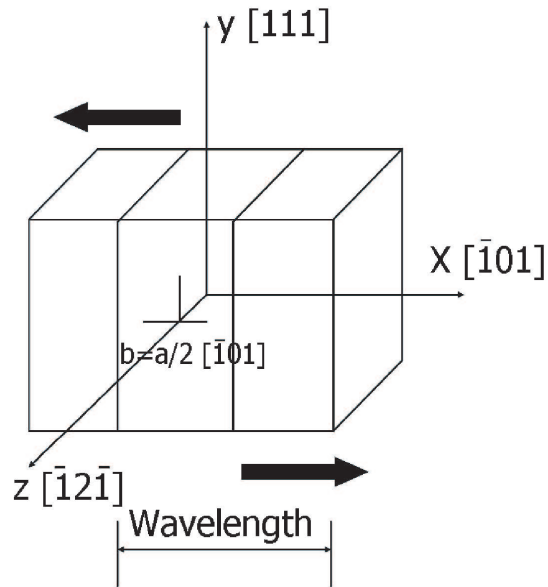


Figure 4.1: Schematic of the simulation model for Cu/Ni nano-layer structure.

The parallel code is PARADYN written by Steve Plimpton at Sandia National Laboratory [82]. The PARADYN code is a parallel implementation of the DYNAMO program, which is written by Stephen Foiles and Murray Daw [59]. PARADYN uses EAM potential [59] to calculate interatomic forces. and can perform both the static minimization and molecular dynamics simulations.

4.2 Dislocation Core Dissociation

A perfect dislocation in an FCC lattice could dissociate into two Shockley partials as shown in Figure 4.2.

since

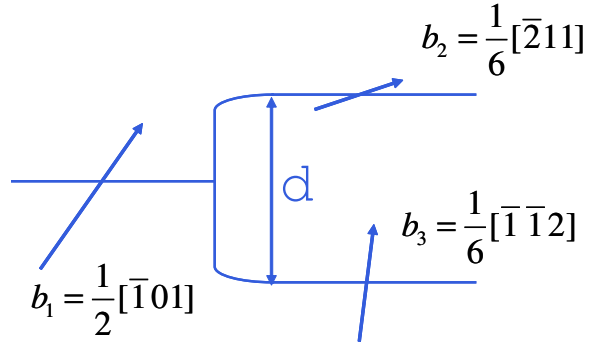


Figure 4.2: Dissociation of a perfect dislocation into two Shockley partials

$$b_1 = b_2 + b_3 \quad (4.1)$$

and

$$b_1^2 > b_2^2 + b_3^2 \quad (4.2)$$

then, the energy of the system decreases because of the dissociation. Because of the reduction in dislocation energy, the dissociation into Schockley partials is observed in FCC crystals. As the distance d between the two partials increases, the stacking fault energy increases, while at the same time, the interaction energy between these two partials decreases. Therefore there exists an equilibrium distance, given by

$$d = \frac{\mu b_1^2}{8\pi\gamma_{SF}} \left(\frac{2-\nu}{1-\nu} \right) \quad (4.3)$$

where γ_{SF} is the stacking fault energy density. Based on experimental data for the stacking fault energies, we have [60]:

$$\gamma_{SF,Cu} = 45mJ/m^2 \quad (4.4)$$

$$\gamma_{SF,Ni} = 125mJ/m^2 \quad (4.5)$$

Hence, the width between the two partials for Ni and Cu is estimated as

$$d_{Cu} = 1.7nm \quad (4.6)$$

$$d_{Ni} = 1nm \quad (4.7)$$

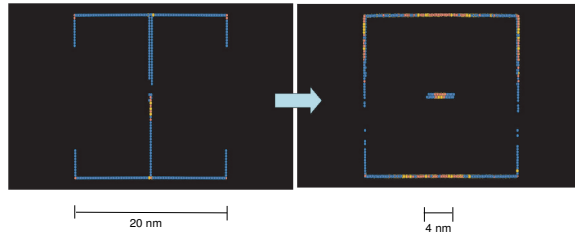


Figure 4.3: Dissociation of the dislocation core into two partials in Copper

Planar core spreading or splitting into shockley partials on the $(1\bar{1}\bar{1})$ plane has been observed in the present simulations. The core width of dissociated dislocations in different layer structures is shown in Figure 4.4 as a function of the wavelength for Ni and in Figure 4.5 for Cu. When the wavelength of the multilayer becomes larger than $\approx 40 - 80$ nm, the dislocation width becomes independent of the wavelength and close to its bulk value. Image forces caused by free surfaces tend to pull the two partial dislocations apart. The smaller the cell size is, the stronger the image force effect, and hence the wider the core. In small size cells, cores spread on the surfaces, and no core width could be measured. When the wavelength is small, Cu-Ni interfaces show strong influence on the width of the core. Interfaces are found to repel partials in Cu and attract them in Ni. The core width is observed to be restricted within Cu layers, and is

found to be proportional to the wavelength. The effect of the interfaces on the dislocation core structure becomes unimportant when wavelength is larger than 40 nm.

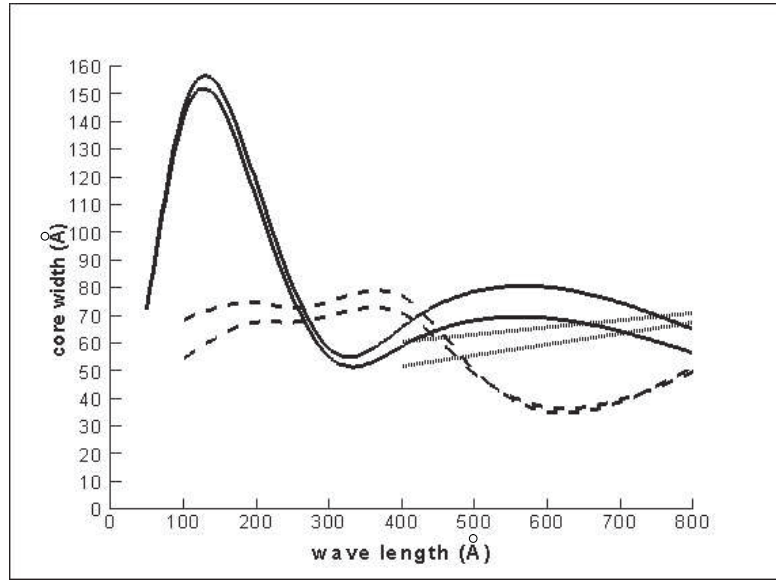


Figure 4.4: The core width of dissociated dislocations in different layer structures as a function of the wavelength for Ni. (a) Solid line: in 5 layers of Ni/Cu/Ni/Cu/Ni, (b) dot line: in 3 layers of Cu/Ni/Cu, (c) dash line: in single Ni crystal.

4.3 Motion of Dislocations in Nano-layers

One representative example of core motion under an applied shear stress is shown in Figure 4.6. The position of the two partials and their velocities were determined from MD simulations. It is shown in the figure that the two partials move towards the interface at different velocities, and that their velocities are not constant and depend on the applied stress. Cu-Ni interfaces act as a strong barriers for continued motion of the partials in Cu, which can be seen from the decrease in the displacement gradients of the partials when they approach the interface. They get stuck at the interface for period of time, depending on the stress level, before they penetrate the interface. On the contrary, interfaces may also accelerate the

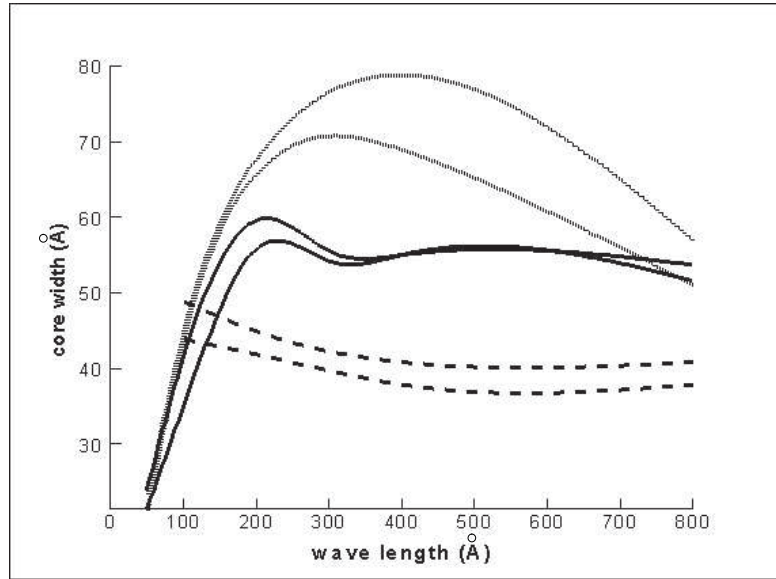


Figure 4.5: The core width of dissociated dislocations in different layer structures as a function of the wavelength for Cu. (a) Solid line: in 5 layers of Cu/Ni/Cu/Ni/Cu, (b) dot line: in 3 layers of Ni/Cu/Ni, (c) dash line: in single Cu crystal.

partials, when they move towards the interface from a Ni layer, which is indicated by the increase in the displacement gradient in Figure 4.6. When the shear stress is below its critical value, the two partials do not penetrate the interface.

Several snap-shots of a movie are shown in Figure 4.7 showing the motion of an edge dislocation in 3 layers of Ni/Cu/Ni and moving from the middle towards the surface. Atoms in perfect positions are not shown, and only atoms within the dislocation core or at the interface are shown for clarity. White atoms represent Cu and purple atoms represent Ni. The blue and red atoms mark atoms that are not in a Centro-symmetric position (see section 5.1).

We can see that when the applied shear stress is under 800 MPa, the dislocation can not attain enough energy to penetrate the interface from Cu (softer layer) to Ni (harder layer). It gets stuck there and moves back and forth. When the shear stress is increased to 1200 MPa, the dislocation can eventually accumulate enough energy and penetrate the interface from Cu to Ni.

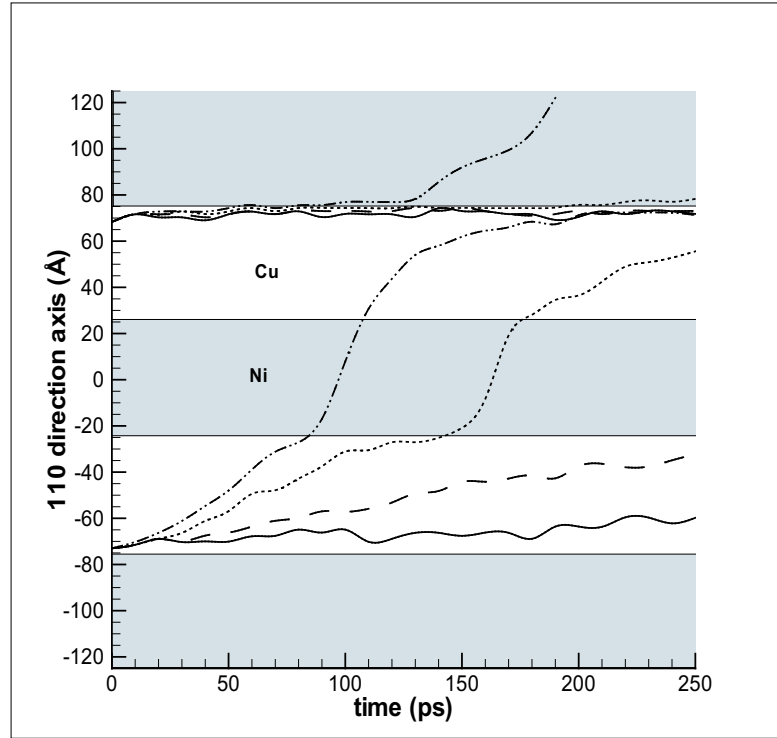


Figure 4.6: Core motion under shear stress in 5 layers Ni-Cu-Ni-Cu-Ni structure with wavelength of 10 nm. The upper curves are for the position of the leading dislocation, and the bottom curves are for the trailing partials. (a) Solid line: under 200 MPa, (b) dash line: under 400 MPa, (c) dot line: under 800 Mpa, (d) dash dot dot line: under 1200 MPa.

4.4 Discussions

In the Cu-Ni nano-layer system, the $\frac{a}{2}[110]$ edge dislocation core width is found to depend on the wavelength of the nano-layered structure, and is influenced by the applied stress and image forces resulting from the elastic modulus mismatch between adjacent layers. Interfaces act as barriers to dislocation transmission, which accelerate or decelerate the motion of its partials, depending on whether the dislocation is originally in a Ni or a Cu layer, respectively. The results show that several factors influence the core structure and thus affect slip confinement in nano-layers, and hence the maximum value of the yield strength. The results

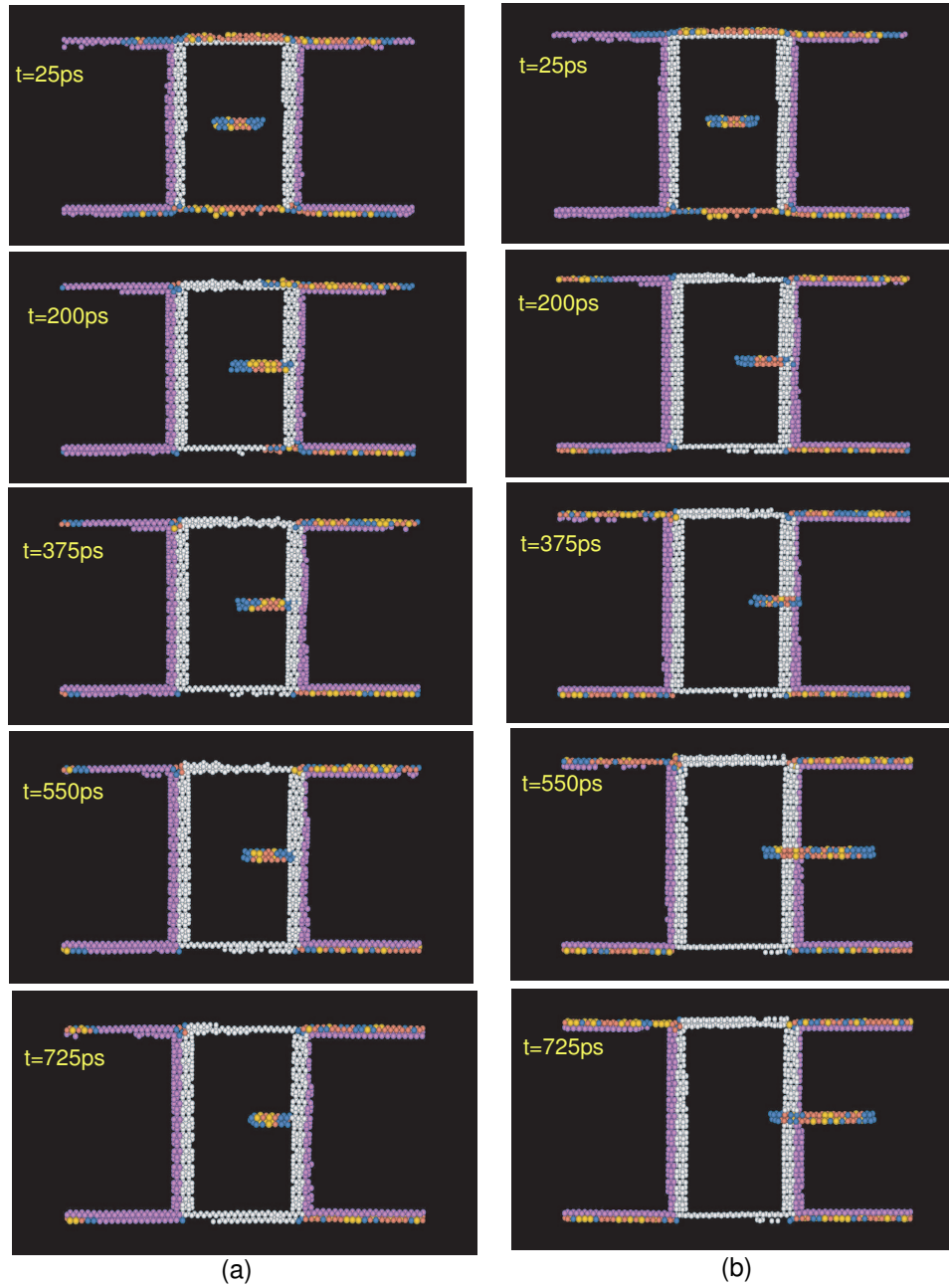


Figure 4.7: Core motion under shear stress in 3 layers Ni-Cu-Ni structure with wavelength of 10 nm. (a) under shear stress of 800 MPa. (b) under shear stress of 1200 MPa.

suggest that the maximum attainable strength of a nano-layered system is dictated by the interaction of partials with interfaces.

The two Shockley partials move towards the interface at different velocities. The velocities are not constant and depend on the applied stress resulting in jerky motion.

The strength of nano-layered materials is dictated by dislocation confinement at interfaces, when an external stress is applied. In materials composed of nano-layered duplex structures, several factors influence the maximum value of the externally-applied stress before dislocations can move across the interface, and thus slip confinement is lost. The strengthening effect is a result of elastic modulus mismatch across the interface (the Koehler barrier), lattice resistance mismatch influencing the core structure (the gamma surface effect), and any coherency strains.

However, although we can analyze the strength mechanism, the simulation result is only qualitative because the parameters of the EAM potential are not calibrated with the experimental values of the stacking fault energies for Ni and Cu.

CHAPTER 5

Deformation of Nano-twinned Copper

5.1 Atom Identification Methodology

MD simulations provide detailed information on the positions and velocities of all atoms in the simulation box. However, the most interesting information for us for the purpose of understanding the deformation mechanism is the location and density of atoms in imperfect positions (e.g. in dislocation cores, vacancies and in interstitial sites), and how such atoms interact with interfaces. One way to do this is to identify defects as atoms with higher energy than the average thermal value. However, identification of atoms in imperfect positions by their energy is not accurate, and usually contains significant noise. For this reason, most researchers rely on geometric information to characterize defects. One popular method is the so-called Centro-symmetry method. The algorithm for this method is as follows::

- For atom i , find its 20 nearest neighbor atoms;
- Pair those neighbor atoms. A "pair" means two atoms with similar distance to atom i while in the opposite directions (shown in Figure 5.1).
- For the nearest 6 pairs, determine the vector sum. Mark the atom by different colors based on the value of the vector sum.

Based on this simple algorithm, the Centro-symmetry method can distinguish atoms that are not in Centro-symmetry configuration from the equilibrium atoms

that are in perfect Centro-symmetry configurations. However, this method can not tell the difference between twin interfaces and dislocations. Therefore we have developed a new method to identify atoms in twin boundaries, which combines the nearest neighbor method and the Centro-symmetry method.

The goal for the new method is to identify and classify defect atoms in dislocations, on surfaces and on twin interfaces. First we need to understand the character of twin interfaces in an FCC lattice (Figure 5.2). An atom at the HCP position (such as twin interface) has the following characteristics:

- It has 12 nearest neighbors;
- The total vector sum of the distance between this atom to all its 12 neighbors is 0
- However, the Centro-symmetry sum of this atom is not 0

Our algorithm of the new visualization method is described below:

- For each atom, check if it has 12 nearest neighbors within a certain cutoff distance, if not, mark it as on a surface, void or a dislocation.
- For all remaining atoms, check if all its neighbors stay around it in a balanced way by summing all 12 neighbor vectors together. If the sum of the vectors falls within a certain tolerance, it is balanced. If not, mark it as distorted atoms.

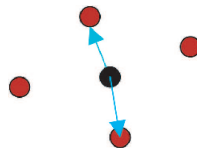


Figure 5.1: Illustration of the Centro-symmetry method

- For the remaining atoms, use the Centro-symmetry method to check if it is the perfect FCC lattice structure. If it has 12 neighbors that forms 6 Centro-symmetry pairs, it is a perfect FCC lattice. Otherwise, mark it as a twin interface.

By applying this new identification method, we are able to identify different types of defects, and provide more information for the analysis of the deformation mechanisms. At the same time, the mulit-step treatment increases the calculation speed by avoiding the Centro-symmetry calculations for every atom, which is very time-consuming.

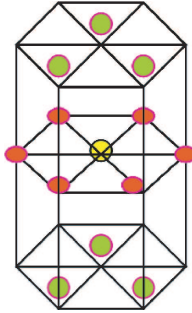


Figure 5.2: Atoms identified at a twin interface in an Fcc crystal.

5.2 Deformation of Nano-twinned Copper Crystals

5.2.1 Numerical Model

As shown in Figure 5.3, the simulation box contains 57600 Cu atoms, with the size of 20 nm in the x and y directions, and 4nm in the z direction. Periodic boundary conditions are applied along the z-direction. Free surface boundary conditions are applied along the x-direction. Shear strain with a constant strain rate of $5 \times 10^8/s$ is applied on the top and bottom layers and the boundary is fixed. Then the computational box is relaxed by molecular dynamics for 0.25 ns

at a temperature of 20 K. A single CPU can finish 250,000 MD steps in 3-5 days.

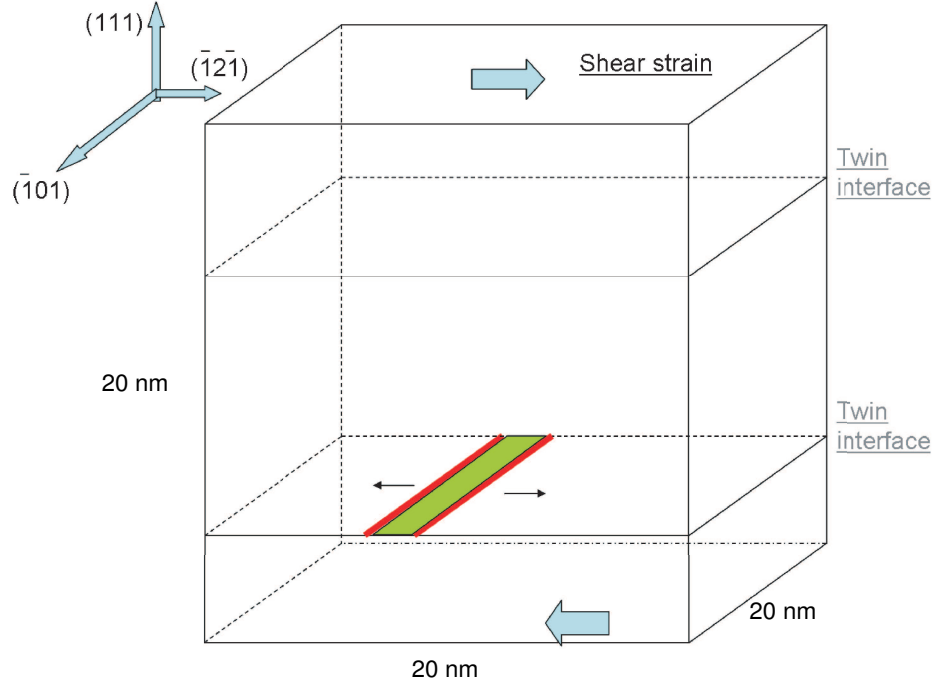


Figure 5.3: Schematic illustration for the computational box used in MD simulations of the Cu twin structure.

We can get the force information on each individual atom from the MD simulation. In order to calculate the strain and stress information for the system, we use the free-body diagram shown in figure 5.4. The strain is calculated from the average displacements of all atoms, as:

$$\varepsilon = \frac{\Delta L}{L} \quad (5.1)$$

To calculate the stress, let's consider the atoms within the middle layer of the box. Under the equilibrium conditions, the atoms will feel a force from the atoms above and below the layer. These two forces should be equal in magnitude but and be opposite in directions. Therefore the net force on this layer of atoms will

be zero under equilibrium. Now if we keep the atomic positions unchanged, and remove the atoms above that layer, then the atoms within that layer will only feel the force from the atoms below them. We can thus calculate the forces on all atoms in the middle layer, and hence the average layer stress. The method is applied to both shear and tension, as shown in Figure 5.4.

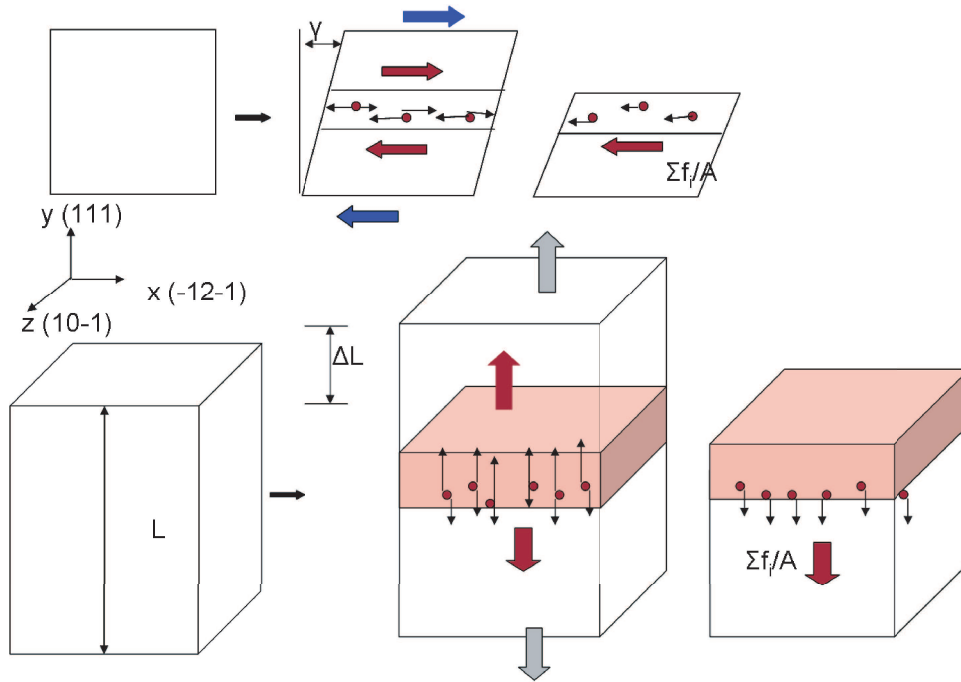


Figure 5.4: A schematic of the computation method for calculations of atomic level stress and strain.

5.2.2 Results

Figure (5.5 - 5.8) show snap-shots of a time sequence for the atomic positions of atoms in defect configurations within the simulation box. The simulation is for a single copper crystal under a high tensile/shear strain rate of $5 \times 10^8/s$. White atoms in the figures mark those in HCP positions (twin boundary or stacking fault); while red atoms mark those atoms with nearest neighbors less

than 12 (e.g. the surface); and blue atoms mark atoms with more than 12 nearest neighbors (e.g. atoms around dislocations). Atoms in perfect positions are not shown for clarity.

When the simulation box is subjected to a high tensile strain rate ($5 \times 10^8/s$),

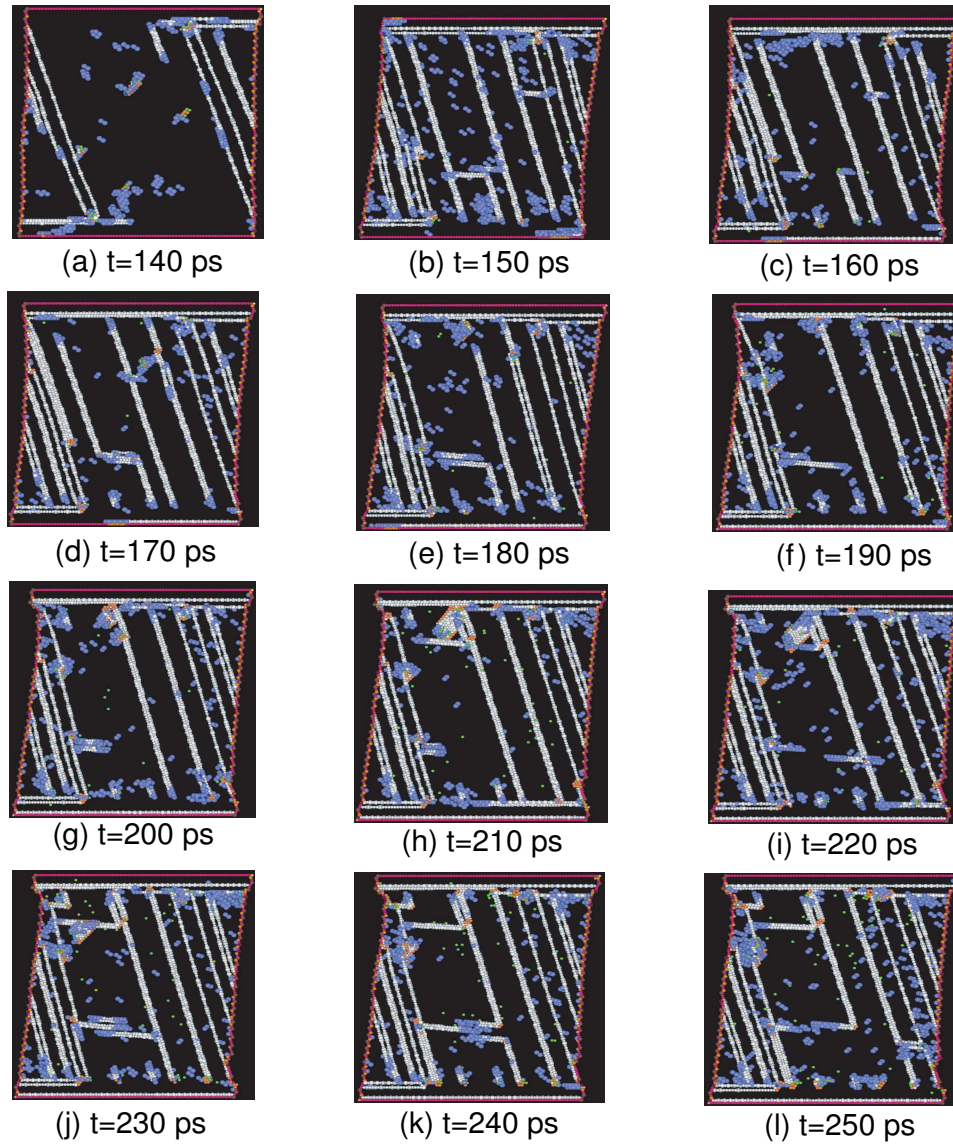


Figure 5.5: Time-sequence of atoms in defect positions in a copper single crystal subjected to a high tensile strain rate of $5 \times 10^8/s$.

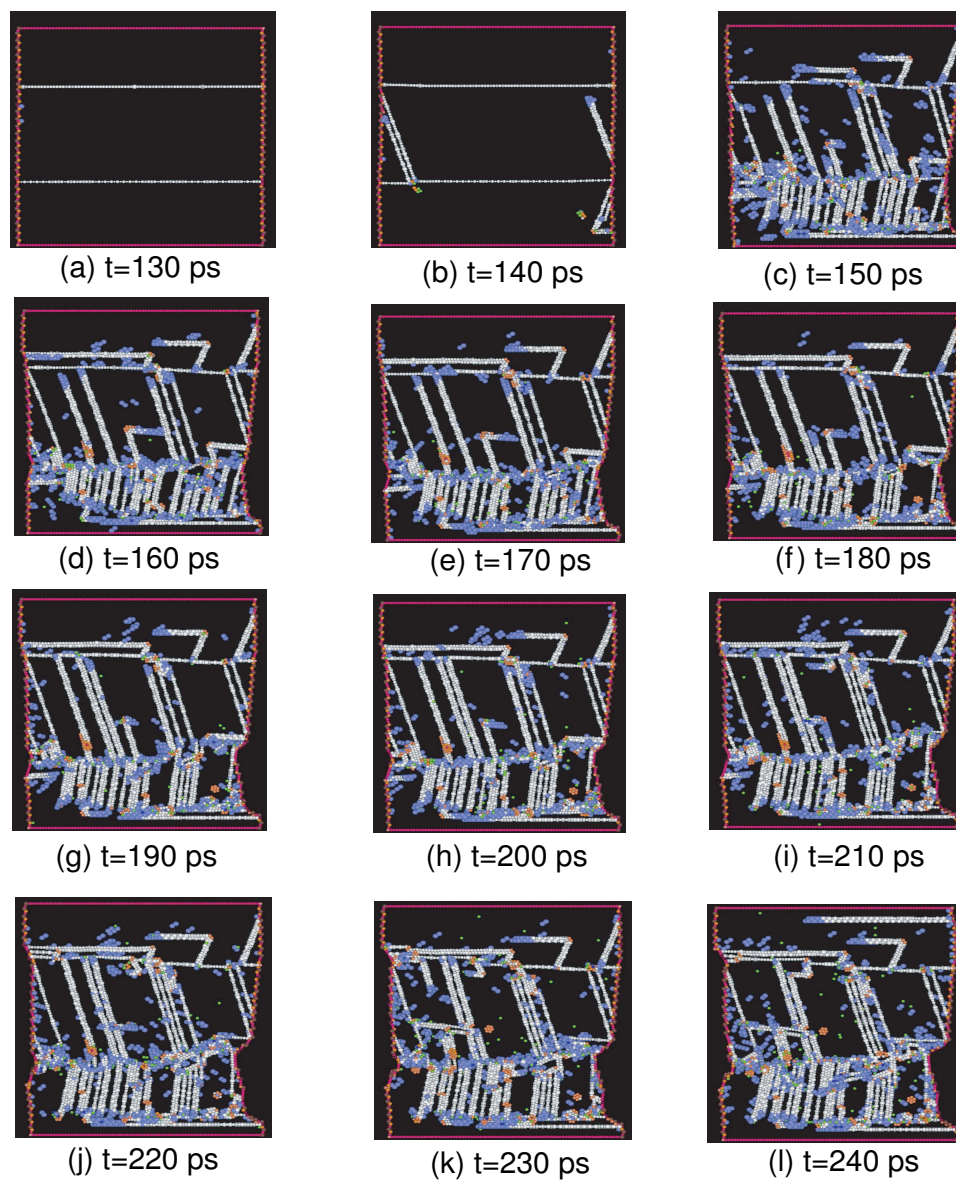


Figure 5.6: Time-sequence of atoms in defect positions in a 3-layer twinned copper crystal subjected to a high tensile strain rate of $5 \times 10^8/s$.

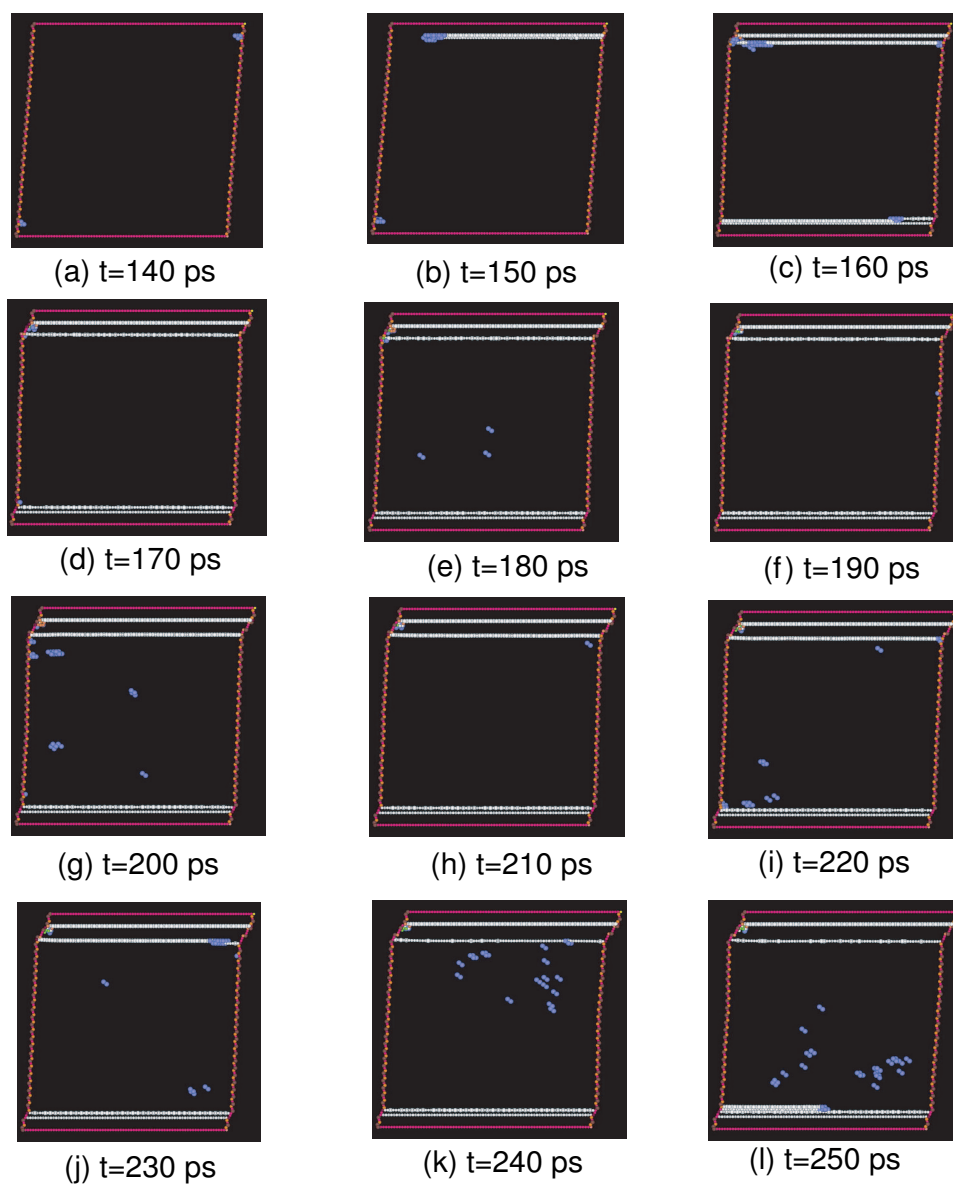


Figure 5.7: Time-sequence of atoms in defect positions in a single crystal subjected to a high shear strain rate of $5 \times 10^8/s$.

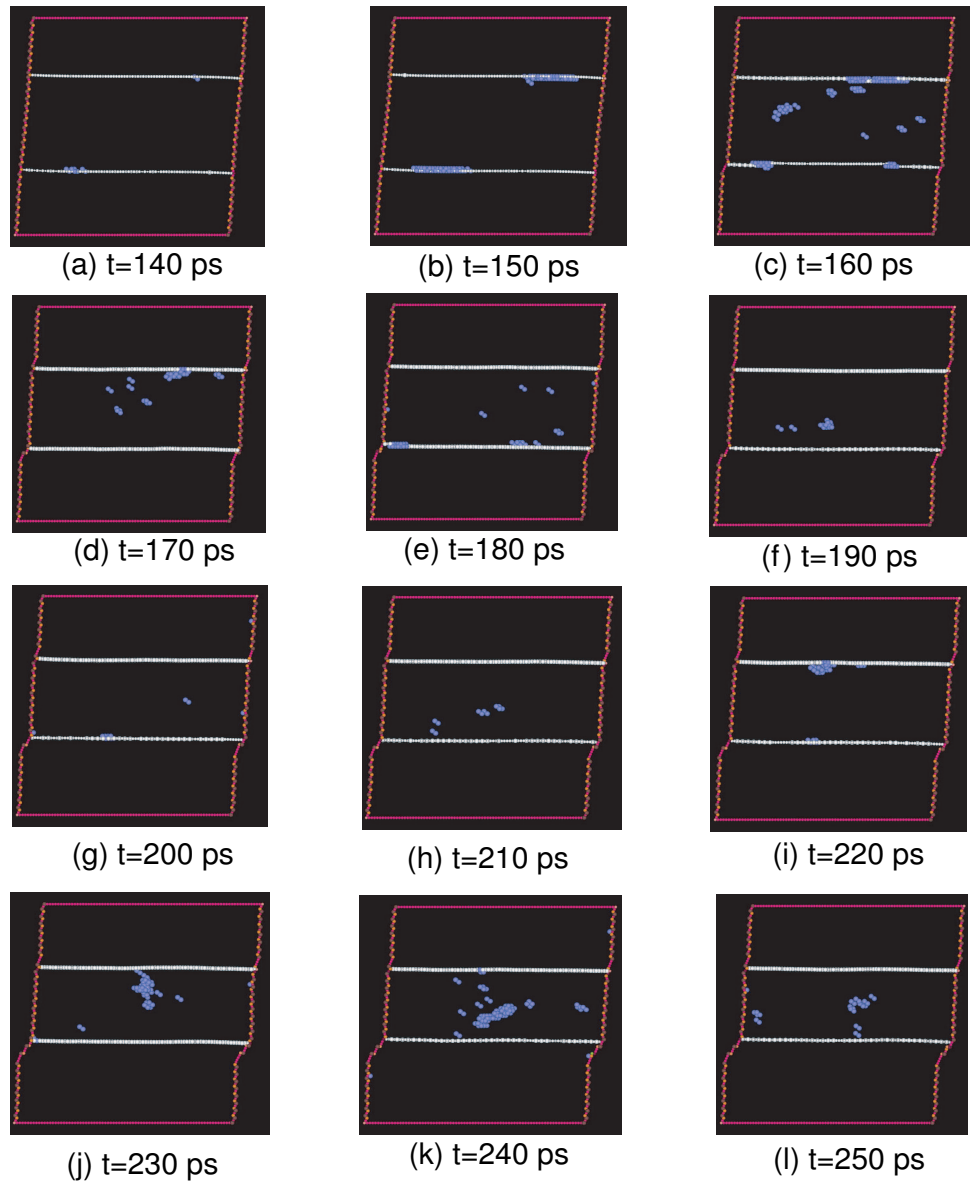


Figure 5.8: Time-sequence of atoms in defect positions in a 3-layer twinned copper crystal subjected to a high shear strain rate of $5 \times 10^8/s$.

a large number of twins are formed along (111) plane in single copper crystals. The density of twinned planes as a function of time is shown in Figure 5.9.

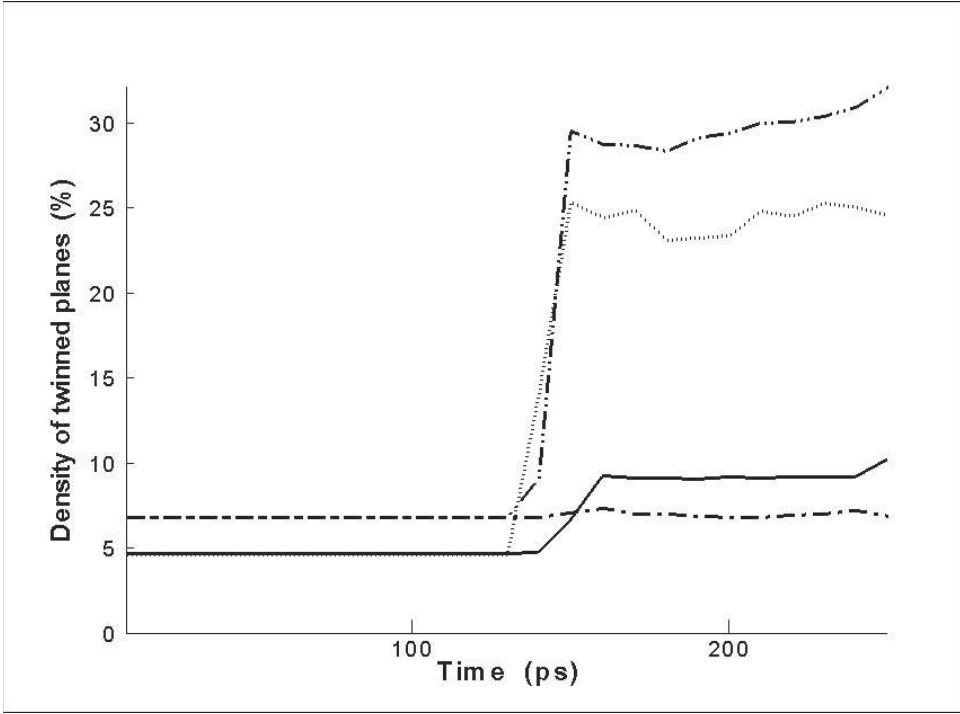


Figure 5.9: The density of twinned planes as a function of time under strain rate of $5 \times 10^8/s$. (a) Dotted line: a copper single crystal subjected to a high tensile strain, (b) dashed dot dot line: a 3-layer twinned copper crystal subjected to a high tensile strain, (c) solid line: a single crystal subjected to a high shear strain, (d) dash dot line: a 3-layer twinned copper crystal subjected to a high shear strain.

Under shear strain, if there are already twin interfaces present, kinks are formed at twin interfaces leading to the migration of the twin interface as will be described in detail next. In other cases, where there are no original twin interfaces, dislocations are generated from surfaces and glide on (111) planes. A leading Schockley partial dislocation of a Burgers vector $\frac{1}{6}[112]$ is first nucleated from the surface, followed by the formation of a pair of twin interfaces on adjacent planes. This, a nucleus of a nano-twin is formed at the end of this process.

The corresponding stress-strain curves are calculated using the method de-

scribed in section 5.2.1, and are shown in Figure 5.10. The stress-strain curves show that the deformation process starts in an elastic manner up to a strain of about 7%. Beyond this level of strain, dislocations are nucleated, giving rise to plastic deformation via dislocation motion and nano-twin region formation. System failure is achieved at a strain of about 12-15%.

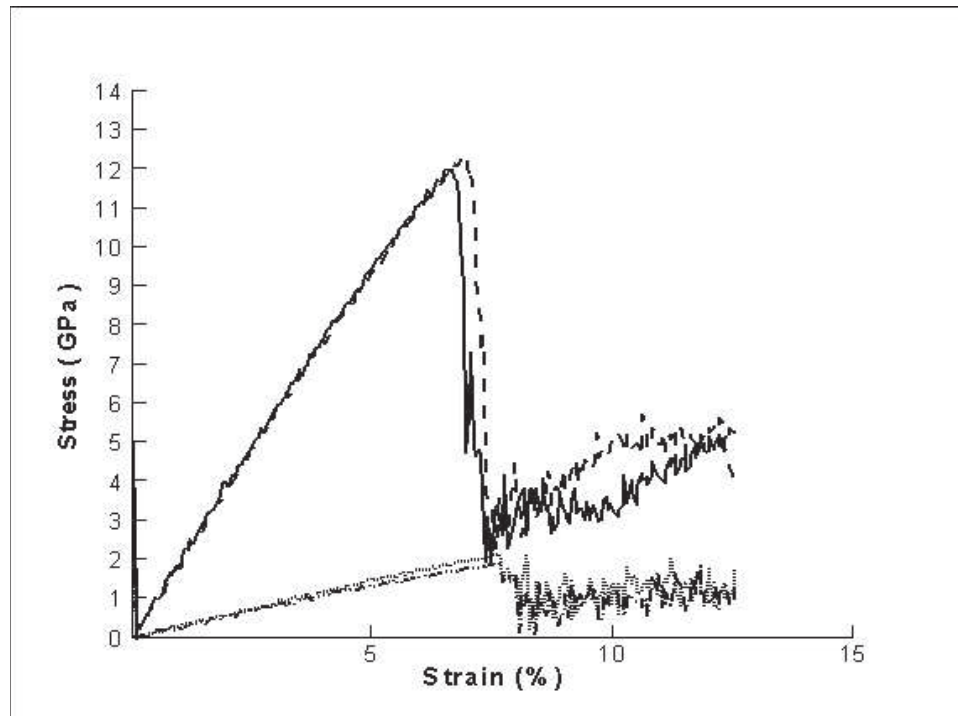


Figure 5.10: Stress-strain curves for deformed copper crystals. (a) Solid line: tension of a single crystal, (b) dash line: tension of a twinned crystal, (c) dot line: shear of a single crystal, and (d) dash dot dot line: shear of a twinned crystal.

The stress-strain curves behavior for single crystals and for crystals with twinned interfaces are similar. The twinned crystal is a little stronger, which may be explained by the additional interaction of the original twin surfaces with dislocations, preventing their glide. The difference is very small because the strain rate is very high and the whole system does not have enough time to reach equilibrium in response to the applied strain rate. Therefore the strengthening

mechanism of original twin interfaces is not obvious. In the following sections we will perform simulations of the twin structure with more relaxation time to show more evidence of the mechanism of twin interface hardening.

As we can see from Figure 5.8, when there are twin interfaces, the twin interfaces will migrate under the applied shear strain which is parallel to the twin interface. To obtain a more detailed view on the twin interface migration mechanism, we take a closer look at smaller time steps (as shown by the time-sequence snapshots in Figure 5.11).

From Figure 5.11, it is clear to see that first point defects form in a high energy zone, which is also a region of stress concentration area. Point defects accumulate and finally spread throughout the entire section on the x-y plane, since the z direction is periodic, becoming full dislocation line defects, and act as the dislocation sources. After that we can see 2 dislocations nucleate from this region and glide in opposite directions along the twin interface (111) plane. These two dislocation loops have opposite Burger's vectors so that the sum of the Burger's vector is zero. The dislocation loops glide under the applied shear strain and finally get absorbed by the surfaces. As a result of the dislocations gliding over the whole twin plane, the twin interface moves one layer up or down depending on the twin orientations. Comparing the time-sequence of atomic positions with the stress-strain curve, we can correlate the inflexion points in the stress/energy curves exactly with the start of gliding of dislocations, which is marked the deformation transfer from elastic region to plastic region.

However, the detail study in Figure 5.11 is restricted by the 2D setup of the simulation box. As a consequence, all possible glide systems are not allowed here, and we need to consider a truly 3-D system to generalize these conclusions. The result is limited by only a few slip systems. In order to obtain more realistic

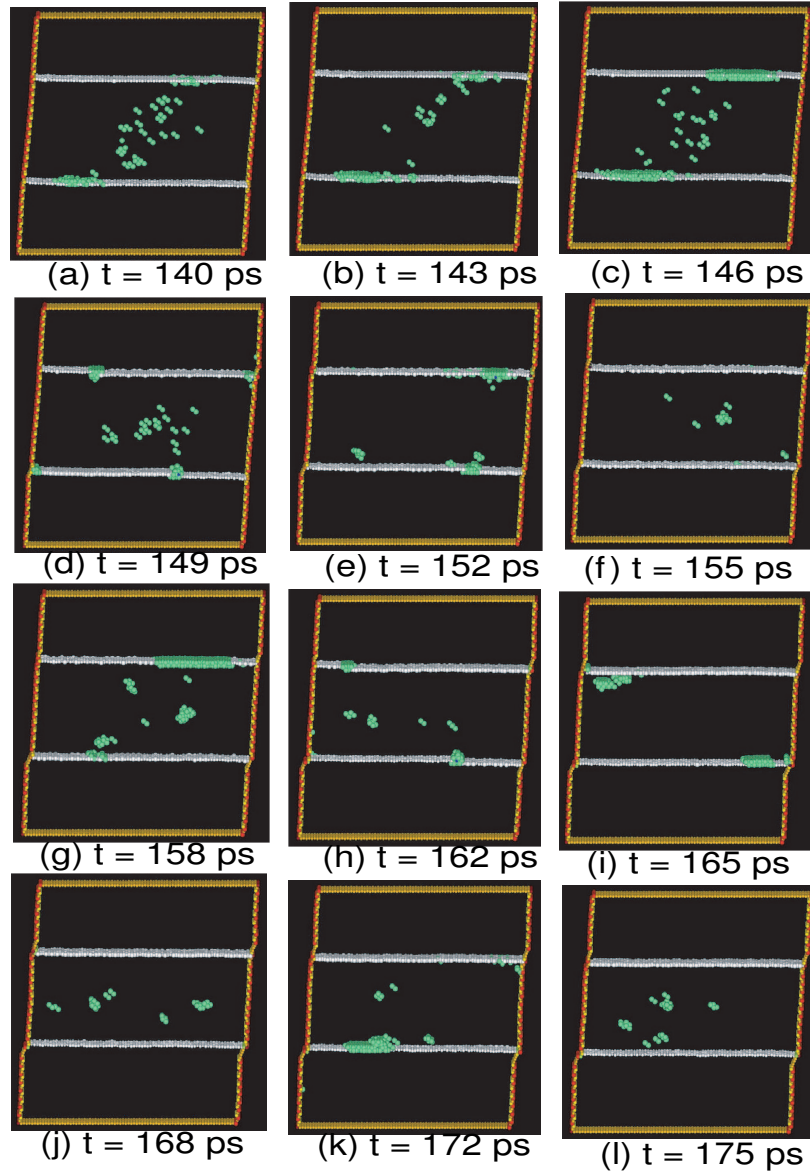


Figure 5.11: Detailed time-sequence of atoms in defect positions in a 3-layer twinned copper crystal subjected to a high shear strain rate of $5 \times 10^8/s$.

results, and get more insight into the twin boundary migration mechanism, we conduct computer simulations using a 3D model that will be described next.

5.3 Twin Boundary Migration (TBM) Mechanism

5.3.1 Computational Model

To investigate the mechanism of twin boundary migration in twinned copper nano-layers, we begin by setting up a simulation box as shown in Figure 5.12. The corresponding atomic configuration of twin boundary atoms is shown in Figure 5.13. The x , y and z axes of the simulation cells are selected as $[110]$, $[\bar{1}\bar{1}\bar{1}]$, and $[\bar{1}\bar{1}2]$, respectively. The twin interfaces are on y planes. The simulation box is 20 nm along all the x , y and z directions, and consists of 0.5 million atoms. Uniform shear strains on the $(\bar{1}\bar{1}\bar{1})$ -plane along the $[110]$ direction are applied. This is realized in two stages: first, the system is preloaded at 6.9% uniform shear strain, and second constant strain rates in the range $5 * 10^7/s$ to $5 * 10^9/s$ are applied. The top and bottom boundary layer atoms are fixed after each shearing step. Atoms in the cells are then allowed to relax. Mishin potential for copper is used throughout these simulations [51] The behavior of atom movement was studied and visualized using the local crystallinity classification method discussed in section 5.1. The wavelength of nano-twins is in the range of 7 nm, and the simulation is conducted at a temperature of 300 K.

5.3.2 Simulation Results for Twin Boundary Migration

Figure 5.14 shows a time sequence of the process of twin boundary migration as a result of the nucleation and spreading of two Schockley partial dislocation loops. The white atoms represent those with the number of nearest neighbors different

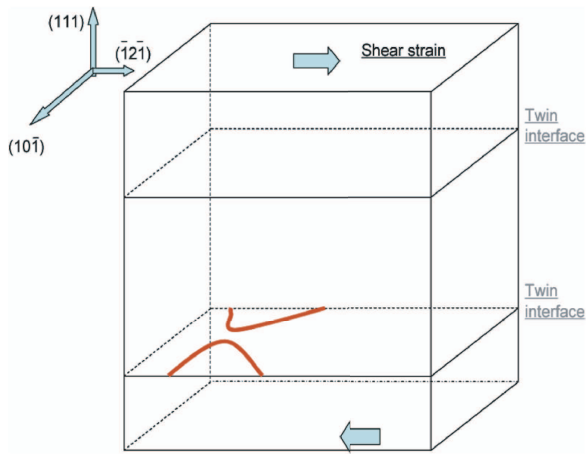


Figure 5.12: Schematic of the computational model for twin boundary migration simulations

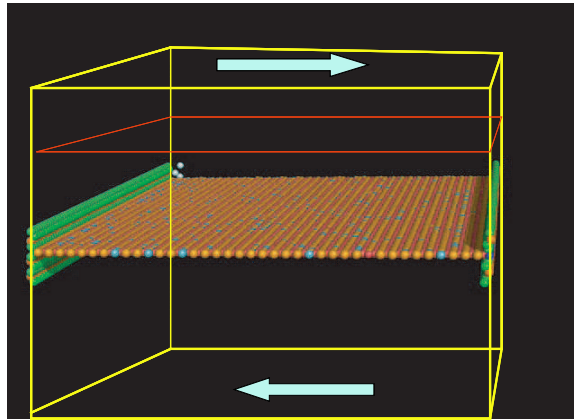


Figure 5.13: 3D view of the simulation box for twin boundary migration

from 12. They are either in a dislocation core or represent severe lattice distortion. The red atomic plane is the original twin interface. The green atomic plane is the new twin interface, which is one-atomic layer higher than the red plane. We can clearly see several stages of the twin boundary migration mechanism illustrated in figure 5.14: (a) At 0.2 ps, the twin boundary before migration. (b) and (c) At $1 \sim 1.8$ ps, coherent motion of highly distorted or interstitial atoms nucleate from the left side surface and slip towards right side. We will later show that these atoms are in highly distorted elastic configurations and are not associated with dislocations. (d) At 4.6 ps, the coherent group of defects moves along the (111) plane and then disassociates on the front and back surfaces. (e) At 5.6 ps, curved partial dislocations nucleate at the intersection of the twin boundary and the interface. We will also show that the Burgers vectors for these dislocation lines to be Schockley partials. (f) At 7.8 ps, the partial dislocations slip over on a (111) plane adjacent to the twin boundary leading to the migration of the twin boundary. (g) At 8.4 ps, the two curved partial dislocations merge in the middle of the cell (h) At 9 ps, a new partial dislocation loop nucleates at the merge point, spreading outwards, followed by the formation of a new twin boundary that is one layer higher than the old one.

In order to better understand the nature of the defects as a time-sequence in Figure 5.14, a dislocation character analysis is required, and we pursue here a modified Burgers circuit analysis across the twin boundary interface. Figure 5.15 shows the Burgers circuit to identify a Schockley partial dislocation along the twin boundary interface, leading to step generation on the interface (a twinning dislocation), and the migration of the twin interface one atomic layer. The orientation in this picture is the same as the one used in Figure 5.14. The x , y and z axes of the simulation cells are $[110]$, $[\bar{1}\bar{1}\bar{1}]$, and $[\bar{1}\bar{1}2]$, respectively. The white atoms are in perfect lattice positions, the blue atoms mark the twin boundaries

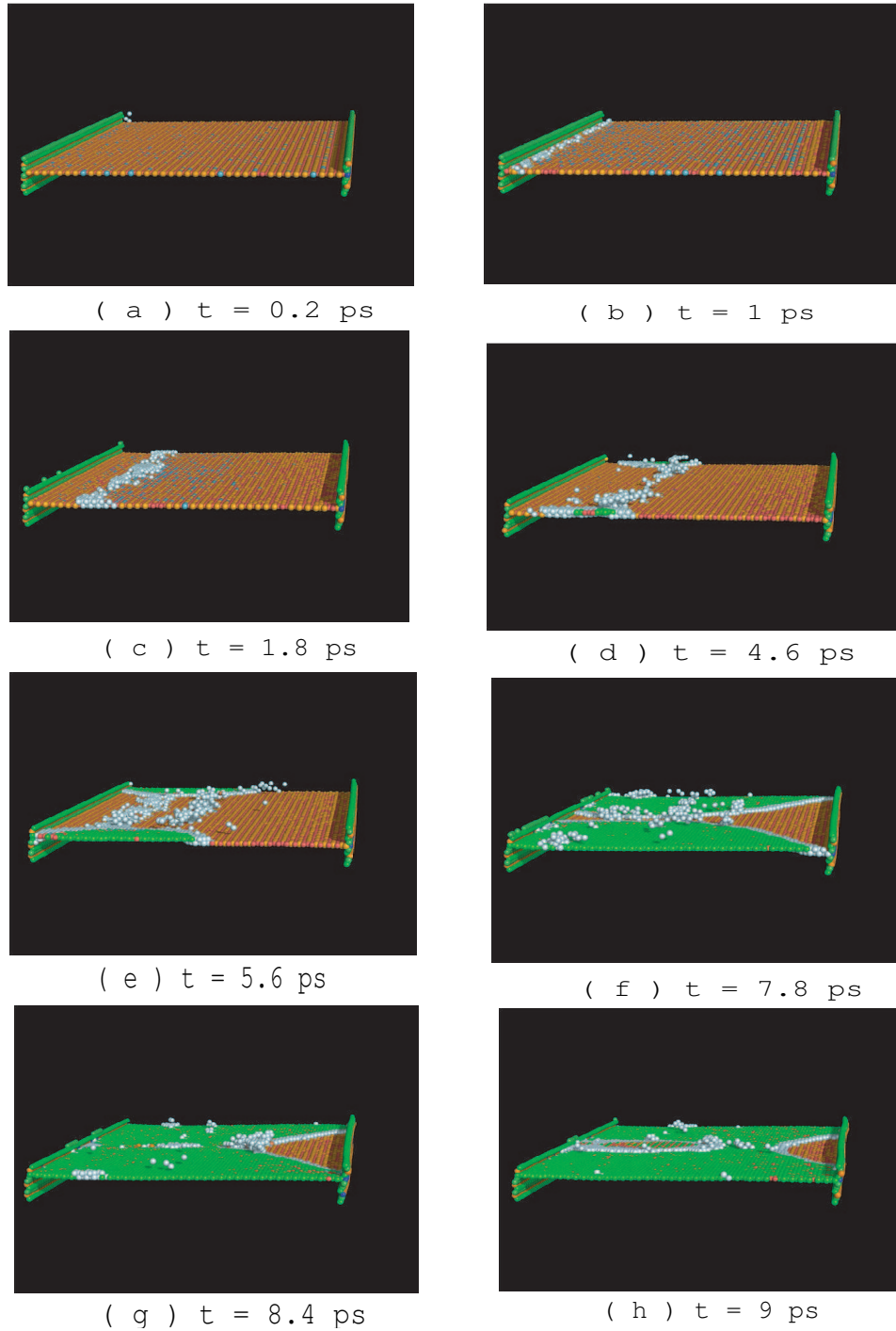


Figure 5.14: The 3D visualization of dislocation nucleation and motion on the twin boundary: The white atoms represent defect atoms which align together to form dislocations. The red atomic plane is the original twin interface. The green atomic plane is the new twin interface which is one-atomic layer higher than the red plane.

and the yellow atoms mark atoms comprising the dislocation line.

If we make a circuit around the dislocation core, we can find the Burgers vector if the circuit doesn't close. Because there is a twin boundary in the lattice, the method to draw the Burgers circuit has to be modified from the method used for single crystals. The method for drawing the Burgers circuit for a twinned crystal is shown in Figure 5.15 as an example. We start from a point (the left-low corner of the yellow circle), then we go upwards 5 steps of atom spacings along the lattice orientation "1" till we reach the twin boundary, then we have to adjust the direction while still going upwards, to fit the new lattice orientation "2" after crossing the twin boundary. We continue in this new orientation for 12 atomic spaces, then go towards the right for 20 steps, and finally proceed downwards. The basic idea here is that when we go downwards, we have to follow exactly the same number of steps in both orientations before and after crossing the twin interface. So we will move 12 steps down along orientation "2", although we will cross the twin interface after 11 steps. Then we change the direction and continue in orientation "1" for 5 steps. Finally, we proceed to the left for another 20 steps and finish the Burgers circuit. At the end of the circuit, we find that it can not be closed. The vector between the start point and end point is the Burgers vector for the dislocation surrounded by the Burgers circuit. The vector is found to be $\frac{1}{6}[112]$, and is perpendicular to the dislocation line, and we thus conclude that the nucleated dislocation is an edge Schockley partial.

Figure 5.16 shows a planar view of the same configuration as that of figure 5.15, but from a different angle. The plane parallel to the paper is the (111) plane and the atoms shown are the atoms across the dislocation, new twin boundary and one layer above the old dislocation. By carefully comparing the relative positions of the atoms with their neighbors on the layer below them, we find that

all atoms on the right side of the dislocation line are displaced along the arrow relative to the left side of the dislocation line. This displacement vector is also confirmed to be $\frac{1}{6}[112]$.

Figure 5.17 shows the relative positions between 2 layers of atoms at the dislocation line. The plane parallel to the paper is the (111) plane. Green atoms are the top layer, while white atoms are one layer below. In an FCC lattice, the (111) plane has 3 different atomic arrangement, and we can call them A,B and C, respectively. Usually, if we have an ABCABC lattice structure, the crystal is a perfect lattice. The dislocation is a group of atoms gliding together from one position (e.g. A) to another position (e.g. B) on top of the C layer. Figure 5.17

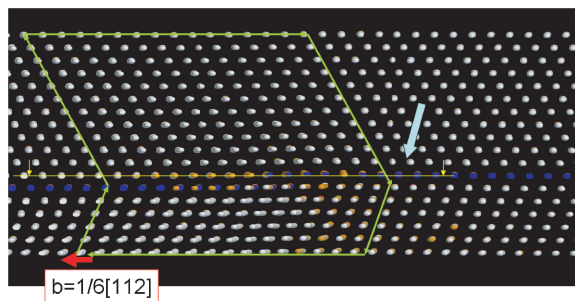


Figure 5.15: Burgers Circuit identifying a Schockley partial dislocation.

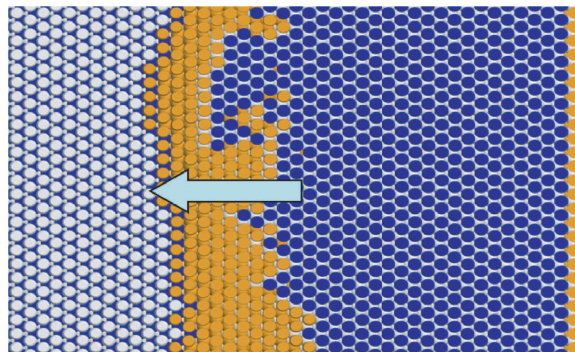


Figure 5.16: Plane view of the relative displacement of two parts of the crystal near the partial dislocation.

shows the dislocation line, and the atoms are in a transition state of gliding from A positions to B positions on top of C positions. The figure clearly describes the Burgers vector (the relative displacement between one part of the lattice on one side of the dislocation to the other part of the lattice). The Burgers vector is along the $[11\bar{2}]$ direction and the magnitude is $\frac{1}{6}[11\bar{2}]$. Figure 5.18 is a sketch of the orientations, and lattice structure on the (111) plane while atoms are in a transition state.

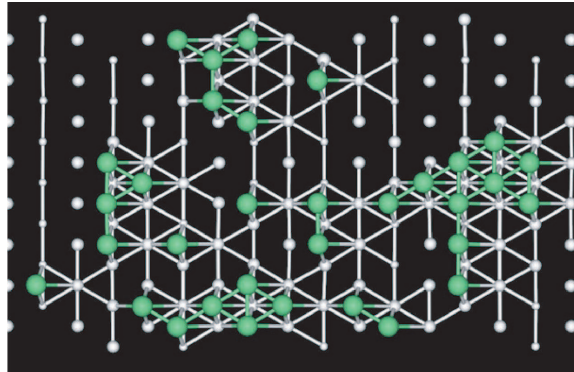


Figure 5.17: The relative position between 2 layers of atoms at the dislocation line.

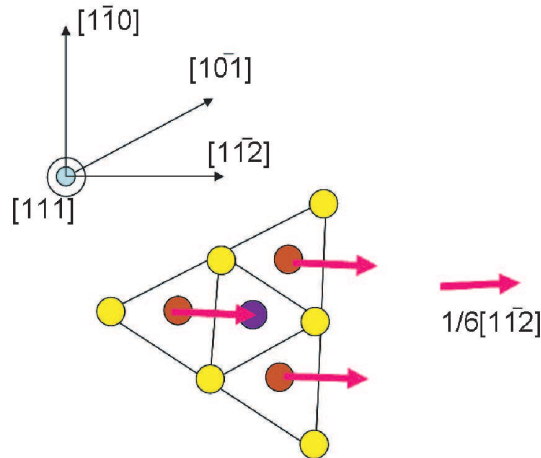


Figure 5.18: A sketch of the relative positions between 2 layers of atoms at the dislocation line.

We also applied a similar Burgers vector analysis method for curved dislocation lines, as shown in Figures 5.19 and 5.20. Figure 5.19 shows a plane view of the curved dislocation on the twin interface plane. All atoms within the half loop have been displaced along the yellow arrow relative to the remainder of the crystal lattice. Figure 5.20 shows a Burgers circuit along the dislocation core. The two circuits are for two segments of the dislocation line, but they belong to the same curved dislocation line. The Burgers vector is still $\frac{1}{6}[112]$, as shown in the figure. The two segments of the dislocation line illustrated in figure 5.20 are of the edge type. However, the dislocation curve is of the mixed type depending on the curve orientation relative to the Burgers vector.

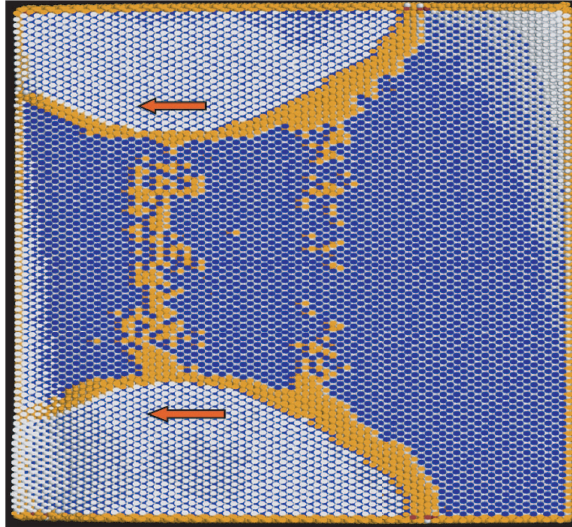


Figure 5.19: Plane view of the relative displacement of the two parts of the crystal near the curved partial dislocations.

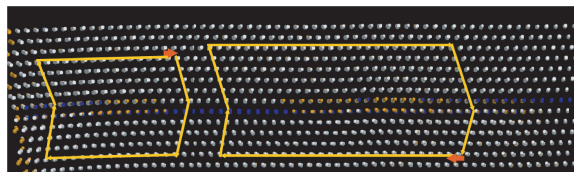


Figure 5.20: Burgers Circuit for the curved partial dislocations

In Figure 5.14 (b) and (c), we observe a group movement of defects nucleated from one side of the surface while they slip towards the right side. We also examine the Burgers circuit for those atoms. The circuit and a plane view is shown in Figure 5.21 and Figure 5.22, respectively. We can see that the Burgers circuit is closed so that there is no Burgers vector around those lines. This indicates that the atoms showing group movement as a line do not actually comprise dislocations. They are just atoms near the region which is bent due to the applied strain and boundary restrictions. Since the visualization method use a cutoff distance to calculate the number of the nearest neighbors, the bending of the structure will cause a change of the number of nearest neighbors, and we therefore mark those atoms as defects. However, their deformation should still be considered elastic.

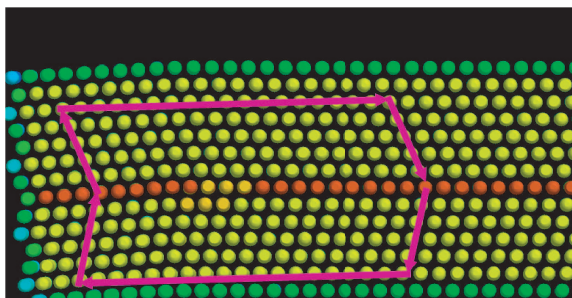


Figure 5.21: A complete Burgers circuit around atoms in high deformation regions illustrate the lack of a dislocation there.

5.3.3 Mechanism of Twin Boundary Migration (TBM)

Figure 5.23 shows a sketch that illustrates the twin boundary migration mechanism as a consequence of Shockley partial nucleation and motion in an FCC crystal. This mechanism was first suggested by Hirth and Lothe [32]. However, our current MD simulations clearly show the conditions, configuration, and motion of Shockley partials leading to the twin boundary migration. Suppose we

have a twin boundary with layers

ABCAB|C|BACB.

The layers above the boundary have the layout of ABC and the layers below the boundary have the layout of CBA, where C is the twin boundary here. If a partial dislocation glides over a (111)-type plane adjacent to the twin boundary, it will move all lattice atoms in an area above its slip plane a distance equal to the magnitude of one Burgers vector. So the layer of atoms in B positions will be moved to an A position. Simultaneously, atoms in C positions will move to B positions, and those in an A position will move to a C position, etc. As the Shockley partial glides over the twin boundary interface, all atoms in the upper part of the crystal will be moved according to the described sequence outlined here. Finally (111)-type atomic planes in the crystal lattice will have the following sequence:

CABC|A|CBACB,

and thus the upper half of the lattice will still have the layout of ABC, while the lower half remains in the layout of CBA, but the twin interface has moved one layer upward and A is the new twin interface.

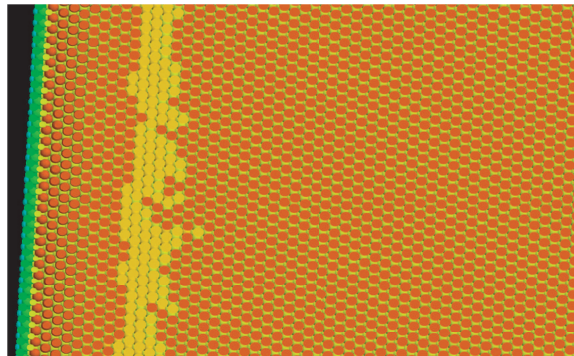


Figure 5.22: A plane view around atoms in high deformation regions illustrate the lack of a dislocation there, because there is no relative displacement for the atoms on different sides of the yellow line.

we show here that the dominant deformation mode in copper under high strain rate is by mechanical twinning and that the deformation is mainly attributed to TBM. The mechanism of TBM is shown to be controlled by the nucleation and spreading of $1/6[121]$ -Shockley partial dislocations at the boundary interface. We discover here that the nucleation of a Shockley partial dislocation loop is induced by the coordinated thermal motion of atoms in a coherent non-linear "wave", since atomic displacements of atoms in this wave far exceed elastic deformation. Nucleation of Shockley partials involved in the TBM mechanism is not homogeneous, but is initiated at three sites: on the layer directly adjacent to the twin boundary, at the surface of the crystal, and at stress concentration regions associated with the motion of a non-linear elastic wave through the crystal. Shockley partial dislocations glide under the applied shear strain and lead to twin boundary migration upward one layer. When two Shockley partial dislocation loops

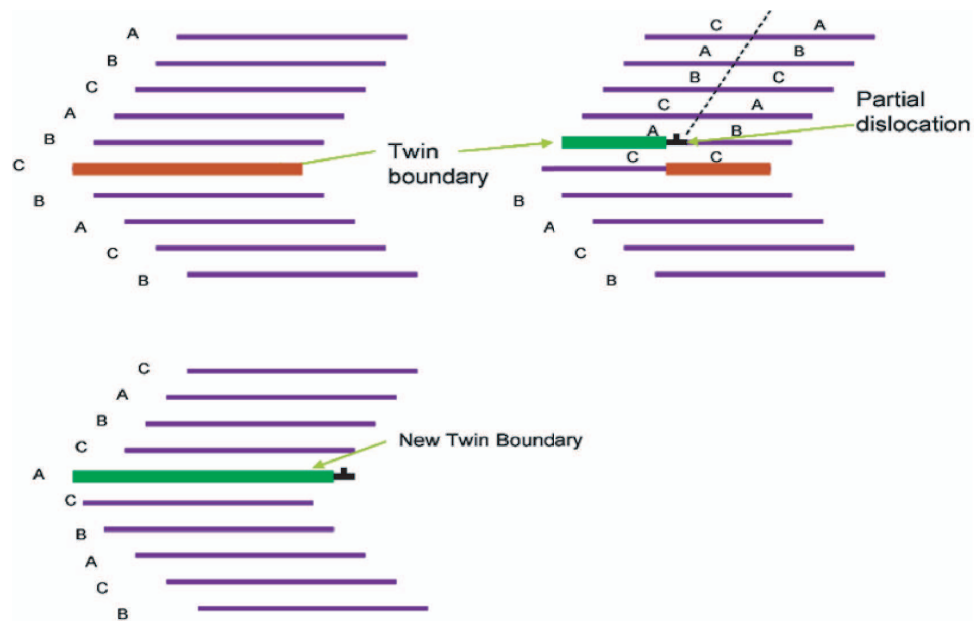


Figure 5.23: Sketch of the twin boundary migration mechanism leading by a Shockley partial dislocation in an FCC crystal.

with the same Burgers vector merge together in the middle of the slip plane, the local stress is so large that a new dislocation loop nucleates on top of the merge point, and on the plane adjacent to the newly-formed twin boundary. Thus, the mechanism is repeatable with alternating nucleation sites of Shockley partial loops between the boundaries and the center, and lead to the continuous motion of the twin boundary.

5.4 Size Effects on the Deformation of Nano-Twinned Copper

In this section we discuss the effects of the nano-laminate size on the deformation of the nano-twinned copper structure. We present here our studies of different nano-twinned Cu structures with different twin layer thickness (wavelength) and focus on understanding the hardening mechanism of ultra-high strength of nano-twins.

5.4.1 Computational Model for nano-twinned Copper crystals

The simulation box is set up to have multi-layers of Cu twin structure with wavelengths of 3 nm, 4 nm, 5 nm, 6 nm, respectively. Single crystals are also simulated to provide a reference for understanding influence of the twin size on mechanical deformation in twinned copper crystals. The twin orientation is randomly selected. Computer simulations have been performed under either constant applied stress or strain, for both tension and shear. In all of the following simulations, the system temperature is maintained at 300K, and when the quench method of section 3.1 is used, a time step of $5 \times 10^{-15} s$ is adopted. The applied strain or stress is applied through the top and bottom about thirty atomic layers (this layer is parallel to the x-z plane). After stress or strain are applied to the top or bottom layers, atoms in these layers were further constrained from motion

in all directions during shear, while they are constrained to move on the x-z plane during tension. In the following figures representing snap-shots of a time-sequence of the deformation, we rotate the box along the y axis so that the norm of the grown-in twin interfaces, which are (111)-planes, are within the paper plane. The green atoms represent atoms in an HCP configuration (twin or stacking fault).

5.4.2 Mechanical Twinning

In the FCC lattice, 4 possible plastic (irreversible) deformation mechanisms may be operative, depending on the conditions of deformation, and these are:

(1) Stacking Faults Extension (SFE). In this mechanism, one Shockley partial dislocation extends across the entire grain, leaving a stacking fault behind.

(2) Full Dislocation Motion (DM). Here, plastic deformation is achieved by the irreversible motion of a leading and a trailing partial on the same slip plane, leaving no dislocation debris behind, but resulting in a shear displacement on the glide plane.

(3) Mechanical Twinning (MT). Here, the leading and twinning partials on two adjacent (111)-planes nucleate an extrinsic stacking fault or a twin-boundary of thickness of three-layer. This nano-twin structure is the precursor for deformation twinning (DT).

(4) Twin Boundary Migration (TBM). In this mechanism, slip activity occurs via the emission of a partial at the intersection of the twin and the GB moving slip on a (111)-plane adjacent to the TB. This is a reversible form of deformation, since twins can migrate back and forth if the stress is reversed.

In the simulations we performed under tensile strain, we observed the abundance of mechanical twins. Figure 5.24 shows a time-sequence for a nano-twin system under an applied tensile strain. The wavelength in this simulation is 3nm.

The simulation starts with atomic relaxation at a rate of $10^{10}/s$ (relax for 20 time steps with step size $5^{-15}s$ for every 0.1% strain). We observe from the figure that many new stacking fault planes (green atoms here) grow from the original twin interface and occupy the space between the original twin interfaces. The areal density of stacking faults is very high. Figure 5.25 gives a clear view of those stacking fault layers. Blue atoms represent original matrix atoms and green ones show the stacking fault layers. We observe here that the green layers always show up in pairs, so that mechanical twinning is initiated. The twin orientations are shown by the yellow line in Figure 5.25.

In order to understand the conditions for mechanical twinning as a dominant deformation mechanism, we study the effect of the quench rate on the density of mechanical twins. As shown in Figure 5.26, the system undergoing a fast quench rate ($10^{10}/s$) will achieve very high stacking fault density, such as 20% when the total applied strain reaches 10% (in 10 ps), while the one with a slow quench rate ($10^9/s$) shows the stacking fault density to be around 7%-8% (in 100 ps). Therefore the higher deformation rate results in a higher twin density.

In summary, double layers of Shockley partials are found and are the dominant plastic deformation mechanism at high quench rates under applied tensile stress or strain. This is a nucleation mechanism for new twins, in qualitative agreement with experimental observations [23] [97].

5.4.3 Results for Constant Shear Strain Rate Deformation

Figure 5.27 shows a time-sequence for the deformation behavior of 3 nm wavelength nano-twinned structure under a constant shear strain rate of $10^9 s^{-1}$ using quench relaxation method, which relaxes the system to reach equilibrium at 0 K by minimizing total potential energies. In the following context, "quench rate" is used to describe the strain rate for the system relaxed at 0 K.

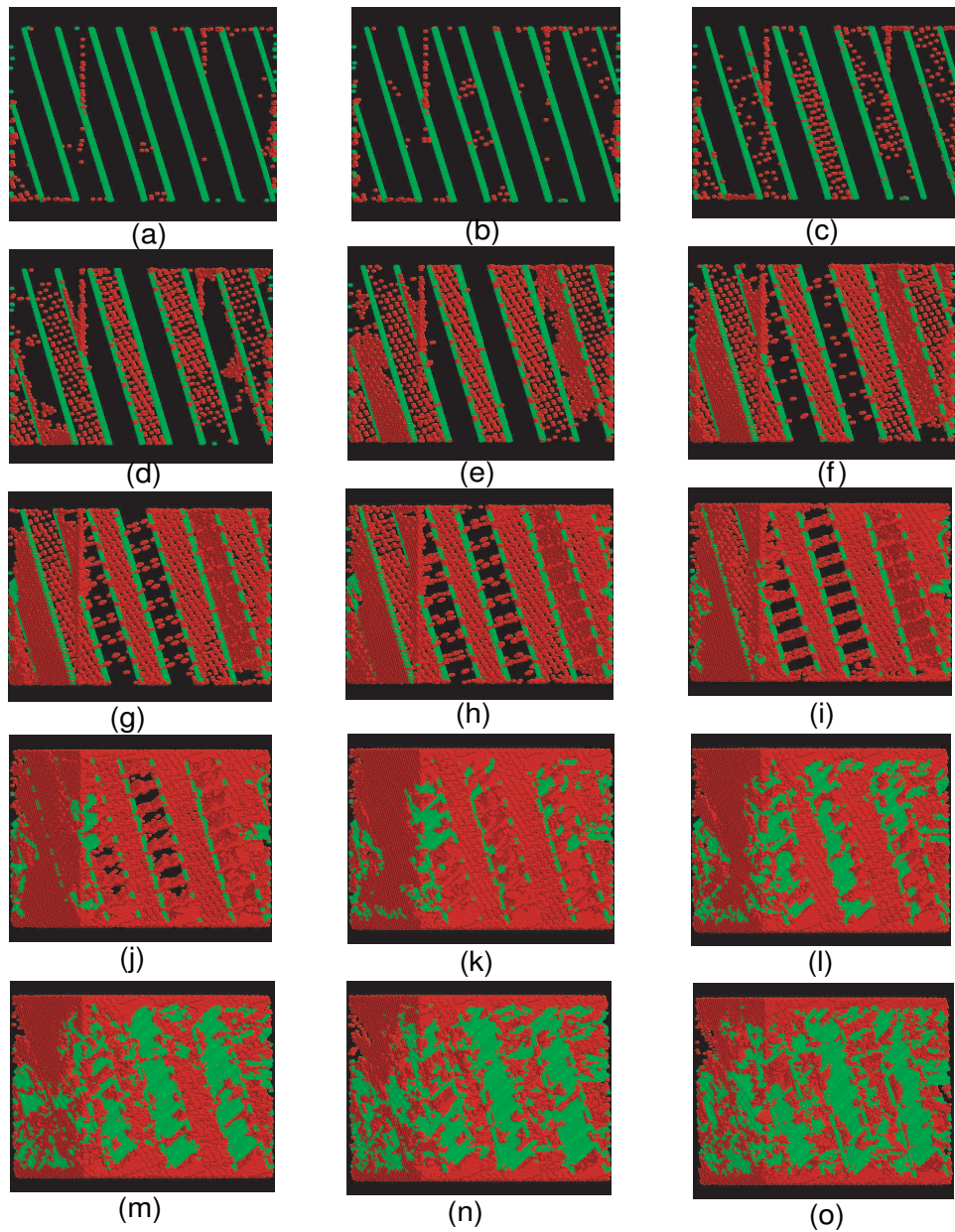


Figure 5.24: Time-sequence showing the progression of deformation in a nano-twinned copper crystal under an applied tensile strain, with fast quench relaxation. The sequence is as follows: (a) At 3 ps, strain = 3%. (b) At 3.5 ps, strain = 3.5%. (c) At 4 ps, strain = 4.0%. (d) At 4.5 ps, strain = 4.5%. (e) At 5 ps, strain = 5.0%. (f) At 5.5 ps, strain = 5.5%. (g) At 6 ps, strain = 6.0%. (h) At 6.5 ps, strain = 6.5%. (i) At 7 ps, strain = 7.0%. (j) At 7.5 ps, strain = 7.5%. (k) At 8 ps, strain = 8.0%. (l) At 8.5 ps, strain = 8.5%. (m) At 9 ps, strain = 9.0%. (n) At 9.5 ps, strain = 9.5%. (o) At 10 ps, strain = 10.0%. Green atoms are for the stacking fault layers, red represent other defects such as atoms, vacancies, noises, dislocations etc.

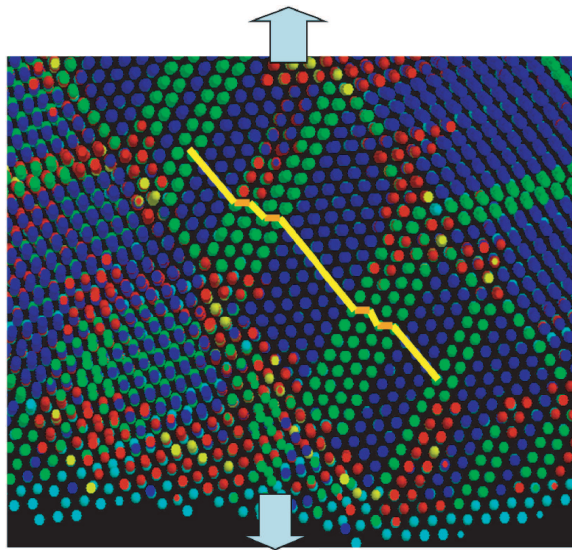


Figure 5.25: A detailed view of mechanical twinning under an applied tensile strain, at 10 ps and with 10% strain. Blue atoms represent original matrix atoms and green ones show the stacking fault layers.

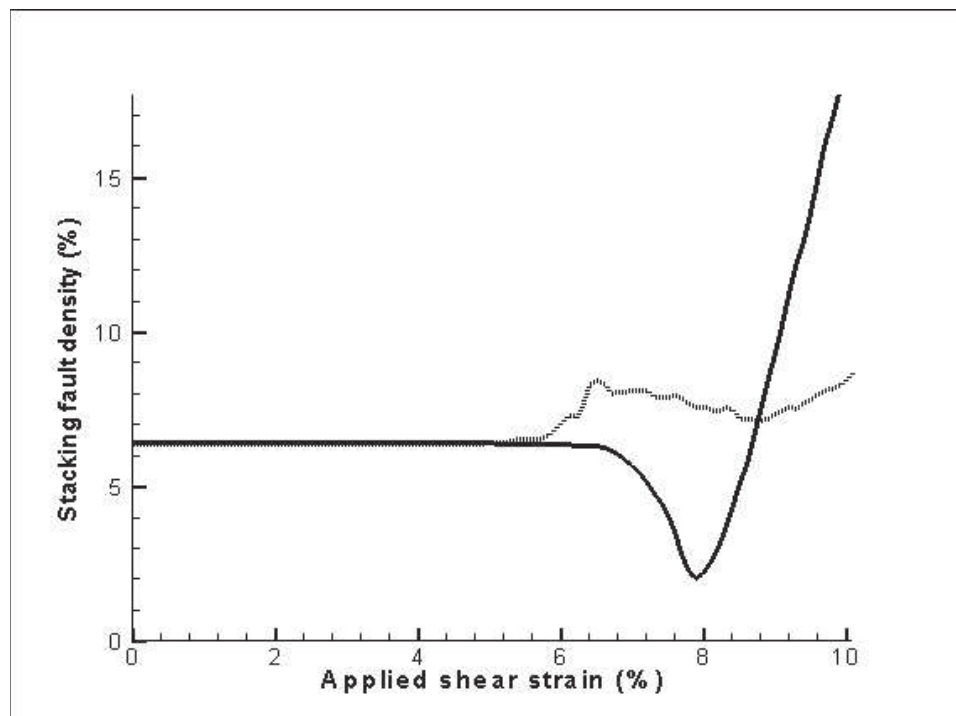


Figure 5.26: Growth of the relative stacking fault areal density for rapid quench of $10^{10} s^{-1}$, solid line, and for slower quench rate of $10^9 s^{-1}$, dotted line.

For comparison, Figure 5.28 shows the time-sequence of single crystal deformation under the same conditions. Green atoms are atoms in a stacking fault. We note that the stacking fault is always nucleated in pairs of adjacent (111) planes, forming the nucleus for the spread of a mechanical twin. Red atoms delineate dislocations leading the spread of the stacking fault.

We can see that in the 3nm nano-twin case, dislocations are well-confined by twin interfaces. While dislocations in the single crystal case can easily glide on their slip planes, dislocations inside the 3nm nano-twin structure can not continue gliding, once they encounter the twin boundary, and they are essentially trapped within the narrow nano-twin channels. When two confined dislocations are close by within the channel, they cross-slip and the screw segments annihilate one another, as can be seen in Figure 5.27 (h)-(l).

If we take a closer look at the deformed crystal as shown in figure 5.29, we can observe both twin boundary migration and mechanical twinning. For example, the green atoms plane shows the original twin boundary, in some of the planes, we can see in part of the plane, the green atoms are one layer higher than the other green atoms in rest of the plane. Between the two parts, there is a red line. So this is the twin boundary migration leading by the partial dislocation line. Between layers of the original twin planes, we see new stack fault plane (the green atoms) show up as pair, surrounding by dislocations (the red atoms), which is the mechanical twins. So we observed both mechanical twinning and twin boundary migration under this situation.

Figure 5.30 illustrate that under shear strain, the number of dislocations nucleated in the 3nm nano-twinned structure (left) in comparison with those in a single crystal structure. As we can see from the figure, the number of dislocations nucleation sites in the 3 nm nano-twin system is much higher than the

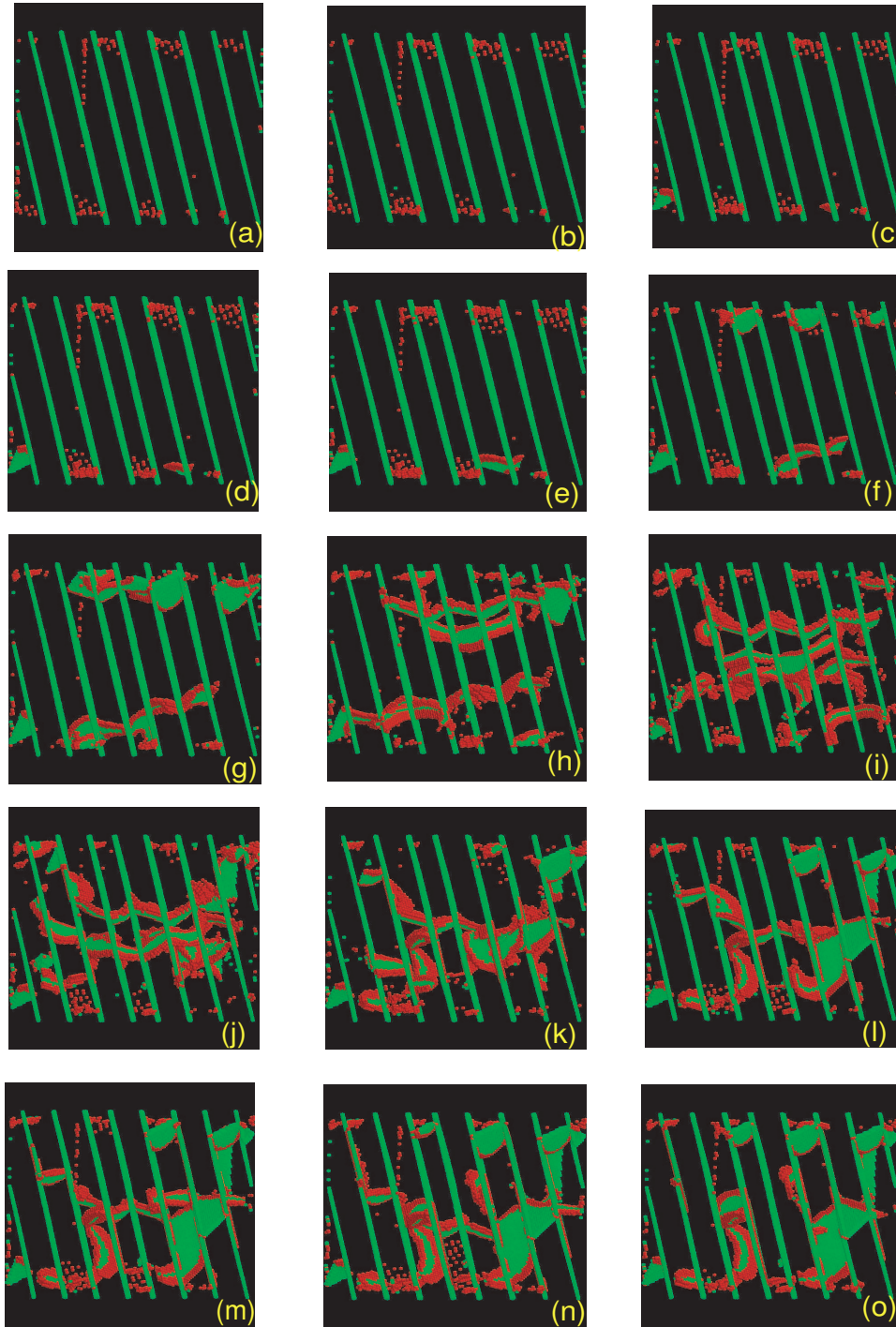


Figure 5.27: A time-sequence of the deformation of a nano-twinned copper structure with a wavelength of 3 nm with applied shear strain at a constant quench rate of $10^9 s^{-1}$. The sequence is as follows: (a) At 54 ps, strain = 5.4%. (b) At 57 ps, strain = 5.7%. (c) At 60 ps, strain = 6.0%. (d) At 63 ps, strain = 6.3%. (e) At 66 ps, strain = 6.6%. (f) At 69 ps, strain = 6.9%. (g) At 72 ps, strain = 7.2%. (h) At 75 ps, strain = 7.5%. (i) At 78 ps, strain = 7.8%. (j) At 81 ps, strain = 8.1%. (k) At 84 ps, strain = 8.4%. (l) At 87 ps, strain = 8.7%. (m) At 90 ps, strain = 9.0%. (n) At 93 ps, strain = 9.3%. (o) At 96 ps, strain = 9.6%.

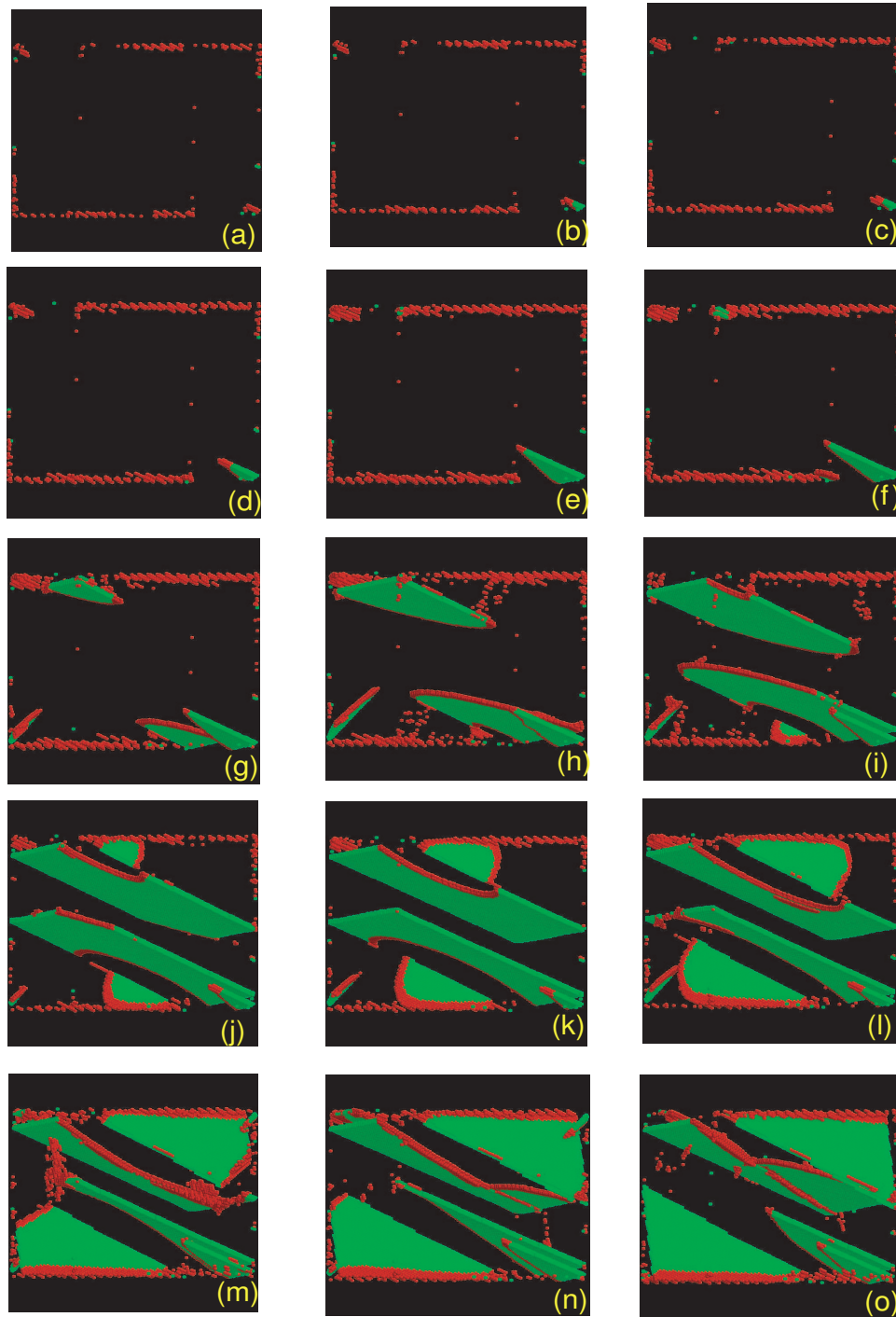


Figure 5.28: A time-sequence of the deformation of a single copper crystal with applied shear strain at a constant quench rate of $10^9 s^{-1}$. The sequence is as follows: (a) At 58 ps, strain = 5.8%. (b) At 61 ps, strain = 6.1%. (c) At 64 ps, strain = 6.4%. (d) At 67 ps, strain = 6.7%. (e) At 70 ps, strain = 7.0%. (f) At 73 ps, strain = 7.3%. (g) At 76 ps, strain = 7.6%. (h) At 79 ps, strain = 7.9%. (i) At 82 ps, strain = 8.2%. (j) At 85 ps, strain = 8.5%. (k) At 88 ps, strain = 8.8%. (l) At 91 ps, strain = 9.1%. (m) At 94 ps, strain = 9.4%. (n) At 97 ps, strain = 9.7%. (o) At 100 ps, strain = 10%.



Figure 5.29: Dominant deformation modes of nano-twinning copper crystals. The figure shows the operation of the Twin Boundary Migration (TBM) mechanism (see fourth boundary from the bottom), and Mechanical Twinning (MT) as is clear in the double layers bound by Shockley partial dislocations.

corresponding number in the single crystal system. Another observation is that in the nano-twinned structure, we see many full dislocations (stacking faults surrounded by a leading and a trailing Shockley partial dislocation). In the single crystal case, however, we observe very few full dislocations.

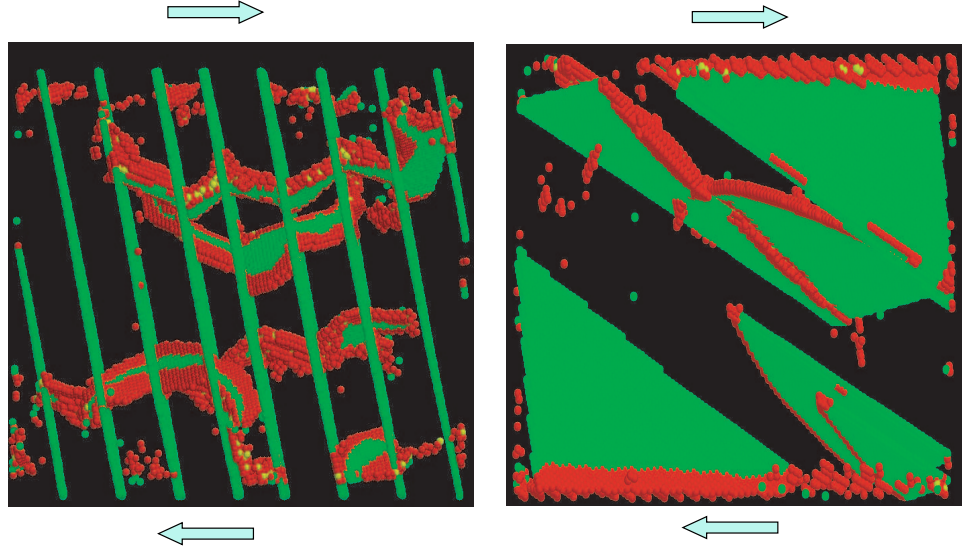


Figure 5.30: A comparison between the deformed structures of the nano-twinned copper (left) and single copper crystal (right) at a strain of 10%. Note the abundance of dissociated dislocations in the nano-twinned case and the abundance of stacking faults in the single crystal.

We also compare the relative Stacking Fault Areal Density (SFAD), defined as the ratio of number of atoms in stacking fault area (excluding the grown-in twins), to the total number of atoms in the crystal, at different nano-twin wavelengths at an applied shear strain of up to 10% (see Figure 5.31). The graph also shows the results for a single copper crystal for reference. As we can see from the figure, the stacking fault density of the single crystal reaches close to 3.5% in about 90 ps, while the density of stacking faults in the nano-twinned structure remains relatively low (typically less than 1%).

The following is a summary of the observations on the deformation of nano-

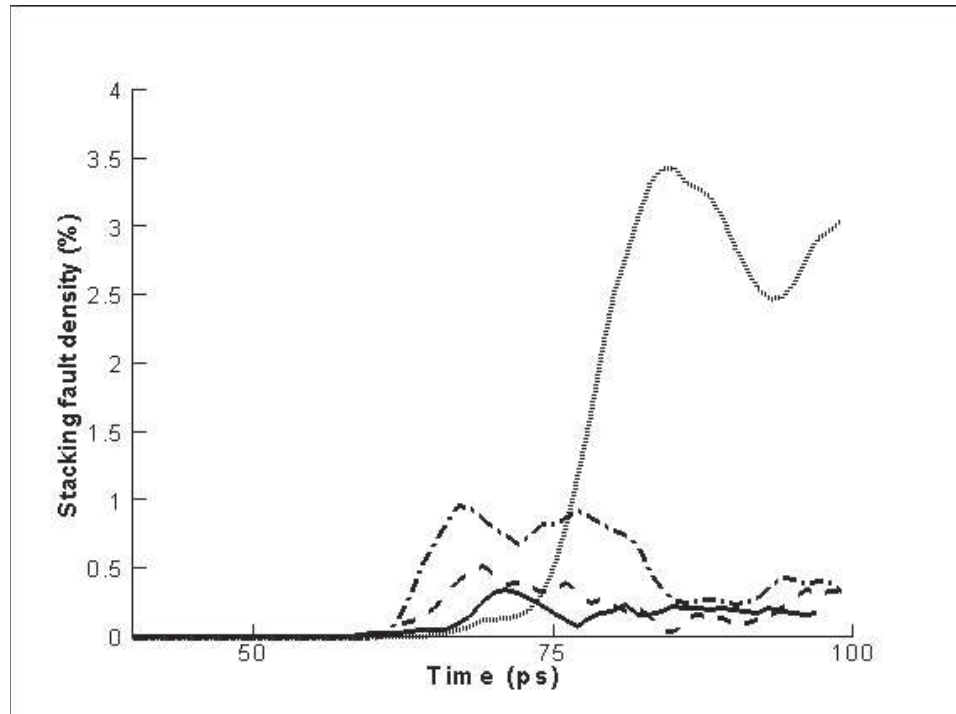


Figure 5.31: Time evolution of the relative Stacking Fault Areal Density (SFAD) for various twin layer size, and for single crystal Cu. Simulations are performed at a constant strain rate of $10^9 s^{-1}$ up to a final strain of 10%. (a) Solid line: nano-twinned crystals with lamella thicknesses of 3 nm, (b) dash line: nano-twinned crystals with lamella thicknesses of 4 nm, (c) dash dot line: nano-twinned crystals with lamella thicknesses of 5 nm, (d) dot line: single crystal.

twinned copper structures under a continuing applied shear strain.

(1) The number of dislocations in the nano-twined structure is much larger than that in a single crystal.

(2) The stacking fault density in the nano-twined structure is lower than that in single crystal.

(3) The trailing dislocation density in a nano-twinned structure is much higher than in a single crystal as a result of dislocation confinement in narrow channels.

We therefore conclude that the rate of dislocation nucleation is higher in a nano-twinned crystal as compared to the single crystal under the same conditions. On the other hand, the rate of expansion of Shockley partials is much higher in a single crystal as compared to a nano-twinned crystal, resulting in a higher rate of deformation twinning in the single crystal case.

The nucleation rate difference is confirmed by the large number of dislocations in nano-twin and the observation that full dislocations are dominant in nano-twins. The reason for the high nucleation rate in a nano-twinned structure is explained to be a result of the large density of nucleation sites in nano-twinned structures, provided by twin boundaries themselves. Additionally, the confinement of dislocations and their motion in narrow channels concentrates the elastic near twin boundaries, which can be released by further nucleation of dislocations.

Although the single crystal has fewer dislocations, a much higher stacking fault areal density is formed. Once dislocations nucleate, they start to spread at very high speeds (approximately 1.3 nm/ ps (or 1300 m/s, comparable to sound speed in Copper: 3570 m/s at 273 K).

The reason behind differences observed in dislocation speeds and glide rates can be explained as a result of the twin boundary confinement.

These two rates both contribute to the total accumulated plastic deformation. Therefore an optimal structure can be found such that the two rates result in the lowest deformation (or the hardest material). In the next section we will discuss the optimization of the nano-twinned structure for maximum strength.

5.4.4 Results for Constant Stress

In the following, we present results of MD computer simulations for the deformation of single and nano-twinned crystalline copper under the conditions of constant stress. Constant values of a tensile stress are applied (2 GPa, 2.5 GPa, and 3 GPa) at 300 K and the equations of motion of all atoms are integrated with a time step of 5 fs. In these simulations, we investigate the dominant deformation modes under constant stress for nano-twinned crystals with lamella thicknesses of 3,4, and 5 nm, respectively.

5.4.4.1 Mechanism Discovered From the Dislocation Visualizations

Figures 5.33, 5.34, 5.35 and 5.36 show time-sequences of the evolution of defect structures and plastic deformation under a constant tensile stress of 2.5 GPa at 300 K for nano-twinned crystals with lamella thicknesses of 3,4, and 5 nm, respectively. A schematic diagram showing the simulation box and direction of tensile stress is shown in Figure 5.32.

When the nano-twin lamella thickness is 3 nm at 2.5 GPa, we observe the following:

Fully dissociated dislocations (with leading and trailing partials) can easily cross the twin boundary and overcome the boundary resistance. A more detailed illustration of this boundary crossing process at 3 nm is shown in Figure 5.37.

A second mode of dislocation interaction with twin interfaces is that of cross-

slip of the leading partial from its original slip plane to the twin interface itself (which is a (111)-type plane), followed by glide of the leading Shockley partial along the interface. Interestingly, the trailing Shockley partial follows by cross-slipping onto the twin boundary interface, but it glides in the opposite direction, expanding the new stacking fault area bound by the two partials and resulting in TBM, as we discussed earlier. This mechanism is shown by arrows in Figure 5.38. The dislocations dissociate onto the twin boundary and glide along the twin boundary, which leads the twin boundary migration.

Under an applied shear stress of 2.5 GPa, dislocation interaction mechanism with twin interfaces is observed to be quite different when the nano-twin lamella thickness is 4 nm. This interaction mechanism is shown in Figure 5.39, where we present a time sequence for the deformation process, and focus the attention on dislocation-twin boundary interaction. It is observed that under these conditions, once the leading partial is nucleated on one twin interface, it expands quickly to

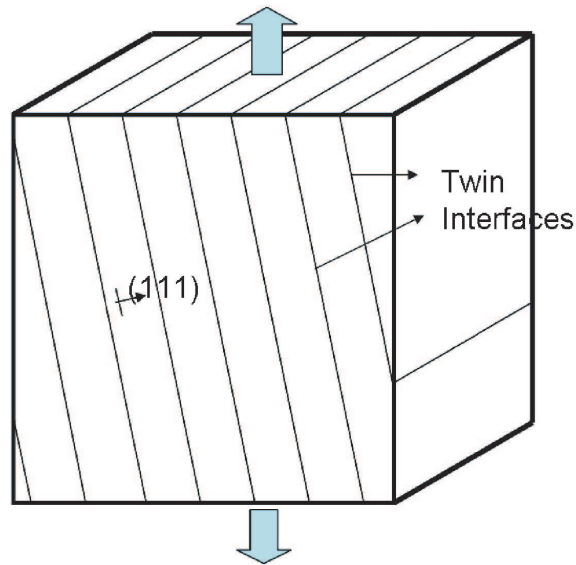


Figure 5.32: A schematic diagram showing the simulation box and direction of tensile stress for nano-twinned crystals.

the other interface, while the trailing partial is almost stationary close to the nucleation site. Collision of the leading partial with the opposite interface results in its trapping, direction reversal, and shrinkage of the dissociated stacking fault zone. The leading partial, once it reverses direction, continues motion till the two partials recombine again at the nucleation site. This interesting behavior is shown in Figure 5.39.

At an applied shear stress of 2.5 GPa and lamella thickness of 5 nm, the previously described dislocation "trapping-recoil" mechanism is also observed. Nevertheless, fully dissociated dislocations are also observed to easily cross twin boundary interfaces, resulting in significant plastic strain. In the single crystal, which is a limiting case here, there is no barrier to dislocation motion. Many stacking faults are generated, which is a prelude to mechanical twinning as a deformation mode. Because of these differences in the deformation behavior of twinned structures of various size lamellae, it appears that there is an optimum lamella thickness for maximizing the strength of the nano-structure. This optimum thickness is on the order of 4 nm for copper. At this thickness, the Shockley partial dislocation emitted from one interface recoils from the opposite interface. Atomic displacements of the two partials represent a trapped wave inbetween the two twin interfaces. The stacking fault inbetween the two Shockley partials induces attraction between the two partials and shrinkage of the fault area. Thus, this "trapping-recoil" mechanism at 4 nm is the main reason for optimal strength in nano-twinned copper. The mechanism will be quantified next by studying the evolution of strain within the simulated systems.

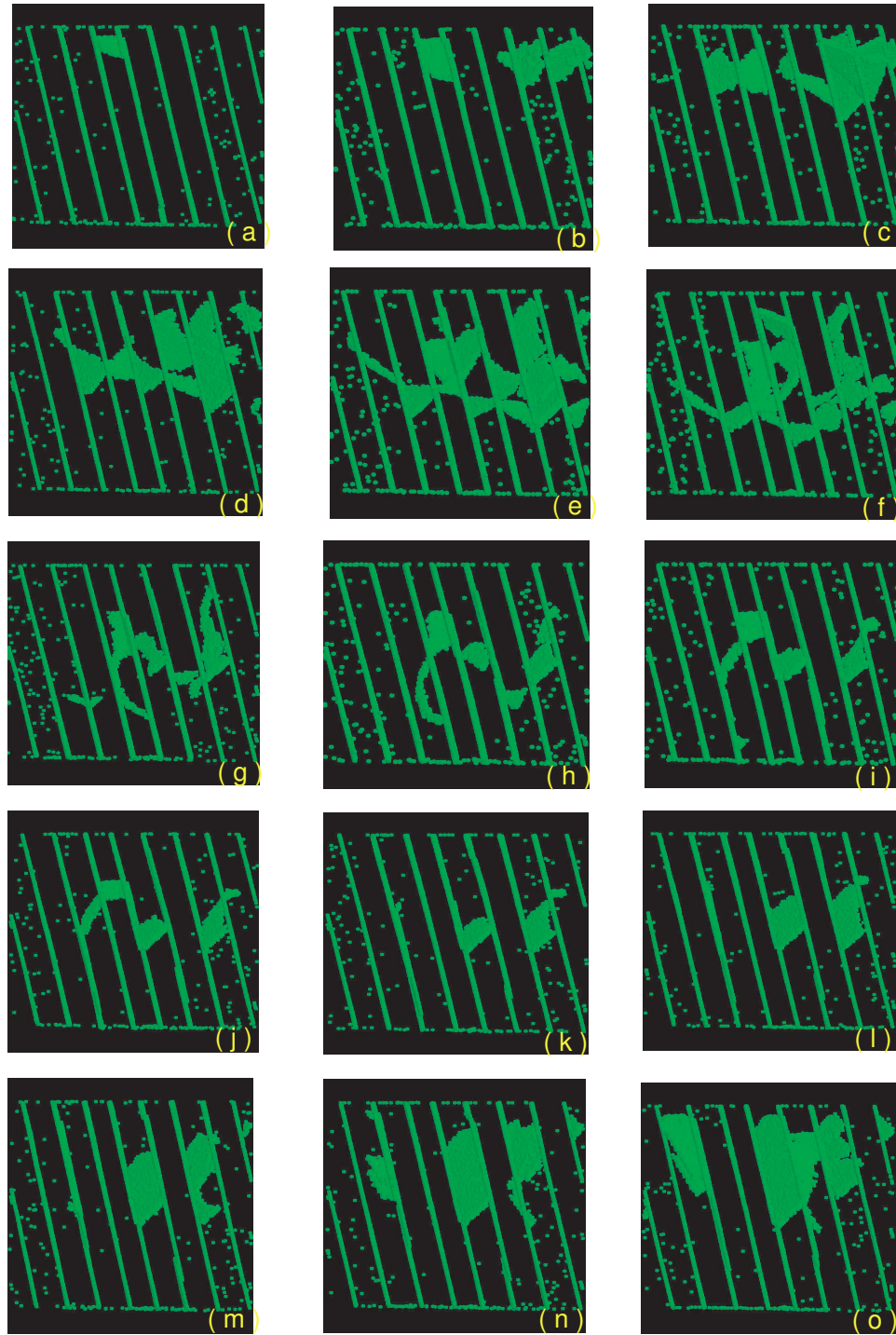


Figure 5.33: Time sequence for the deformation behavior of nano-twinning copper under a tensile stress of 2.5 GPa at 300 K, and with lamella thickness of 3 nm (10 layers are shown here). Simulations are conducted at 300 K, with a time step of 5 fs. The time sequence is as follows: (a) 32 ps, (b) 34 ps, (c) 36 ps, (d) 38 ps, (e) 40 ps, (f) 42 ps, (g) 44 ps, (h) 46 ps, (i) 48 ps, (j) 50 ps, (k) 52 ps, (l) 54 ps, (m) 56 ps, (n) 58 ps, (o) 60 ps.

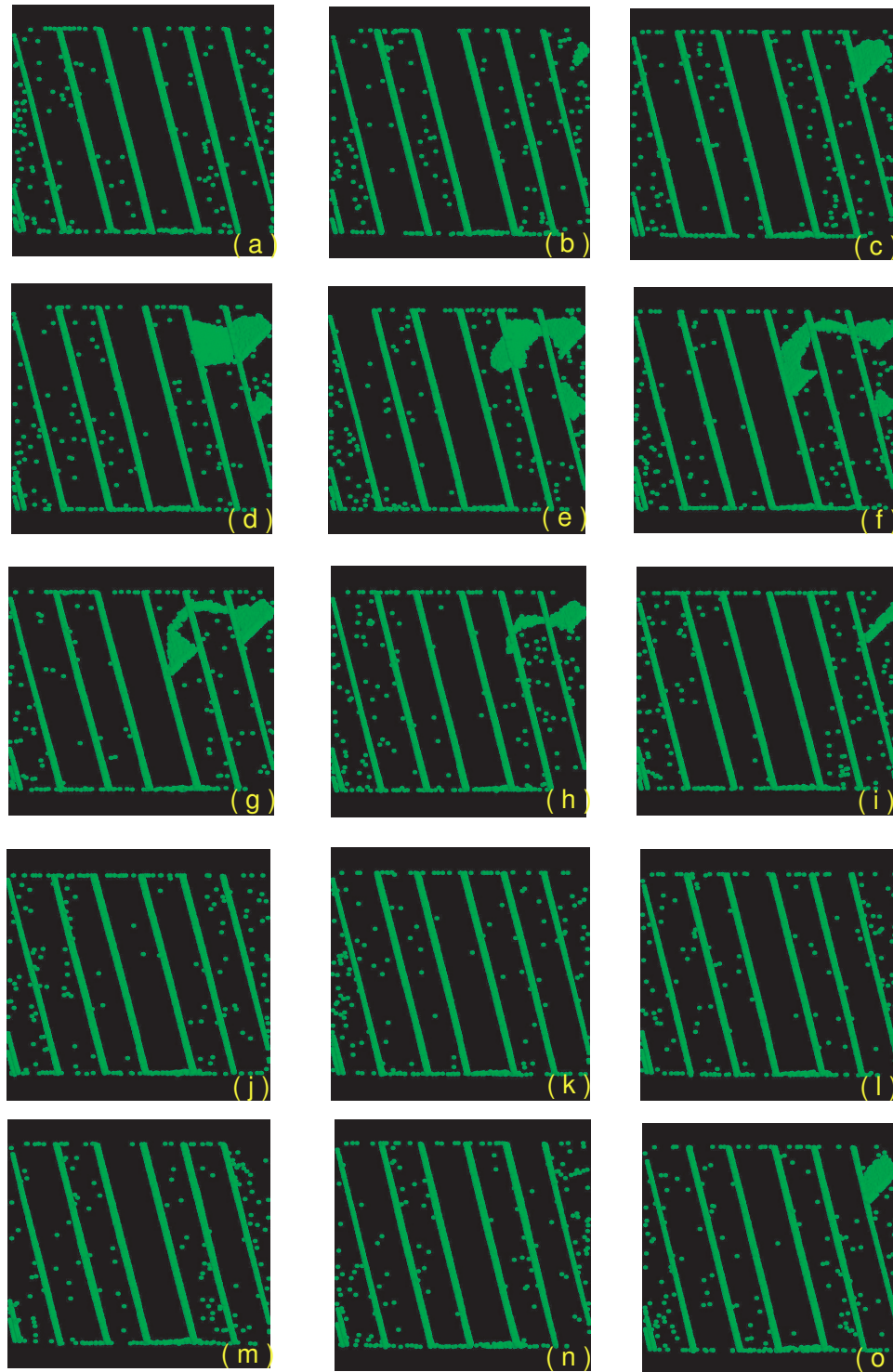


Figure 5.34: Time sequence for the deformation behavior of nano-twinned copper under a tensile stress of 2.5 GPa at 300 K, and with lamella thickness of 4 nm (7 layers are shown here). Simulations are conducted at 300 K, with a time step of 5 fs. The time sequence is as follows: (a) 32 ps, (b) 34 ps, (c) 36 ps, (d) 38 ps, (e) 40 ps, (f) 42 ps, (g) 44 ps, (h) 46 ps, (i) 48 ps, (j) 50 ps, (k) 52 ps, (l) 54 ps, (m) 56 ps, (n) 58 ps, (o) 60 ps.

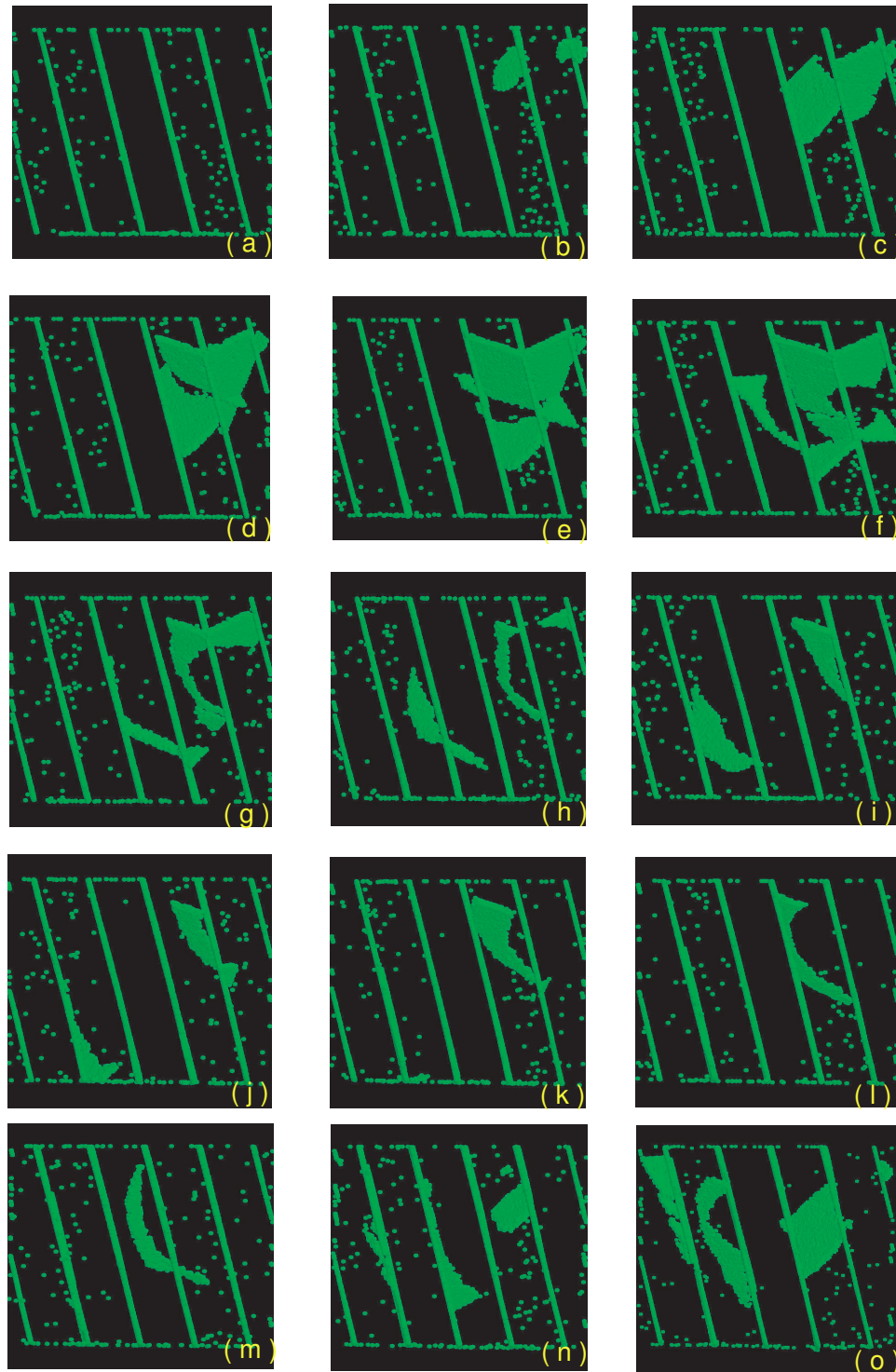


Figure 5.35: Time sequence for the deformation behavior of nano-twinning copper under a tensile stress of 2.5 GPa at 300 K, and with lamella thickness of 5 nm (5 layers are shown here). Simulations are conducted at 300 K, with a time step of 5 fs. The time sequence is as follows: ((a) 32 ps, (b) 34 ps, (c) 36 ps, (d) 38 ps, (e) 40 ps, (f) 42 ps, (g) 44 ps, (h) 46 ps, (i) 48 ps, (j) 50 ps, (k) 52 ps, (l) 54 ps, (m) 56 ps, (n) 58 ps, (o) 60 ps.

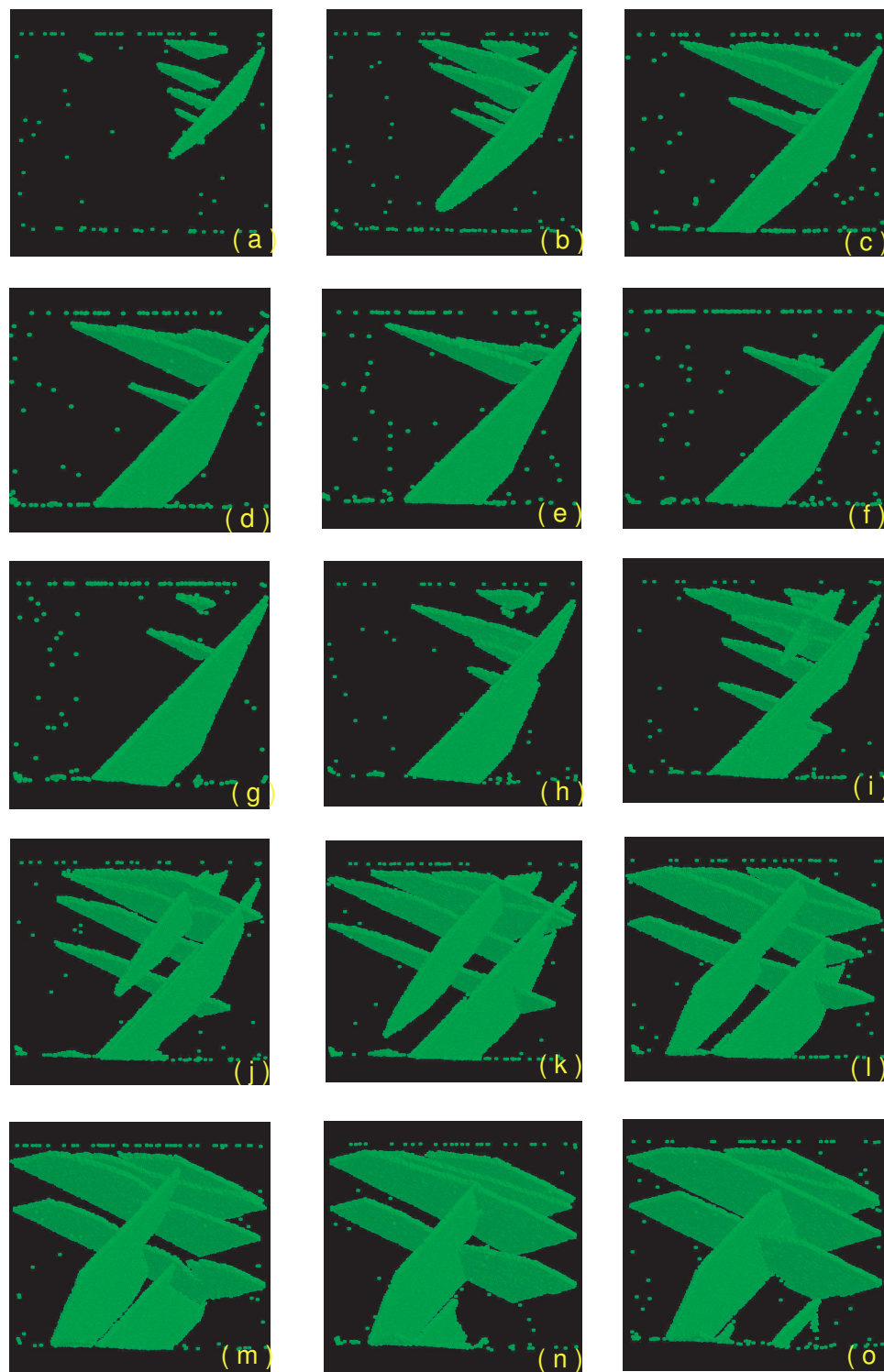


Figure 5.36: Time sequence for the deformation behavior of single crystal copper under a tensile stress of 2.5 GPa at 300 K, and with lamella thickness of 3 nm (10 layers are shown here). Simulations are conducted at 300 K, with a time step of 5 fs. The time sequence is as follows: (a) 32 ps, (b) 34 ps, (c) 36 ps, (d) 38 ps, (e) 40 ps, (f) 42 ps, (g) 44 ps, (h) 46 ps, (i) 48 ps, (j) 50 ps, (k) 52 ps, (l) 54 ps, (m) 56 ps, (n) 58 ps, (o) 60 ps.

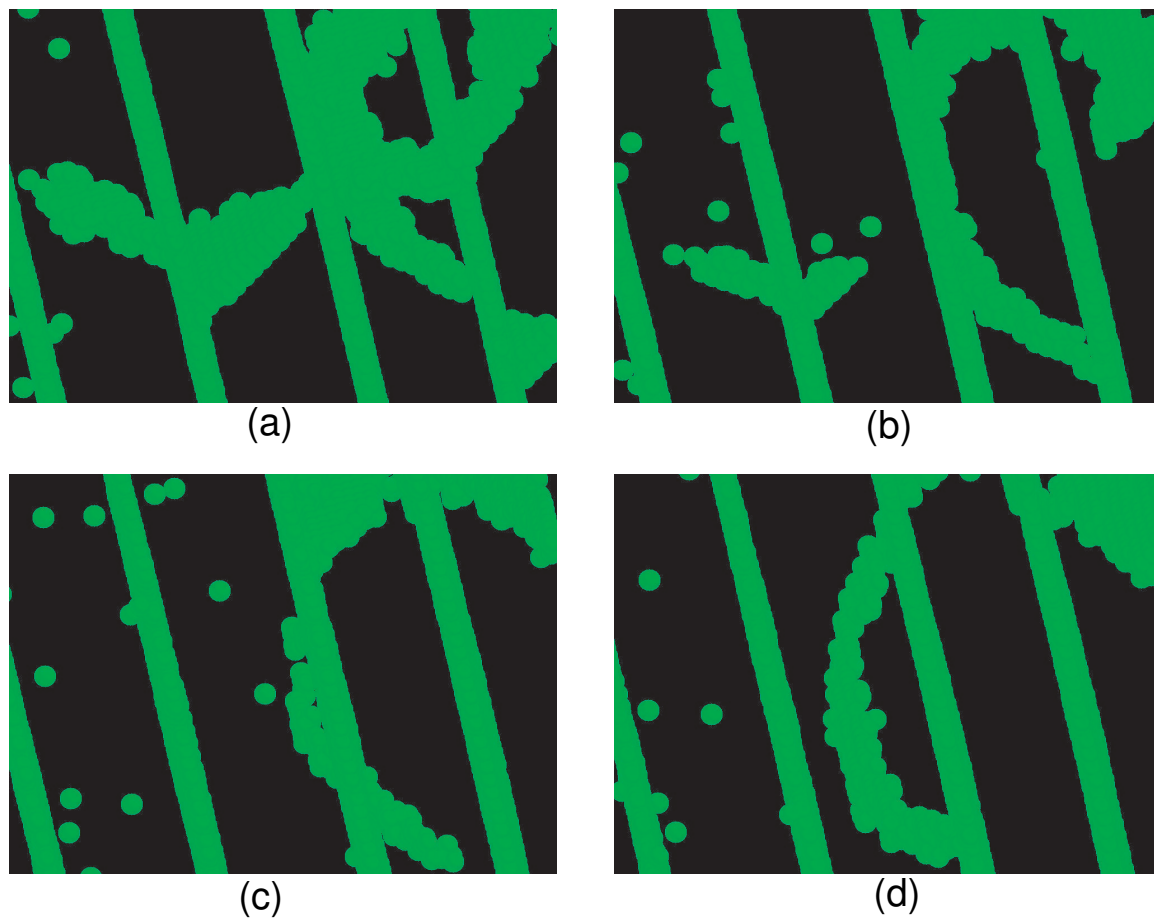


Figure 5.37: Time sequence illustrating the cross-glide mechanism of dislocation loops in nano-twinned copper under a tensile stress of 2.5 GPa at 300 K, and with lamella thickness of 3 nm. The time sequence is as follows: (a) 43 ps, (b) 44 ps, (c) 45 ps, (d) 46 ps. Figure shows that the leading partial crosses twin boundary interfaces.

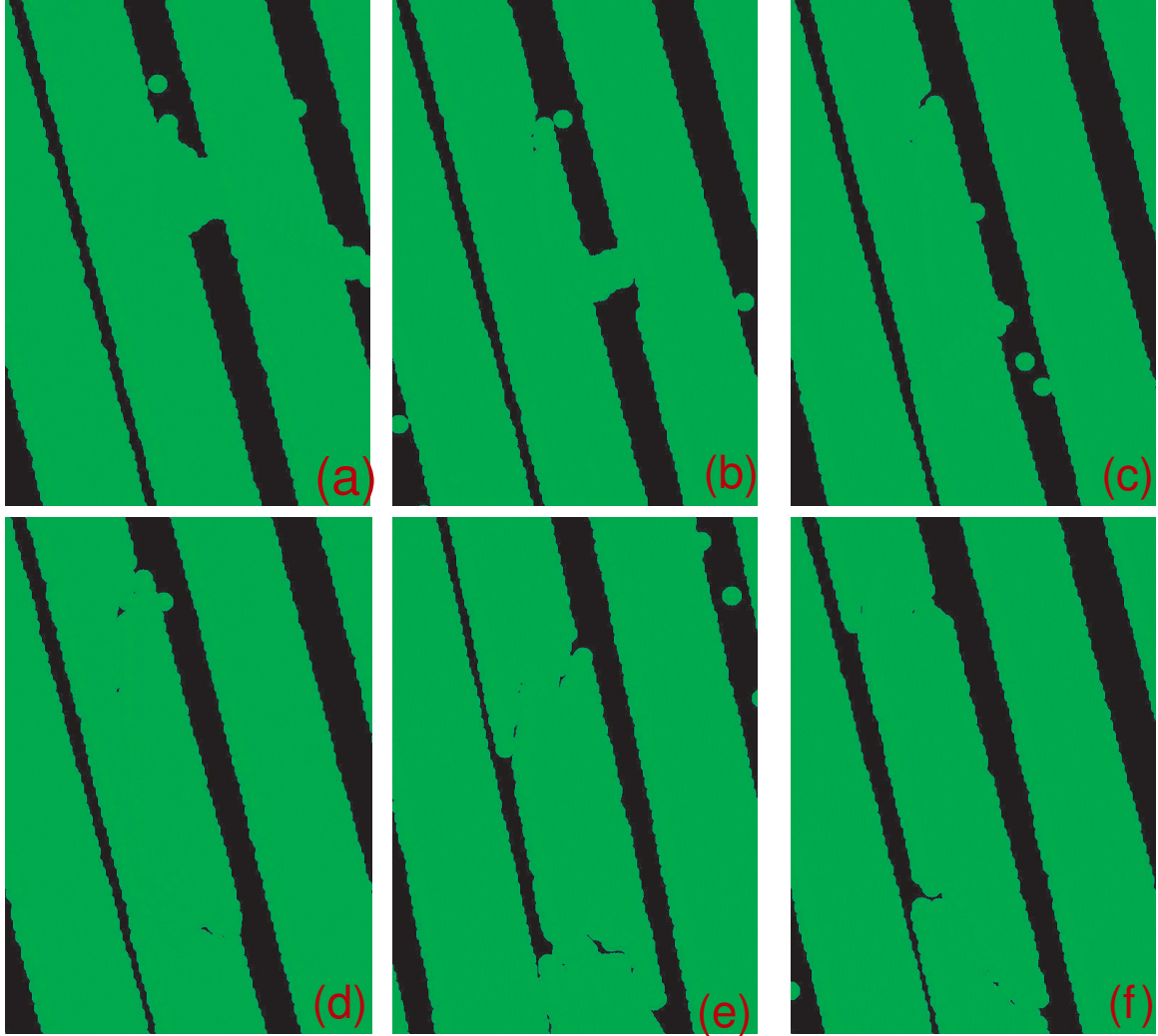


Figure 5.38: Time sequence illustrating the Twin Boundary Migration (TBM) mechanism in nano-twinned copper under a tensile stress of 2.5 GPa at 300 K, and with lamella thickness of 3 nm. The time sequence is as follows: (a) 17 ps, (b) 19 ps, (c) 21 ps, (d) 23 ps, (e) 25 ps, (f) 27 ps. Figure shows that the leading partial glides on the twin interface leading to its migration.

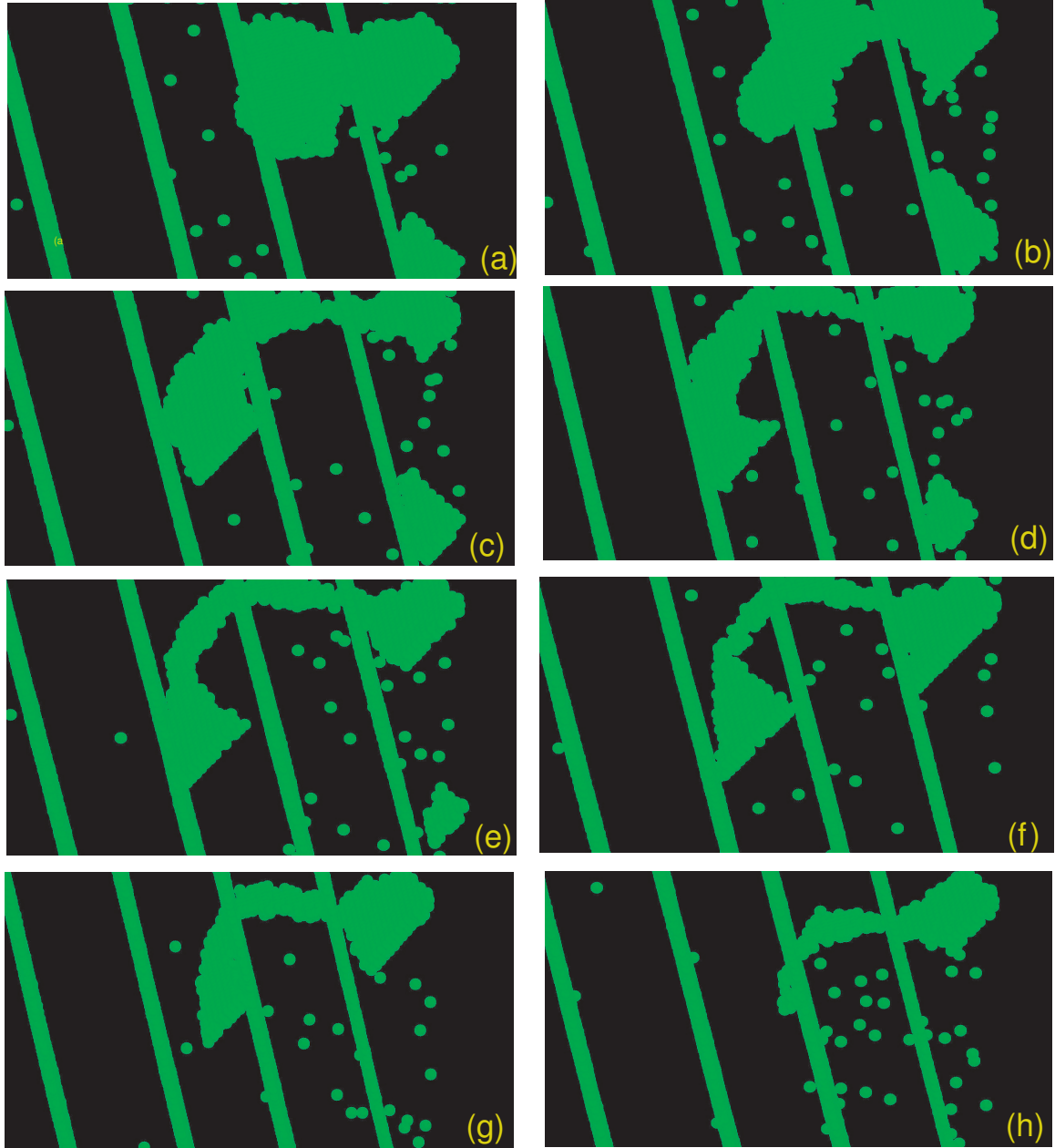


Figure 5.39: Time sequence illustrating the "trapping-recoil" mechanism of dislocations in nano-twinned copper under a tensile stress of 2.5 GPa at 300 K, and with lamella thickness of 4 nm. The time sequence is as follows: (a) 39 ps, (b) 40 ps, (c) 41 ps, (d) 42 ps, (e) 43 ps, (f) 44 ps, (g) 45 ps, (h) 46 ps. Figure shows that the leading partial generates from one boundary, crosses to the opposite boundary, recoils, and finally shrinks back to a small loop close to the nucleation site.

5.4.4.2 Quantitative Analysis of Nano-twinned Structure Deformation

In this section, we will quantify the observations derived from the previous MD simulations on the influence of twin lamella size on the deformation of twinned copper structures. Figures 5.40, 5.41 and 5.42 show the time evolution of the accumulated total strain of twinned copper structures of various lamella thicknesses at applied shear stress levels of 2 GPa, 2.5 GPa, and 3 GPa, respectively. The Resolved Shear Stress (RSS) on the grown-in twin planes are 0.45 GPa, 0.675 GPa, and 0.9 GPa, respectively, while the Resolved Shear Stress (RSS) on the dislocation glide planes intersecting with grown-in twins are 1.28 GPa, 1.92 GPa, and 2.56 GPa, respectively. For comparison purposes, the results of MD simulations at 300 K are shown in Figure 5.40, along with results using the quench relaxation method at 0 K. The oscillations in MD simulations are due to the dynamic extension and contraction of stacking faults and dislocation loops, as they interact with twin boundary interfaces or external surfaces. The quench results show the time evolution behavior under 0 K condition. The results for 0 K deformation are the lower envelope bounding the strain values under dynamic conditions. The time evolution of total strain, displayed in Figures 5.40, 5.41 and 5.42, clearly demonstrate that the lowest deformation is obtained when the lamella size is 4 nm.

5.4.4.3 Dependence of the Relative Stacking fault Areal Density on Lamella Size

Plastic strain can also be measured in terms of the increase in the stacking fault surface area. In Figures 5.43, 5.44 and 5.45, we show the time evolution of the accumulated stacking fault areal density for different twin lamella sizes for applied shear stress of 2 GPa, 2.5 GPa, and 3 GPa, respectively. The stacking

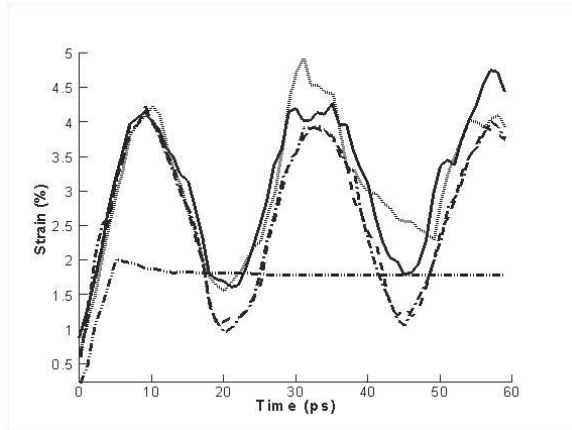


Figure 5.40: Time evolution of the total shear strain for various size nano-twin lamella thickness at an applied shear stress of 2 GPa. (a) Solid line: nano-twin crystals with lamella thicknesses of 3 nm at 300 K, (b) dash line: nano-twin crystals with lamella thicknesses of 4 nm at 300 K, (c) dash dot line: nano-twin crystals with lamella thicknesses of 5 nm at 300 K, (d) dot line: single Cu crystal at 300 K, (e) dash dot dot line: nano-twin crystals with lamella thicknesses of 3 nm at 0 K.

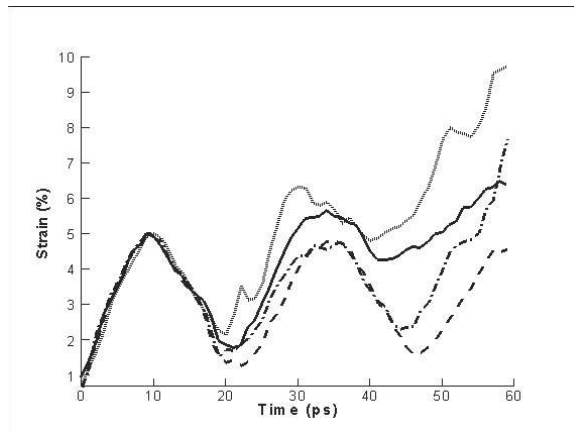


Figure 5.41: Time evolution of the total shear strain for various size nano-twin lamella thickness at an applied shear stress of 2.5 GPa at 300 K. (a) Solid line: nano-twin crystals with lamella thicknesses of 3 nm, (b) dash line: nano-twin crystals with lamella thicknesses of 4 nm, (c) dash dot line: nano-twin crystals with lamella thicknesses of 5 nm, (d) dot line: single Cu crystal.

fault areal density when the nano-twin lamella size is 4 nm and 5 nm is relatively low, confirming the conclusion that an optimal lamella size of about 4 nm gives the most resistance to deformation.

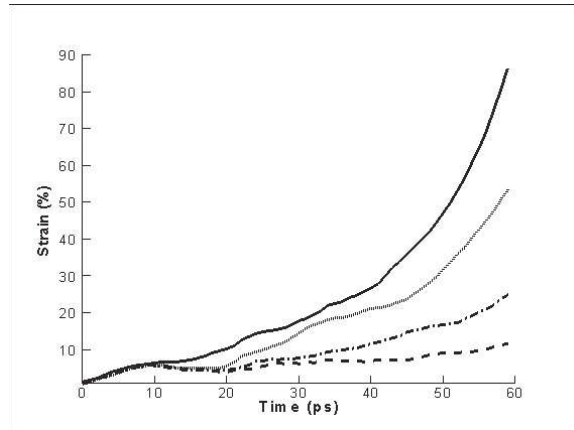


Figure 5.42: Time evolution of the total shear strain for various size nano-twin lamella thickness at an applied shear stress of 3 GPa at 300 K. (a) Solid line: nano-twinning crystals with lamella thicknesses of 3 nm, (b) dash line: nano-twinning crystals with lamella thicknesses of 4 nm, (c) dash dot line: nano-twinning crystals with lamella thicknesses of 5 nm, (d) dot line: single Cu crystal.

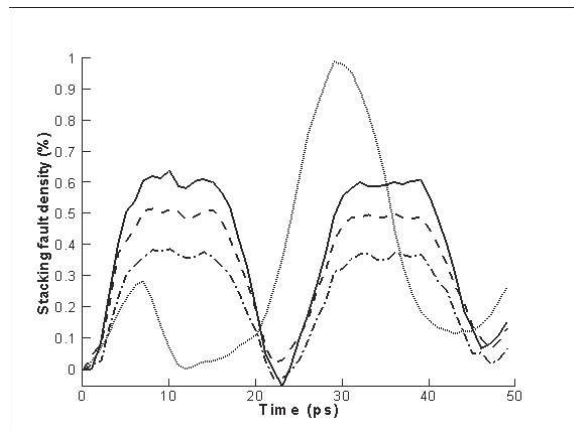


Figure 5.43: Time evolution of the relative stacking fault area for various size nano-twin lamella thickness at an applied shear stress of 2 GPa at 300 K. (a) Solid line: nano-twinning crystals with lamella thicknesses of 3 nm, (b) dash line: nano-twinning crystals with lamella thicknesses of 4 nm, (c) dash dot line: nano-twinning crystals with lamella thicknesses of 5 nm, (d) dot line: single Cu crystal.

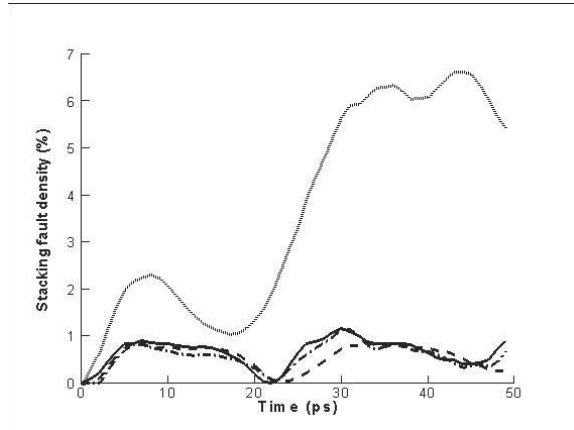


Figure 5.44: Time evolution of the relative stacking fault area for various size nano-twin lamella thickness at an applied shear stress of 2.5 GPa at 300 K. (a) Solid line: nano-twinned crystals with lamella thicknesses of 3 nm, (b) dash line: nano-twinned crystals with lamella thicknesses of 4 nm, (c) dash dot line: nano-twinned crystals with lamella thicknesses of 5 nm, (d) dot line: single Cu crystal.

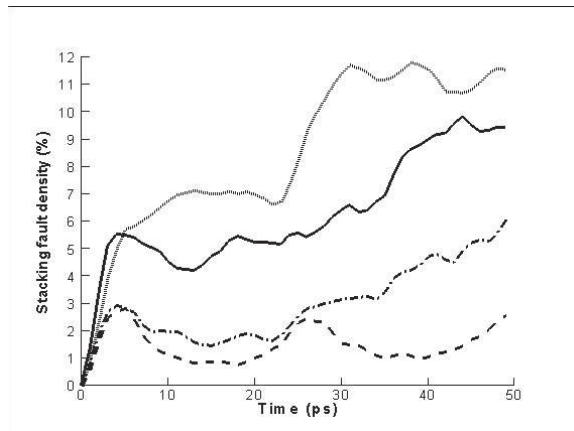


Figure 5.45: Time evolution of the relative stacking fault area for various size nano-twin lamella thickness at an applied shear stress of 3 GPa at 300 K. (a) Solid line: nano-twinned crystals with lamella thicknesses of 3 nm, (b) dash line: nano-twinned crystals with lamella thicknesses of 4 nm, (c) dash dot line: nano-twinned crystals with lamella thicknesses of 5 nm, (d) dot line: single Cu crystal.

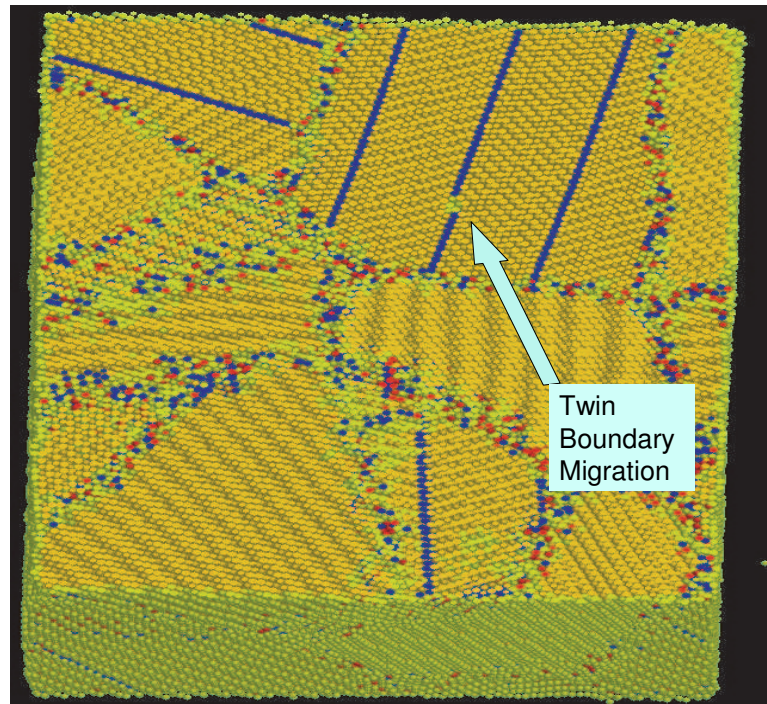
5.4.5 Summary of Nano-twin Lamella Size Effects

The large strength of nano-twinned copper structures is derived from the resistance of twin boundaries to dislocation motion. Although twin boundaries act as nucleation sites for dissociated dislocation loops in twinned copper, they also act as barriers to their subsequent motion. At stress levels below a critical value, dislocations are generally confined in their motion to very narrow channels formed in between twin boundaries. This mode of restricted motion gives rise to strengthening of the structure. When the stress is raised above this critical value, dislocations are able to overcome the twin boundary barrier, and hence confinement is lost. It is found that at an optimal thickness of about 4 nm, Shockley partial dislocations emitted from the surface of one twin boundary recoil from the opposing boundary and are trapped in between. The dynamic effects of the recoil leads to further shrinkage of the stacking fault between the leading and trailing partials, and thus accumulated plastic deformation is recovered in this event.

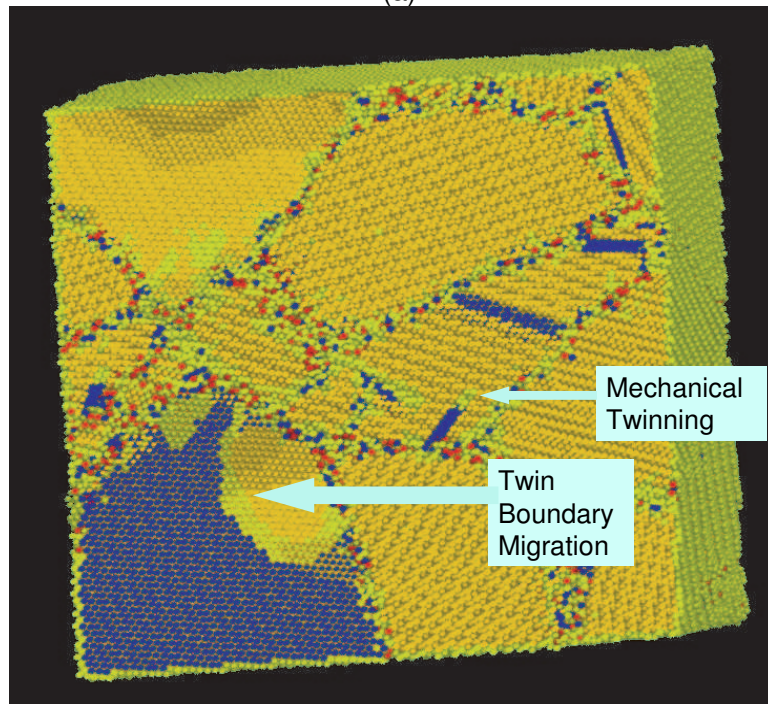
The magnitude of plastic deformation is determined by both dislocation nucleation rate and dislocation propagation rate, and an optimal lamella thickness can thus be obtained to minimize the combined rates of nucleation and propagation. The results of both tension and shear show that when the Schmid stress is computed in each case, Twin Boundary Migration (TBM) will be the dominant deformation mode when the twin boundaries have high Schmid factors, while mechanical twinning and dislocation glide are dominant when other (111)-planes have high Schmid factors.

5.5 Nano-grain Cu with Nano-Twin Structure

The previous results show the strong effects of the basic nano-laminate size on the deformation mechanisms, and also clearly demonstrate the different deformation modes in each case. To examine the effects of grain boundaries on the deformation process, we simulate here the deformation of nano-grains that contain nano-twinned structures. In Figures 5.46 and 5.47 , we show simulation results for 10 nano grains inside a box with size of $20 \text{ nm} \times 20 \text{ nm} \times 20 \text{ nm}$, with 3 grains having grown-in nano-twins of 3nm lamella thickness. Total number of atoms in the box is 677,120. A shear strain of 7% is applied on the box boundary and the system is relaxed with the quench relaxation method at 0 K for 3000 steps with step size of $1 \times 10^{-15} \text{ s}$. These simulations show several different deformation mechanisms: twin boundary migration initiated by Shockley partial dislocations, double layer stacking fault formation as a prelude to mechanical twinning, and full dislocation motion on two adjacent layers. Future efforts should focus on the development of large scale computational simulations with grain size of 300-500 nm, and a twin lamella size of 10-20 nm for comparison with recent experiments [48].



(a)



(b)

Figure 5.46: Deformation of nano grain Cu crystals containing an initial nano-twin structure: Twin Boundary Migration and Mechanical Twinning. A shear strain of 7% is applied at 0 K. System is relaxed for 3000 steps with step size of $1 \times 10^{-15} s$. (a) An intersection view perpendicular to the grown-in twin interfaces, (b) an intersection view parallel to the grown-in twin interfaces.

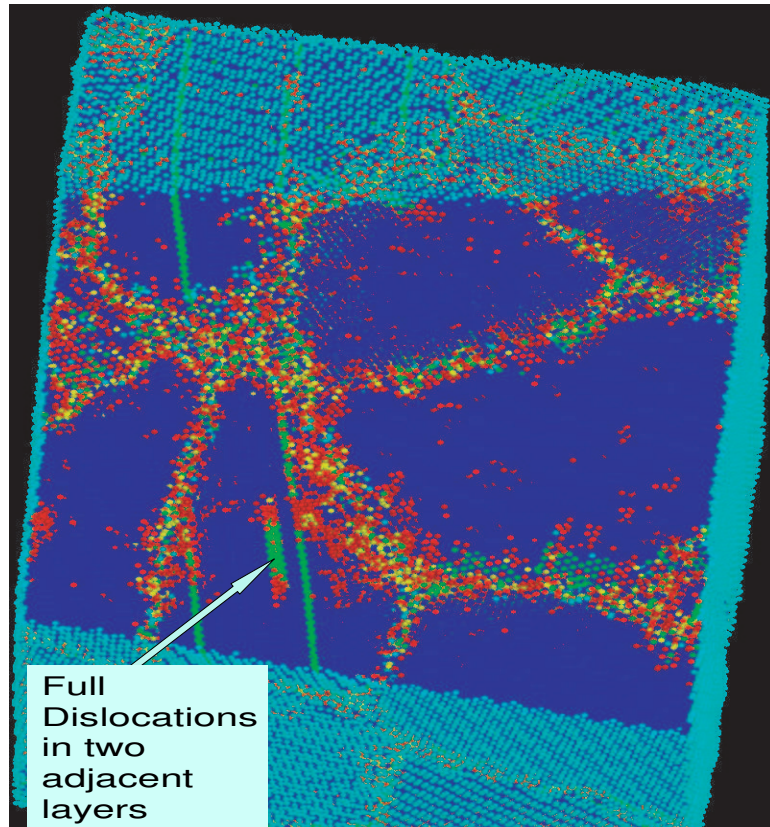


Figure 5.47: Deformation of nano grain Cu crystals containing an initial nano-twin structure: full dislocations in two adjacent layers. A shear strain of 7% is applied at 0 K. System is relaxed for 3000 steps with step size of $1 \times 10^{-15} s$.

CHAPTER 6

Conclusions

6.1 Summary of Discussions

The goal of this thesis was to model nano-layer structures using Molecular Dynamics simulation tools in the hope of finding a suitable nano-layered structure that have ultra-strength. We have largely achieved the main objectives of this thesis, and in the process, we have uncovered several important deformation mechanisms that are responsible for the strength of nanolayered materials. In the following, we summarize the main findings and achievements of this thesis. In our studies of the dislocation motion in Cu/Ni nano-layers using Molecular Dynamics (MD) simulations, we used a simulation box with 3 nano layers (5 nm Ni, 5 nm Cu, and 5 nm Cu). An edge dislocation was inserted into the Cu layer, and then shear strain was applied along the boundary. These simulations revealed that interfaces act as barriers for dislocation transmission, which accelerate or decelerate the motion of Shockley partials of dissociated dislocations. Dislocation transmission across interfaces was found to proceed first by the leading partial and then by the trailing partial, once significant interaction between them is realized. Thus, we found that spread dislocation cores have to be squeezed first before the the dislocation is allowed to be transmitted across the interface. The main mechanism for the resistance here was found to be the modulus mismatch between Cu and Ni (i.e the so called Koehler barrier). Dislocation velocity across nano-laminated systems of the Cu/Ni type was shown to be intermittent, and thus we concluded that dislocation motion is "jerky" in nano-laminates.

Next, our MD simulations of a simple twinned copper structure was aimed at the discovery of the main mechanism by which twin boundaries move under stress in fcc crystals. In a 3 layer twinned-structure simulation box, shear stain was applied parallel to the twin interface. We observed that twin boundary migration is induced by Shockley partial dislocations in the following sequence: (1) nucleation of a partial is initiated by the coordinated thermal motion of atoms in a coherent wave. The first partial nucleation site was observed to occur under three 3 conditions: (a) on the layer directly adjacent to the twin boundary, (b) at the surface of the crystal, (c) and at stress concentration regions. (2) partial dislocation glide under the applied shear strain leads the upward twin boundary migration by one atomic layer. (3) when two partials with the same Burgers vectors merge together in the middle of the slip plane, the local stress is so large that a new dislocation loop nucleates on top of the merge point, and on the plane adjacent to the newly-formed twin boundary. The continuous operation of this mechanism results in twin boundary migration under stress over long distances relative to interatomic spacings.

We also studied the effects of nano-twin lamella size on the deformation of nano-twinned copper. The deformation behavior of nano-twinned Cu with different twin thickness was simulated under several loading conditions. Simulations were performed for both constant applied shear strain and constant applied tensile stress. The relative stacking fault areal density and the number of nucleated dislocations are compared for different lamella thickness of twin structures. Our simulations clearly demonstrated that the number of dislocations in a nano-twin structured material is much more than the number of dislocations in a single

crystal, while the SDF in nano-twin structure is much less than the SDF in the corresponding single crystal. In nano-twins, dissociated full dislocations dominate while in a single crystal we observed very few full dislocations. Those observations lead to the conclusion that the degree of plastic deformation is determined by both dislocation nucleation rate and dislocation propagation rate, implying that an optimal thickness exists. MD simulation results confirmed the main mechanism of strengthening in nano-twinned copper as the restriction of dislocation motion in narrow channels (twinned layers). A critical twin thickness, maximum strength and minimum plastic deformation are observed. At lamella thickness of 4 nm, the leading partial dislocation emitted from one twin interface propagates to the opposite interface, recoil there, reverses direction, shrinking the core of the emitted dislocation core and confine it to remain in the same twinning channel. At lamella thickness of 3 nm, MD simulations indicate that dislocations can easily cross twin interfaces. It is also found from our simulations that the stress state greatly influence the main deformation mechanism. In the case of a large Schmid stress compared to normal components on the twin interface, the main mechanism of deformation is observed to be the TBM mechanism. When the Schmid stress on the twin interface is small compared to its value on intersecting (111)-slip planes, the main deformation mode is observed to be double layer nucleation and growth of Shockley partial dislocations.

My research on the deformation mechanisms of nano-laminate and nano-twinned materials have resulted in a number of new contributions. A computational method to distinguish twin interfaces from other defects we developed. The phenomenon of jerky motion of dislocations moving in nano-laminates was revealed by MD simulations of dislocation motion in nano-laminates of Cu/Ni structures. Critical conditions for dislocation confinement and transmission were uncovered. A new MD model for nano twinned Cu in single and polycrys-

talline configurations was established. The Twin Boundary Migration Mechanism (TBM) was identified as a deformation mode in nano-twinned Cu when the Schmid stress is high on the twin interface, and the dislocation nucleation and propagation in narrow twin channels as the main deformation mechanism when the Schmid stress is low on the twin interface and high on intersecting (111)-glide planes. Finally, the factors that determine the strength of nano-twinned Cu have been discovered, enabling a materials-by-design approach to optimize the strength and ductility of nano-structured materials.

APPENDIX A

Molecular Dynamics Code Summary

Several free public MD codes are currently available on the internet. Although these codes share the same basic equations, they have some differences in dealing with details such as neighbor searches, force calculations, interatomic potential type, input method, parameter control, boundary control and user interface, etc.

As mentioned before, the codes are developed for each group's need and the writer's personal preference, and there is no one that was developed perfectly for our computational cluster and specific needs. I will outline below the specific features of the MD codes we used, and then specify what needs to be done to write a suitable code for nano deformation problems in the future.

A.1 XMD

Before we have our own MD code, the best code we can use now is the one called XMD, which is written by Jon Rifkin from the University of Connecticut [73]. This is a parallel code written in C and has a flexible user interface. It can do most of the work we are interested in doing and has the function that can read in different styles of EAM potentials.

However, XMD is written for parallel machines with Shared Memory, as stated in their Readme documents, "Only SMP computers are likely to support POSIX threads, these are "shared memory" systems that typically have up to 8 or 16 cpus." Since our ISIS cluster is a Message Passing type cluster with non-shared memory in each node, we can not run the parallel XMD version on it. However,

we still can run it a single process and do most of our simulations.

XMD and related documents can be downloaded from

<http://xmd.sourceforge.net/>

The input file is written with command lines and saved as *.xm file. One can then use the command:

```
../src/xmd *.xm
```

to run the simulation.

A.2 LAMMPS

Some MD codes can run in a message passing cluster architecture: for example the PARADYN and LAMMPS developed by Steve Plimpton at Sandia National Lab; ALCMD by Morris and Turner at Ames Labs. Among them, LAMMPS has a very new version which is written in C++ and is quite powerful and flexible. This can be found on the web site:

<http://www.cs.sandia.gov/~sjplimp/LAMMPS>

One problem of LAMMPS is that it only reads in the first generation of EAM potentials. Although other EAM potential formats look similar, LAMMPS still needs different modules to handle different types of potentials.

A.3 Other MD codes

There are other parallel MD codes I have not used, such as CHARMM, AMBER, NAMD, NWCHEM, and TINKER, and these are designed primarily for modeling biological molecules. The reader may find the information under this link:

<http://www.cs.sandia.gov/~sjplimp/LAMMPS/>

A.4 MakeFiles

For parallel codes, to compile them in our cluster, there is always system compatibility problems. Usually, those codes give different versions of Makefiles that are used for different Linux operating systems. Unfortunately, our system is usually not in any of their list. So it usually requires us to write a similar new Makefile to help the compiler find the MPI in order to compile parallel codes.

A.5 SIDE CODE

Those MD codes calculate the main function of MD: the equations of motion. They usually take an input atomic coordinates file (a start cell) and calculate the future coordinates of those atoms based on the potentials and boundary conditions. First, we need to generate the computational cell of interest, for example a box with some interface inside with certain orientations and with certain kinds of defects, such as dislocations. They usually have several type of output information that can be used to do further analysis. The most often used information is the coordinate output file. The coordinate output file includes the information of all the coordinates of all atoms in the simulation cell. There will be millions of atoms and we are mainly interested in defects. It is hard to abstract information from millions of pure numbers, so that we developed our own software to process output files for needed atomic information.

A.5.1 Code to build the input model

A.5.1.1 Generation of Perfect Crystals with Specific Orientations

I developed software to generate a perfect crystal lattice. The method is to repeat the unit cell in all 3 directions. Because dislocations glide on 111-planes, we use the [111] direction as one of the Cartesian axes. For the same reason, [110] is

another interesting direction because it is the Burgers vector direction in an FCC crystal. There are two methods to generalize such a cell with these directions as axis. One is to generate a cell with axes as $[100]$, $[010]$ and $[001]$ directions then rotate it. The other method is to take the base cell with $[111]$ axes and then repeat it. We use the last method because it gets rid of the rotation matrix and results in smooth boundaries. The tradeoff is that the second method is not as flexible as the first one for cell generation in other orientations. The method is specific for $[111]$ orientations only, while the first method can rotate the lattice to any orientation. However, since we are only interested in $[111]$ axes, we prefer to use the second method.

A.5.1.2 Generation of Twin and Grain Interfaces

The code can also generate twin interfaces by stacking (111) planes by different sequences at two sides of a twin interface. For example, on one side of the twin interface, the sequence is ABCABC while on the other side the sequence is ACBACB. The code can generate a Cu/Ni grain interface assuming that the interface is a (111)-plane and along the dislocation moving direction $[110]$.

A.5.1.3 Dislocation Generation

The code can add half plane of (110) atoms into the cell to form an edge dislocation. To do this, first the atoms are displaced according to the displacement field of an anisotropic dislocation, then the extra plane atoms are added. Doing this can avoid the problem that some atoms are too close to one another and cause the potential energy to be excessively high. This code can not add other types of dislocations, and to do that, we will use another code discussed below, courtesy of Dr. Satish Rao.

A.5.2 Code to analyze the output model

A.5.2.1 Centro-symmetry method to identify defect atoms

There are several methods to identify defects, such as energy and geometry methods (e.g. the Centro-symmetry and coordination number identification schemes). We adopt the geometry method, because it is derived from the exact definition of a dislocation in the lattice and has less associated computational noise. We use Centro-symmetry method by finding the nearest neighbors of each atom, pair those neighbors to find the best 6 pairs, and add the vector sum of the distance between the object atom and each neighbor in these 6 best pairs. If the object atom is in a perfect site, the vector sum of its 6 pair neighbors should be close to 0. On the other hand, atoms around the dislocation core will be in some highly distortion position in a lattice and has asymmetry neighbors so that the vector sum will be large. Therefore, we are able to identify atoms in defect configurations by the amplitude of this vector sum. In our code, we assign a different type to the defect atoms based on the sum value. For example, we assign 'Au' to the atoms with the largest vector sums, and assign 'H' to atoms with the smallest vector sums. We use this to be able to clearly visualize atoms by different colors in the visualization software discussed below.

A.5.2.2 Masking Perfect Atoms

I developed another code to mask atoms in perfect sites in order to utilize the visualization software for the analysis of defect motion. Otherwise the huge number of atoms always make the computer extremely slow and also prevent us from observing the interesting aspects of atomic scale deformation..

A.5.3 Software to Visualize Atoms

A.5.3.1 Accelrys DS views

This is a commercial software with good picture quality and an easy mouse-operation interface. The only problem is that when we try to export a movie into other formats such as the avi format, it is not quite easy to do so.

A.5.3.2 Pymol

This is a free software that can be downloaded from <http://pymol.sourceforge.net/>. It is small, simple but as powerful as DS views. However, it uses command operations and thus requires more training for best utilization. So need more time to get use to it. This software also has an option to save a movie into separate JPG figures then use some other movie maker software to produce an avi format movie using those figures.

A.5.4 Adding Dislocations by the Anisotropic Displacement Field (Courtesy of Dr. Satish Rao, AFRL)

(This elastic displacement code was developed by Dr. Man Yoo at ORNL 15 years ago. As an example, its input file reads:

```
NiAl s.rao potential Elastic Const 1 1 1.0000000
4.05192 10.72 10.72 10.72
3.22 3.22 3.22 6.51 6.51 6.51
1 1-1 2 1 1 0 1 1 0 2
```

To generate the displacement field for a set of atoms, based on their initial positions and the position at which the dislocation has to be put in, we input the

six roots of the sextic equation (real and imaginary parts of three roots), then the displacement constants (9 real parts first, 9 imaginary parts next), then the dislocation line direction, glide plane, magnitude of the Burgers vector. It should work with any kind of dislocation.

The elastic solutions with "displacement components" ($A_1(M,N)$ and $B_1(M,N)$, $M = 21,22,23$) are the displacement constants. A_1 is the real part and B_1 is the imaginary part.

REFERENCES

- [1] F. F. Abraham, J. Q. Broughton, N. Bernstein, and E. Kaxiras. Spanning the length scales in dynamic simulation. *Comput. Phys.*, 12:538–546, 1987.
- [2] R.J. Amodeo and N. M. Ghoniem. A review of experimental observations and theoretical models of dislocation cells. *Res Mech.*, 23:137, 1988.
- [3] Peter Michael Derlet Anders Gudmund Froseth and Helena Van Swygenhoven. Twinning in nanocrystalline fcc metals. *Advanced Engineering Materials*, 7(1-2):16, 2005.
- [4] P. M. Derlet A. Froseth, H. Van Swygenhoven. The influence of twins on the mechanical properties of nc-al. *Acta. Materialia*, 52:2259, 2005.
- [5] P. M. Derlet A. G. Froseth and H. Van Swygenhoven. Grown-in twin boundaries affecting deformation mechanisms in nc-metals. *Appl. Phys. Lett.*, 85(24):5863, 2004.
- [6] S.P. Baker. The analysis of depth-sensing indentation data. In P.J. Blau and B.R. Lawn, editors, *Mater. Res. Soc. Symp. Proc.*, volume 308, page 209, Philadelphia, PA, 1993. Materials Research Society.
- [7] D.M. Barnett and J. Lothe. Line force loadings on anisotropic half-spaces and wedges. *Physica Norvegica*, 8:13–22, 1975.
- [8] M. I. Baskes. Application of the embedded-atom method to covalent materials - a semiempirical potential for silicon. *Phys. Rev. Lett.*, 59:2666–2669, 1987.
- [9] Van Swygenhoven H. Derlet P. M. Van Petegem S. Budrovic, Z. and B. Schmitt. Plastic deformation with reversible peak broadening in nanocrystalline nickel. *Science*, (273-276), 2004.
- [10] V. V. Bulatov, S. Yip, and A. S. Argon. Atomic modes of dislocation mobility in silicon. *Philos. Mag. A*, 72:453–496, 1995.
- [11] W. Cai, M. de Koning, V. V. Bulatov, and S. Yip. Minimizing boundary reflections in coupled-domain simulations. *Phys. Rev. Lett.*, 85:3213–3216, 2000.
- [12] G.H. Campbell, S.M. Foiles, H. Huang, D.A. Hughes, W.E. King, D.H. Lassila, D.J. Nikkel, T. Diaz de la Rubia, J. Y. Shu, and V. P. Smyshlyaev. Multi-scale modeling of polycrystal plasticity: A workshop report. *Mat. Sci. Eng.*, A251:1, 1998.

- [13] J. P. Chang, W. Cai, V. V. Bulatov, and S. Yip. Dislocation motion in bcc metals by molecular dynamics. *Mater. Sci. Eng. A*, 309:160–163, 2001.
- [14] N. X. Chen. Modified Mobius inverse formula and its applications in physics. *Phys. Rev. Lett.*, 64:1193–1195, 1990.
- [15] F. Cleri, D. Wolf, S. Yip, and S. R. Phillpot. Atomistic simulation of dislocation nucleation and motion from a crack tip. *Acta Mater.*, 45:4993–5003, 1997.
- [16] R. E. Cohen, M.J. Mehl, and D. A. Papaconstantopoulos. Tight-binding total-energy method for transition and noble metals. *Phys. Rev. B*, 50:14694, 1994.
- [17] M. Daw and M. Baskes. Semiempirical, quantum mechanical calculation of hydrogen embrittlement in metals. *Phys. Rev. Lett.*, 50:1285, 1983.
- [18] M. S. Duesbery and V. Vitek. Plastic anisotropy in b.c.c. transition metals. *Acta Mater.*, 46:1481, 1998.
- [19] T. Dumitrica, T. Belytscko, and B. I. Yakobson. Bond-breaking bifurcation states in carbon nanotube fracture. *J. Chem. Phys.*, 118:9485–9488, 2003.
- [20] U. Erb, G. Palumbo, R. Zugic, and K.T. Aust. Structure-property relationships of nano-crystalline materials. In *Treatise on Materials Science and Engineering*, page 93, Pittsburgh, PA., 1996. The Minerals, Metals and Materials Research Society.
- [21] F. Ercolessi and J. Adams. Interatomic potentials from 1st-principles calculations - the force-matching method. *Europhys. Lett.*, 26:583–588, 1994.
- [22] F. Ercolessi, E. Tosatti, and M. Parrinello. Au(100) surface reconstruction. *Phys. Rev. Lett.*, 57:719–722, 1986.
- [23] Liao X. C. et al. Deformation twinning in nanocrystalline copper at room temperature and low strains rate. *Appl. Phys. Lett.*, 84:592–594, 2004.
- [24] M. Finnis and J. Sinclair. A simple empirical n-body potential for transition metals. *Phil. Mag. A*, 50:45, 1984.
- [25] Th. Frauenheim, D. Porezag, M. Elstner, G. Jungnickel, J. Elsner, M. Haugk, and A. Sieck. An ab initio two-center tight-binding approach to simulations of complex materials properties. In A. Gonis P. E.A. Turchi and L. Colombo, editors, *Tight-Binding Approach to Computational Materials Science*, volume 491, page 91. MRS Symposium Proc., 1998.

- [26] C.W. Gear. *Numerical Initial Value Problems in Ordinary Differential Equations*. Prentice-Hall, Englewood Cliffs, 1971.
- [27] S. I. Golubov, X. L. Liu, H. C. Huang, and C. H. Woo. GFCUBHEX: Program to calculate elastic green's functions and displacement fields for applications in atomistic simulations of defects in cubic and hcp crystals. *Comput. Phys. Commun.*, 137:312–324, 2001.
- [28] P. Gumbsch and H. Gao. Dislocations faster than the speed of sound. *Science*, 283:965–968, 1999.
- [29] V. Vitek G. J. Ackland. Many-body potentials and atomic-scale relaxation in noble-metal alloys. *Physical Review B*, 41(15):10324, 1990.
- [30] J. C. Hamilton, R. Stumpf, K. Bromann, M. Giovannini, K. Kern, and H. Brune. Dislocation structures of submonolayer films near the commensurate-incommensurate phase transition: Ag on pt(111). *Phys. Rev. Lett.*, 82:4488–4491, 1999.
- [31] J. C. Hamilton. Dislocation nucleation rates during submonolayer growth of heteroepitaxial thin films. *Phys. Rev. B*, 55:R7402–R7405, 1997.
- [32] J.P Hirth and J. Lothe. *Theory of dislocations*. John Wiley & Sons, New York, 1982.
- [33] R. G. Hoagland, J. P. Hirth, and P. C. Gehlen. Atomic simulation of dislocation core structure and peierls stress in alkali-halide. *Philos. Mag. A*, 34:413–439, 1976.
- [34] W. G. Hoover. Canonical dynamics - equilibrium phase-space distributions. *Phys. Rev. A*, 31:1695–1697, 1985.
- [35] H. C. Huang, N. M. Ghoniem, T. Diaz de la Rubia, M. Rhee, H. Zbib, and J. P. Hirth. Stability of dislocation short-range reactions in bcc crystals. *J. Eng. Mater. Tech.*, 121:143–150, 1999.
- [36] H. C. Huang, N. M. Ghoniem, J. K. Wong, and M. I. Baskes. Molecular-dynamics determination of defect energetics in beta-sic using three representative empirical potentials. *Model. Simul. Mater. Sci. & Eng.*, 3:615–627, 1995.
- [37] P. M. Derlet H. Van Swygenhoven and A. G. Froseth. Stacking fault energies and slip in nanocrystalline metals. *Nature Materials*, 3:399, 2004.

- [38] M.R. James and J.B. Cohen. The measurement of residual stresses by x-ray diffraction techniques. In H. Herman, editor, *Treatise on Materials Science and Technology*, volume 19A, page 1, New York, N.Y., 1980. Academic Press.
- [39] J. F. Justo, M. de Koning, W. Cai, and V. V. Bulatov. Point defect interaction with dislocations in silicon. *Mater. Sci. Eng. A*, 309:129–132, 2001.
- [40] T. Kido, T. Maruyama, K. Niita, and S. Chiba. MD simulation study for nuclear matter. *Nucl. Phys. A*, 663:877c–880c, 2000.
- [41] E. Kuramoto, K. Ohsawa, and T. Tsutsumi. Computer simulation of atomic properties and dynamic behavior of interstitial clusters in Ni. *J. Comput. Aided Mater. Design*, 7:89–95, 2000.
- [42] E. Kuramoto K. Ohsawa. Flexible boundary condition for a moving dislocation. *Journal of Applied Physics*, 86(1):179, 1999.
- [43] J. E. Lennard-Jones. On the determination of molecular fields. ii. from the equation of state of a gas. *Proc. Roy. Soc. A*, 106:463–477, 1924.
- [44] W. C. Liu, S. Q. Shi, H. C. Huang, and C. H. Woo. Dislocation nucleation and propagation during thin film deposition under compression. *Comput. Mater. Sci.*, 23:155–165, 2002.
- [45] W. C. Liu, S. Q. Shi, C. H. Woo, and H. C. Huang. Dislocation nucleation and propagation during thin film deposition under tension. *Comput. Model. Eng. Sci.*, 3:213–218, 2002.
- [46] Q. K. Li and S. Q. Shi. Dislocation jumping over the sound barrier in tungsten. *Appl. Phys. Lett.*, 80:3069–3071, 2002.
- [47] J.L. Loubet, J.M. Georges, and G.F. Meille. Micro indentation techniques in materials science and engineering. In P.J. Blau and B.R. Lawn, editors, *ASTM-STP 889*, page 72, Philadelphia, PA, 1986. American Society for Testing and Materials.
- [48] Chen X Qian L Lu K. Lu L, Shen Y. Ultrahigh strength and high electrical conductivity in copper. *Science*, 304:422, 2004.
- [49] Shan ZW Dao M Lu K Suresh S. Lu L, Schwaiger R. Nano-sized twins induce high rate sensitivity of flow stress in pure copper. *Acta mater*, 53:2169, 2005.

- [50] M.J. Mehl and D. A. Papaconstantopoulos. Applications of a tight-binding total-energy method for transition and noble metals: Elastic constants, vacancies, and surfaces of monatomic metals. *Phys. Rev. B*, 54:4519, 1996.
- [51] Papaconstantopoulos D A Voter A F Mishin Y, Mehl M J and Kress J D. Structural stability in lattice defects in copper: Ab initio, tight-binding and embedded-atom calculations. *Phys. Rev. B*, 63:224106, 2001.
- [52] J. A. Moriarty, J. F. Belak, R. E. Rudd, P. Söderlind, F. H. Streitz, and L. H. Yang. Quantum-based atomistic simulation of materials properties in transition metals. *J. Phys.: Condens. Matter*, 14:2825, 2002.
- [53] J. A. Moriarty and M. Widom. First-principles interatomic potentials for transition-metal aluminides: Theory and trends across the 3d series. *Phys. Rev. B*, 56:7905, 1997.
- [54] J. A. Moriarty. Density-functional formulation of the generalized pseudopotential theory: III. transition-metal interatomic potentials. *Phys. Rev. B*, 38:3199–3231, 1988.
- [55] J. A. Moriarty. Angular forces and melting in bcc transition-metals - a case-study of molybdenum. *Phys. Rev. B*, 49:12431–12445, 1994.
- [56] P. M. Morse. Diatomic molecules according to the wave mechanics: II. vibrational levels. *Phys. Rev.*, 34:57–64, 1929.
- [57] H. Mughrabi. Dislocation wall and cell structures and long-range internal-stresses in deformed metal crystals. *Acta Met.*, 31:1367, 1983.
- [58] H. Mughrabi. A 2-parameter description of heterogeneous dislocation distributions in deformed metal crystals. *Mat. Sci. & Eng.*, 85:15, 1987.
- [59] M. I. Baskes Murray S. Daw. Embedded-atom method: Derivation and application to impurities, surfaces, and other defects in metals. *Physical Review B*, 29(12):6443, 1984.
- [60] L. E. Murr. *Interfacial Phenomena in Metals and Alloys*. Reading, MA, 1975.
- [61] K. J. Hemker H. Sheng Y. Wang M. Chen, E. Ma and X. Cheng. Deformation twinning in nanocrystalline aluminum. *Science*, 300(5623):1275, 2003.
- [62] Esteban Busso Nicolas Kioussis Nasr M. Ghoniem, Hanchen Huang. Multiscale modeling of nano- and micro- mechanics: an overview. 2002.

- [63] H. Neuhäuser. *Slip-line formation and collective dislocation motion.*, volume 6. 1983.
- [64] S. Nose. A molecular-dynamics method for simulations in the canonical ensemble. *Mol. Phys.*, 52:255–268, 1984.
- [65] M. Ortiz and R. Phillips. Nanomechanics of defects in solids. *Adv. Appl. Mech.*, 36:1–79, 1999.
- [66] M. Parrinello and A. Rahman. Polymorphic transitions in single-crystals - a new molecular-dynamics method. *J. Appl. Phys.*, 52:7182–7190, 1981.
- [67] R. Pasianot, D. Farkas, and E. J. Savino. Empirical many-body interatomic potential for bcc transition-metals. *Phys. Rev. B*, 43:6952–6961, 1991.
- [68] D. G. Pettifor and I.I. Oleinik. Analytic bond-order potentials beyond Tersoff-Brenner. I. theory. *Phys. Rev. B*, 59:8487, 1999.
- [69] D. G. Pettifor and I.I. Oleinik. Bounded analytic Bond-Order potentials for σ and π bonds. *Phys. Rev. Lett.*, 84:4124, 2000.
- [70] D. G. Pettifor. New many-body potential for the bond order. *Phys. Rev. Lett.*, 63:2480, 1989.
- [71] S. I. Rao and C. Woodward. Atomistic simulations of $(a/2)\langle 111 \rangle$ screw dislocations in bcc mo using a modified generalized pseudopotential theory potential. *Philos. Mag. A*, 81:1317–1327, 2001.
- [72] S. Rao, Simmons J.P. Hernandez, C., T.A. Parthasarathy, and C. Woodward. Green’s function boundary conditions in two-dimensional and three-dimensional atomistic simulations of dislocations. *Phil. Mag. A*, 77:231–256, 1998.
- [73] Jon Rifkin. <http://www.ims.uconn.edu/centers/simul/xmd/doc-2.5.30/xmd.html>.
- [74] D. Rodney and G. Martin. Dislocation pinning by glissile interstitial loops in a nickel crystal: a molecular-dynamics study. *Phys. Rev. B*, 61:8714–8725, 2000.
- [75] D. Rodney and R. Phillips. Structure and strength of dislocation junctions: an atomic level analysis. *Phys. Rev. Lett.*, 82:1704–1707, 1999.
- [76] B. Schonfelder, P. Keblinski, D. Wolf, and S. R. Phillpot. On the relationship between grain-boundary migration and grain-boundary diffusion by molecular-dynamics simulation. *Mater. Sci. Forum*, 294:9–16, 1999.

- [77] B. Schonfelder, D. Wolf, S. R. Phillpot, and M. Furtkamp. Molecular-dynamics method for the simulation of grain-boundary migration. *Interface Sci.*, 5:245–262, 1997.
- [78] A. Segmuller and M. Murakami. X-ray diffraction analysis of strains and stresses in thin films. In H. Herman, editor, *Treatise on Materials Science and Engineering*, volume 27, page 143, New York, N.Y., 1988. Academic Press.
- [79] S. Q. Shi, H. C. Huang, and C. H. Woo. Interaction of a transonic dislocation with subsonic dislocation and point defect clusters. *Comput. Mater. Sci.*, 23:95–104, 2002.
- [80] J. E. Sinclair. Improved atomistic model of a bcc dislocation core. *J. Appl. Phys.*, 42:5321–5329, 1971.
- [81] M.K. Small, B.J. Daniels, B.M. Clemens, and W.D. Nix. The elastic biaxial modulus of Ag-Pd multilayered thin films measured using the bulge test. *J. Mater. Res.*, 9:25, 1994.
- [82] Bruce A. Hendrickson Steve J. Plimpton. Parallel molecular dynamics with the embedded atom method. *Materials Theory and Modelling*, 291:37, 1993.
- [83] F. H. Stillinger and T. A. Weber. Computer simulation of local order in condensed phases of silicon. *Phys. Rev. B*, 31:5262, 1985.
- [84] J. Tersoff. New empirical model for the structural properties of silicon. *Phys. Rev. Lett.*, 56:632, 1986.
- [85] Jr. Troy Barbee. Optical applications of nano-laminates. In *Technology Days in the Government Mirror Development and Related Technologies*. Lawrence Livermore National Laboratory, September 2003.
- [86] H. Van Swygenhoven, A. Caro, and D. Farkas. A molecular dynamics study of polycrystalline fcc metals at the nanoscale: Grain boundary structure and its influence on plastic deformation. *Mater. Sci. Eng. A*, 309:440–444, 2001.
- [87] H. Van Swygenhoven. Polycrystalline materials - grain boundaries and dislocations. *Science*, 296:66–67, 2002.
- [88] V. Vitek. Theory of the core structures of dislocations in body-centred-cubic metals. *Crystal Lattice Defects*, 5:1, 1974.

- [89] L. Kubin B. Devincre S. Yip V. Bulatov, F. F. Abraham. Connecting atomistic and mesoscale simulations of crystal plasticity. *Nature(London)*, 391:669, 1998.
- [90] G. F. Wang, A. Strachan, T. Cagin, and W. A. Goddard. Molecular dynamics simulations of $1/2$ a (111) screw dislocation in ta. *Mater. Sci. Eng. A*, 309:133–137, 2001.
- [91] J. Wang, C. H. Woo, and H. C. Huang. Destabilization of dislocation dipole at high velocity. *Appl. Phys. Lett.*, 79:101–104, 2001.
- [92] C. H. Woo, H. C. Huang, and W. J. Zhu. Low dimension self-interstitial diffusion in a-zr. *Appl. Phys. A*, 76:101–106, 2002.
- [93] C. H. Woo and M. P. Puls. Improved method of calculating lattice friction stress using an atomistic model. *J. Phys. C*, 9:L27–L31, 1976.
- [94] T.W. Wu, C.-K. Lee, and R.H. Wang. Micro-impact technique and its application. In *Mater. Res. Soc. Symp. Proc.*, volume 308, page 133, 1993.
- [95] W. Xu and J. A. Moriarty. Atomistic simulation of ideal shear strength, point defects, and screw dislocations in bcc transition metals: Mo as a prototype. *Phys. Rev. B*, 54:6941–6951, 1996.
- [96] W. Xu and J. A. Moriarty. Accurate atomistic simulations of the peierls barrier and kink-pair formation energy for $\langle 111 \rangle$ screw dislocations in bcc mo. *Comput. Mater. Sci.*, 9:348–356, 1998.
- [97] E. J. Lavernia D. W. He Y. T. Zhu X. C. Liao, F. Zhou. Deformation twins in nanocrystalline al. *Allp. Phys. Lett.*, 83:5062–5064, 2004.
- [98] M. Zaiser. Statistical modeling of dislocation systems. *Mat. Science & Engr. A*, 3019-310:304–315, 2001.
- [99] W. Q. Zhang, Q. Xie, X. J. Ge, and N. X. Chen. Interatomic potentials between distinct atoms from first-principles calculation and lattice-inversion method. *J. Appl. Phys.*, 82:578–582, 1997.
- [100] S. J. Zhou, D. L. Preston, P. S. Lomdahl, and D. M. Beazley. Large-scale molecular dynamics simulations of dislocation intersection in copper. *Science*, 279:1525–1527, 1998.